ABSTRACT

Title of Document: AN EVALUATION OF A SEVERE SMOG EPISODE IN THE EASTERN U.S. USING REGIONAL MODELING AND SATELLITE MEASUREMENTS.

Elena Andreyevna Yegorova, Doctor of Philosophy, 2011

Directed By: Dr. Dale J. Allen, Assistant Research Scientist, Dr. Russell R. Dickerson, Professor, Department of Atmospheric and Oceanic Science

An ensemble of regional chemical modeling (WRF/Chem with RADM2) simulations, satellite, ozonesonde, and surface observations during July 7-11, 2007 was used to examine the horizontal and vertical signature of one of the worst smog events in the eastern U.S. in the past decade. The general features of this event – a broad area of high pressure, weak winds and heavy pollution, terminated by the passage of a cold front – were well simulated by the model. Average 8-hr maximum O_3 has a mean ($\pm\sigma$) bias of 0.59 ($\pm$ 11.0) ppbv and a root mean square error of 11.0 ppbv. WRF/Chem performed the best on poor air quality days, simulating correctly

the spatial pattern of surface O_3. Yet the model underpredicted O_3 maxima by 5-7 ppbv in the Northeast and overpredicted by 8-11 ppbv in the Southeast. High O_3 biases in the Southeast are explained by overpredicted temperatures in the model (>1.5°C). Sensitivity simulations with 1) accelerated O_3 dry deposition velocity and 2) suppressed multiphase nitric acid formation pushed the model closer to observations. Simulated O_3 vertical profiles over Beltsville, MD showed good agreement with ozonesonde measurements, but the modeled boundary layer depth was overpredicted on July 9, contributing to the low bias over this region.

During this severe smog episode, space-borne TES detected high total tropospheric column ozone (TCO) over the Western Atlantic Ocean off the coast near North and South Carolina. The standard product (OMI/MLS) missed the magnitude of these local maxima, but the level-2 ozone profile (OMI) confirmed the TES observations. HYSPLIT back trajectories from these O_3 maxima intersected regions of strong convection over the Southeast and Great Lakes regions. When lightning NO emissions were implemented in WRF/Chem, the high concentrations of NO_x and O_3 off the coast were well reproduced, showing that the exported O_3 was produced by a combination of natural NO and pollutants lofted from the lower atmosphere. Lastly, WINTER MONEX O_3 data from 1978 are presented for the first time here in discussion of open cell convection over Indonesia.

AN EVALUATION OF A SEVERE SMOG EPISODE IN THE EASTERN U.S. USING REGIONAL MODELING AND SATELLITE MEASUREMENTS.

By

Elena Andreyevna Yegorova

Dissertation submitted to the Faculty of the Graduate School of the
University of Maryland, College Park, in partial fulfillment
of the requirements for the degree of
Doctor of Philosophy
2011

Advisory Committee:
Professor Russell R. Dickerson, Co-Chair
Assistant Research Scientist, Dale J. Allen, Co-Chair
Adjunct Professor Kenneth E. Pickering
Professor Ross J. Salawitch
Professor Sheryl H. Ehrman

Dedication

I dedicate this work to my wonderful children and my loving husband who had to compete for my time and attention with this dissertation for many, many years. To my parents, parents-in-law, and our wonderful nanny for all their love, help and encouragement in bringing-up my kids and studying. To my grandparents for their love. In loving memory of grandfather Arkadiy.

Acknowledgements

I want to acknowledge Dale Allen, Russell Dickerson and Kenneth Pickering for their ideas, support and help with this work. I am grateful for all your advice and patience. Special thanks to Chris Loughner, the model guru, for trouble shooting my WRF/Chem issues. For fear of forgetting to name someone, thanks to all that contributed to this dissertation. Individual thanks to Jeff Stehr, Anne Thompson, Dylan Jones, Xiong Liu, Georg Grell, Steven Peckham, Louisa Emmons, Michael Woodman, David Krask, Mark Schoeberl, John Yorks, Greg Osterman, Al Cooper and Matus Martini.

Table of Contents

List of Tables

List of Figures

Chapter 1 Introduction

Pollution from anthropogenic activities is an important issue due to its effects on regional and global air quality and climate. The high-density urban corridor stretching from Washington, D.C. to Boston in the northeast U.S. frequently experiences summertime smog events, which have detrimental health effects on young children, elderly, and people with respiratory problems. In the U.S. approximately 4,000 premature deaths per year occur due to elevated O_3 concentrations during smog events [*Bell et al.*, 2004]. An estimated 1.8-3.1 years of life per person are lost due to exposure to particulate matter in the most polluted U.S. cities [*Pope et al.*, 2000].

The Mid-Atlantic region faces unhealthy levels of ozone several times each summer. The July 7-11, 2007 episode was the worst air quality event recorded in the Mid-Atlantic region in the past decade in which 8 hour maximum ozone mixing ratios in northeastern Maryland reached 125 ppbv (Figure 1.1). Such high O_3 8-hr maxima are the first to occur in Maryland since the NO_x State Implementation Plan (SIP) Call, which became effective in 2003 and mandated substantial power plant NO_x emission reduction in 22 eastern states [*Frost et al.*, 2006]. Occurrence of thunderstorms at the end of this smog event creates the potential for this regional pollution event to be exported from North America and contribute to hemispheric pollution.

In the Mid-Atlantic region poor air quality events generally occur during the months of May-October under favorable meteorological conditions of high-pressure synoptic systems: high temperatures, clear skies, weak winds, and stagnation [*Ryan et al.*, 2000]. Local vehicle emissions of O_3 precursors, NO and NO_2 (NO_x) and volatile

organic compounds (VOCs) and transport of power plant generated NO_x from the Ohio River Valley contribute to O_3 production.

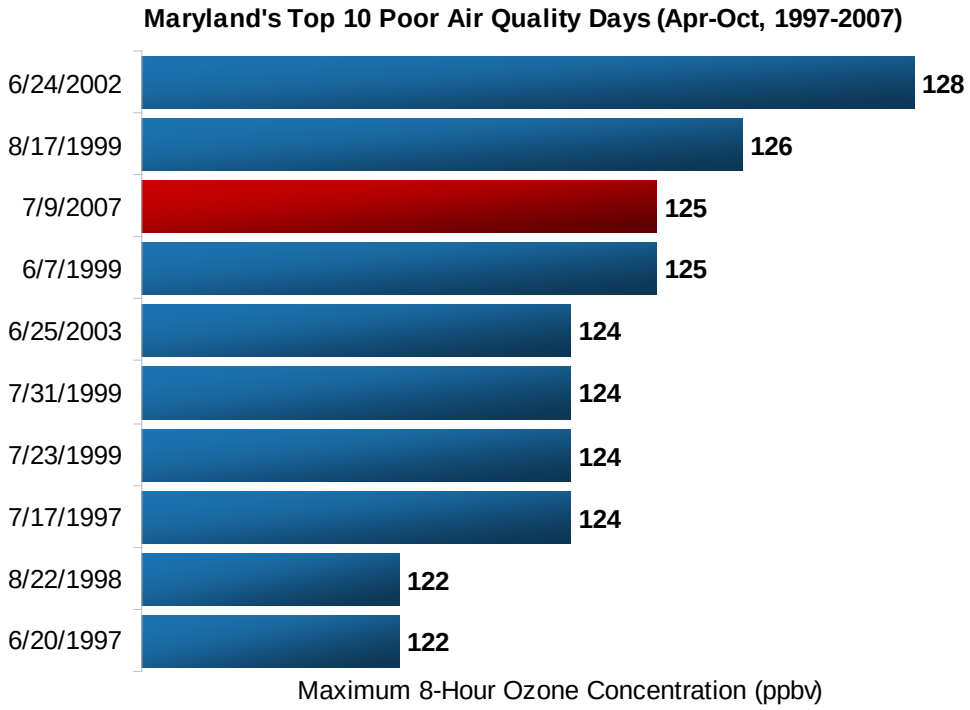

Figure 1.1 Ranking of Maryland's top poor air quality days since 1997.

Regional air pollution in the eastern U.S. has been extensively studied using ground based [e.g. *Diem et al.*, 2009; *Mao et al.*, 2010] and aircraft observations [e.g. *Taubman et al.*, 2006; *Mena-Carrasco et al.*, 2007] as well as regional chemical models [e.g. *Zhang et al.*, 2006; *Yu et al.*, 2007; *Castellanos et al.*, 2010]. Satellite remote sensing of tropospheric O_3, NO_2, CO, HCHO and aerosols is becoming an essential resource for studying urban pollution [e.g. *Al-Saadi et al.*, 2005; *Martin et al.*, 2008; *Molina et al.*, 2007; *Fishman et al.*, 2008; *Kar et al.*, 2010; *Eremenko et al.*, 2008].

The objectives of the work presented in this dissertation are to:

1. Use a regional chemical transport model (WRF/Chem) to simulate a severe smog event of July 7-11, 2007.
2. Measure model performance against surface and ozonesonde measurements across the eastern U.S.
3. Perform a lightning sensitivity simulation to determine the impact of lightning-induced O_3 on surface and tropospheric column O_3.
4. Compare the updated simulation with the Aura satellite O_3, NO_2, and CO products to draw conclusions about the ability of satellites to retrieve pollutant enhanced profiles associated with the July 2007 smog event.

This works consists of 6 chapters. The next background chapter describes meteorological conditions and chemical reactions conducive to smog formation, as well as previous results on modeling and satellite sounding of regional air quality. Chapter 3 discusses the July 2007 smog event, the base WRF/Chem simulation and compares the model with surface measurements. Chapter 4 presents the WRF/Chem lightning sensitivity study and comparison with satellite products. Chapter 5 presents a historic ozone data set from the Winter Monsoon Experiment (WMONEX) 1978/1979 over the South China Sea and discusses these observations in the context of open cell convection. Conclusions and discussion are found in Chapter 6.

Chapter 2 Background

A severe smog episode arises during certain photochemical and synoptic conditions. Analysis of air pollution is facilitated through the use of regional models and satellite observations. This chapter outlines the basic concepts of the above topics.

2.1 Tropospheric Photochemistry

2.1.1 Ozone

Tropospheric ozone formation is driven by oxides of nitrogen ($NO_x = NO + NO_2$), carbon monoxide (CO) and volatile organic compounds (VOC). Major NO_x sources are high-temperature combustion of fossil fuels, microbial processes in soils, lightning, and biomass burning [IPCC, 2007]. Concentrations of O_3 and NO_x depend on the photostationary state [e.g. *Kelly et al., 1980*]:

$$NO_2 + h\nu \ (\lambda < 430 \text{ nm}) \rightarrow NO + O \quad (1)$$

$$O + O_2 + M \rightarrow O_3 + M \quad (2)$$

$$NO + O_3 \rightarrow NO_2 + O_2 \quad (3)$$

where $h\nu$ is a photon and M is a third body molecule (i.e. N_2 or O_2) needed to stabilize ozone. This sequence of reactions results in a steady state, neither producing nor destroying O_3, NO, and NO_2.

Photochemical O_3 production is possible if NO is converted to NO_2 without simultaneous destruction of O_3. Reaction of hydroxyl radical (OH) and organic hydrocarbons, such as carbon monoxide (CO) removes NO:

$$CO + OH \rightarrow CO_2 + H \quad (4)$$

$$H + O_2 + M \rightarrow HO_2 + M \quad (5)$$

$$HO_2 + NO \rightarrow NO_2 + OH \quad (6)$$

Next, NO_2 can photolyze and produce O_3 via reactions (1) and (2).

During the night ozone can react with NO_2 to form dinitrogen pentoxide (N_2O_5) reservoir species.

$$O_3 + NO_2 \rightarrow NO_3 + O_2 \quad (7)$$

$$NO_3 + NO_2 \rightarrow N_2O_5 \quad (8)$$

In the presence of aqueous aerosols, nitric acid is formed.

$$N_2O_5 + H_2O(aq) \rightarrow 2HNO_3(aq) \quad (9)$$

2.1.2 OH and Reactive Nitrogen Species Chemistry

OH is a major oxidant in the atmosphere; it acts as the first step in the removal of many pollutants, such as CO, NO_2, and methane (CH_4). The major source of OH is the photolysis of O_3 in the presence of water vapor [*Seinfield and Pandis*, 1998].

$$O_3 + h\nu \rightarrow O_2 + O(^1D) \quad (10)$$

$$O(^1D) + H_2O \rightarrow 2OH \quad (11)$$

The first step in the reaction with VOCs (Figure 2.1) is the removal of hydrogen atom from an alkane (RH) forming water and alkyl radical (R). R represents an organic compound C_iH_j, where i and j are integers.

$$OH + RH \rightarrow H_2O + R\cdot \quad (12)$$

Alkyl radical readily reacts with oxygen forming an alkylperoxy radical (RO_2).

$$R\cdot + O_2 + M \rightarrow RO_2 + M \quad (13)$$

$$RO_2 + NO \rightarrow RO + NO_2 \quad (14)$$

Alkylperoxy radical reacts with NO to produce NO_2, which can contribute to ozone productions via reactions (1) and (2).

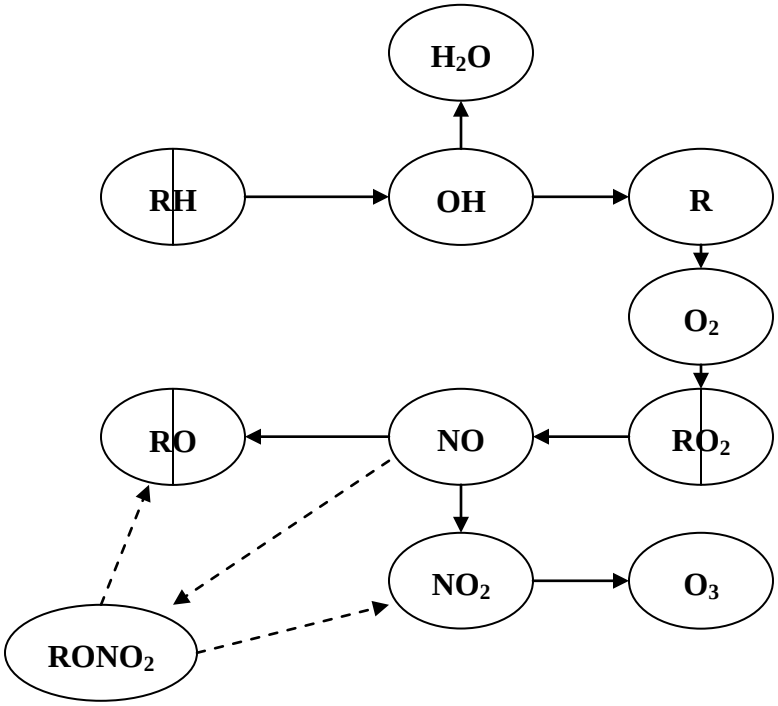

Figure 2.1 Photochemical O_3 production from VOCs and NO_x species.

Alternatively, alkyl nitrates ($RONO_2$) form.

$$RO_2 + NO + M \rightarrow RONO_2 + M \quad (15)$$

Formation of alkyl nitrates is an additional mechanism for transporting reactive nitrogen to higher altitudes. Aloft, photolysis of $RONO_2$ to NO_2 and alkoxy radical (RO) follows.

$$RONO_2 + h\nu \rightarrow NO_2 + RO \quad (16)$$

Next, photochemical production of ozone via reactions (1) and (2) contributes to background ozone concentrations in the remote troposphere.

NO_x is removed from the atmosphere by oxidation to nitric acid (HNO_3).

$$NO_2 + OH + M \rightarrow HNO_3 + M \quad (17)$$

which is removed by heterogeneous deposition. NO_x has a lifetime of hours to few days [*Seinfeld and Pandis*, 1998].

Total reactive nitrogen oxides (NO_y) is the sum of NO_x and its oxidation products, HNO_3, the nitrate radical (NO_3), peroxyacetyl nitrate (PAN), N_2O_5, peroxynitric acid (HNO_4), nitrous acid (HONO), $RONO_2$, and peroxyalkyl nitrates ($ROONO_2$). According to EPA major sources of NO_x in the U.S. include transportation (on-road vehicles 36%, off-road 23 %) and fossil fuel use (electricity generation 21%, fuel combustion 13 %, industrial processes 6 %) [*EPA, 2005*].

2.1.3 NO_x-VOC dependency

Efficiency of tropospheric ozone production has a non-linear dependence on the ratio of VOC to NO_x in the lower troposphere. Relationship between peak NO_x and VOC availability and O_3 production is illustrated by an isopleth plot (Figure 2.2) generated by Empirical Kinetic Modeling Approach [*Finlayson-Pitts and Pitts*, 1993]. Peak ozone is plotted as a function of VOC and NO_x mixing ratios. The eight-to-one line separates the plot into two theoretical regions: urban (or VOC limited) on the left and rural (or NO_x limited) on the right. In the theoretical urban region NO_x emissions from fuel combustion in motor vehicles and industrial processes are large. In theoretical rural regions, concentrations of biogenic VOCs are

greater than NO_x emissions. VOC to NO_x ratio of approximately 8:1 is a reference point for determining the shift in sensitivity of an air mass to precursor levels and possible benefits of NO_x vs. VOC controls. Establishing relative position of a specific region's VOC to NO_x ratio on the isopleths plot is the first step in implementation of an air quality control program. The goal is to move perpendicular towards lower isopleths lines to reduce O_3 peak concentration.

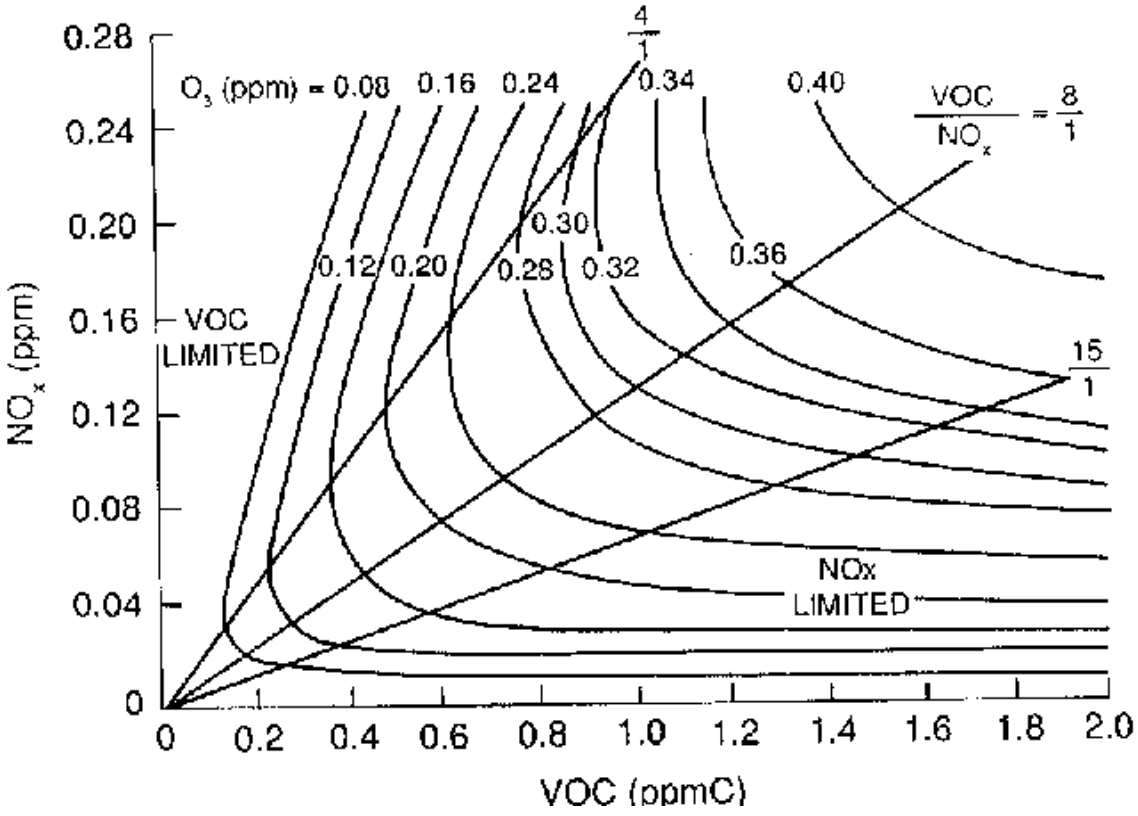

Figure 2.2 Non-linear dependence of tropospheric O_3 production on NO_x and VOC availability. Adapted from [Finlayson-Pitts and Pitts, 1993].

2.1.4 CO

CO is an excellent tracer for long-range transport because it is sparingly soluble in water, easily detected, measured with high precision and good temporal resolution, and has a distinct profile in the troposphere. CO is produced primarily by

ground sources and destroyed throughout the troposphere, so its abundance decreases with altitude. It is a product of incomplete combustion, with sources such as vehicles, biofuels, and biomass burning. Thus CO is a good proxy for pollution from urban, industrialized areas and biomass burning. CO has a lifetime of a few months, long enough for tracking pollution plumes on synoptic and intercontinental scales, but short enough to provide pollution enhancements in plumes relative to background. Vertical flux of CO can be used as a tracer of pollutant outflow from source regions.

2.2 *Meteorology and Transport of Pollution*

2.2.1 High Pressure System

Air quality in the Mid-Atlantic region strongly depends on regional weather patterns. An episode of high ozone can occur when a high pressure weather system sets just west of the Appalachian Mountains. High pressure systems are characterized by clear sky, hot, humid conditions. Cloudless skies transmit more ultraviolet radiation and high temperatures accelerate smog photochemistry at the surface. Large scale subsidence associated with high pressure contributes to atmospheric stability and low surface winds. Clockwise circulation around the high pressure pushes air from the industrialized Mid-West and the Ohio River Valley into the Mid-Atlantic region. Strongest Mid-Atlantic pollution episodes occur when the Bermuda High pressure system combines with the existing high pressure over the eastern U.S (Figure 2.3). Hot, humid air from the Gulf of Mexico moves clockwise around the Bermuda High into the Mid-Atlantic.

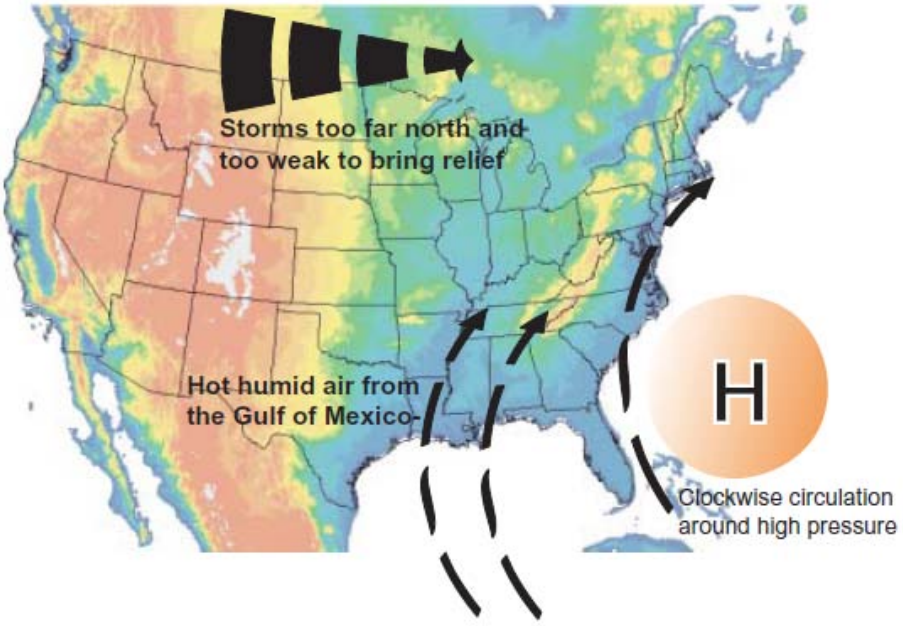

Figure 2.3 A semi-permanent area of high pressure forms over the Atlantic Ocean during the summer. The clockwise circulation around the high pressure brings southwesterly winds to the East. Adapted from Guide to Mid-Atlantic air quality [Stehr, 2005].

2.2.2 Diurnal Cycle

The Planetary Boundary layer (PBL) or mixing layer has a diurnal cycle following the cycle of solar heating at daytime and cooling at nighttime at the surface. Following sunrise, the mixing layer grows rapidly to a maximum depth of 1.5-2.5 km by mid-afternoon. By sunset, the mixing height is reduced to less than 500 m and a stably-stratified layer develops near the surface, extending upward to about 200 m [*Rao et al*., 2003]. Mixing layer diurnal cycle contributes to diurnal cycle of surface pollutants, such as O_3. At nighttime pollutants are trapped in the shallow mixed layer below a nocturnal inversion. O_3 and NO_2 are removed via equations 7-9 and subsequent deposition of nitric acid. A residual layer forms between a nocturnal inversion and subsidence inversion associated with the high pressure system. The residual layer serves as a reservoir of photochemically aged species and also entrains

pollution from upwind sources transported by the low level jet, discussed below. In the morning the ground warms, breaking the nocturnal inversion. Clean air in the PBL and polluted air in the residual layer rapidly mix (Figure 2.4), contributing to an O_3 maximum in the early morning. Subsequently, the daytime mixing layer accumulates local and regionally transported emissions [e.g., Ryan *et al.*, 1998].

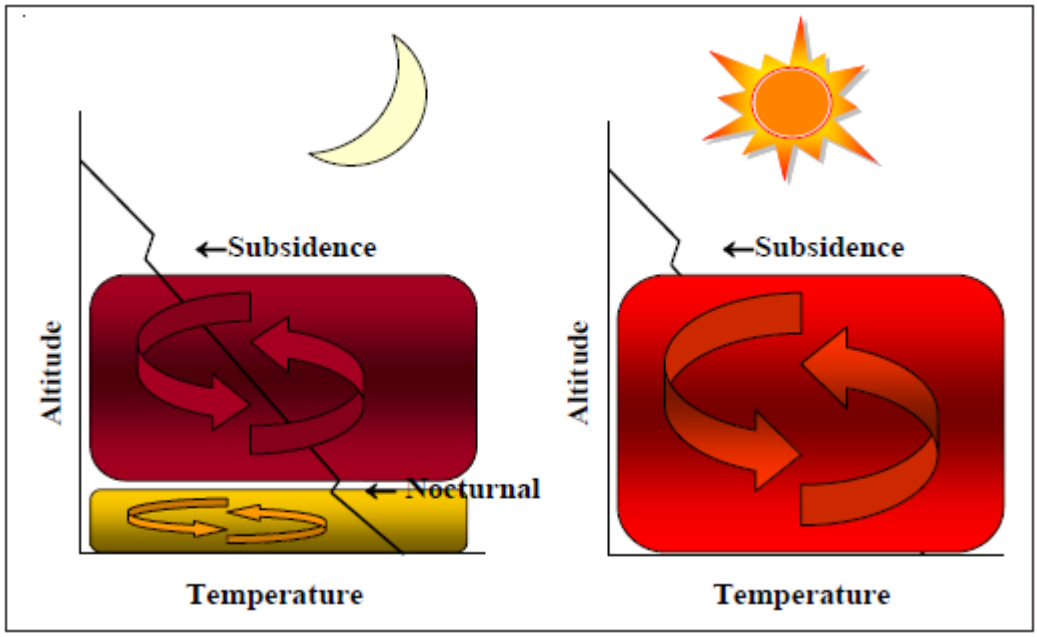

Figure 2.4 Daily cycle of inversions and mixing. Low O_3 concentrations (denoted in yellow) below nocturnal inversion are isolated from polluted air below the subsidence inversion (in dark red). As nocturnal inversion is destroyed in the morning hours, there is mixing of the two layers and surface O_3 concentrations surge (orange). Adapted from Regional Air Quality Guide [Stehr, 2005].

2.2.3 Low Level Jet and Appalachian Leeside Trough

Smaller scale systems, the nocturnal low level jet (LLJ) and Appalachian Leeside Trough (ALT), also affect regional air quality. The LLJ forms above the nocturnal inversion in the warm sector of a midlatitude cyclone caused by large temperature gradients spanning from behind the cold front to the warm sector. At nighttime the LLJ is strengthened by cooling of high elevation air in the Appalachian Mountains

relative to air at the same geopotential height along the east coast [*Holton*, 1967]. The LLJ is a south-westerly flow of 10-20 m/s observed between 300-1000 m lasting from approximately midnight to 6 am LST. This system is capable of moving pollutants from the southeast U.S. approximately 300 km into the Washington-Baltimore urban region.

The ALT forms on the leeward side of the Appalachian Mountains, as an air mass blows over the mountains, compresses, and warms adiabatically. Additional buoyancy makes the air rise creating a mesoscale region of low pressure at the surface. To conserve absolute vorticity, the winds blowing from the west, turn counter-clockwise across the trough and blow from the southwest along the east coast. Transport of pollutants from the Midwest and Southeast U.S via the LLJ and ALT is important during stagnant smoggy conditions [*Gaza*, 1997].

2.2.4 Continental Pollution Outflow

The local chemical budget of O_3 in the lower troposphere depends directly on vertical transport of O_3 from the pollution source or indirectly on transport of chemical precursors. In the PBL pollutants are short-lived, if they are transported to the upper troposphere their atmospheric residence times increase. For instance, in the marine boundary layer ozone photochemical lifetime is about a week, increasing with height to 1 month at 6 km and 1 year at 10 km [*Kley et al.*, 1996]. Therefore, the lifetime of lower tropospheric ozone is enhanced by upward convective transport. On the other hand, the lifetime of upper tropospheric ozone decreases as it is transported to the lower troposphere where it is more efficiently destroyed [*Lelieveld and*

Crutzen, 1994]. Similarly residence times for nitrogen and sulfur compounds are shortest in the PBL, where they are destroyed by surface deposition.

Pollution transport from source regions occurs either in the planetary boundary layer (PBL) or in the free troposphere (FT). Pollutants travel farther at higher altitudes due to stronger upper level winds. In the PBL wind speeds are reduced by friction with the earth's surface. In addition, a temperature inversion often isolates air in the PBL and limits its mixing with the rest of the troposphere.

Vertical transport of pollutants can be represented by eddy diffusion: mixing due to turbulent motions; species gradually move from regions of high concentration to low to reduce the gradient. If this were the sole vertical mixing method, molecules from the earth's surface would slowly mix to 10 km in a few months. More efficient transport paths exist, for instance in thunderstorms this transport time is reduced to hours. The main mechanisms responsible for lifting surface emissions into the middle and upper troposphere are deep convection, fronts and orographic forcing, followed by irreversible mixing. These mechanisms act at different spatial and temporal scales: cloud scale and several hours for deep convection, synoptic scale and several days for fronts.

2.2.4.1 Deep Convection and Lightning NO_x

Deep convection is an important mechanism for tropospheric air transport. Rapid convective updrafts redistribute trace gases within the troposphere [*Chatfield and Crutzen, 1984*; *Dickerson, et al.*, 1987]. NO from lifted pollution or lightning (LNO_x) can produce O_3. The formation of NO following a lightning flash can be described by the following Zeldovich mechanism:

$$O_2 \rightarrow 2\,O \quad (18)$$

$$O + N_2 \rightarrow NO + N \quad (19)$$

$$N + O_2 \rightarrow NO + O \quad (20)$$

$$N + OH \rightarrow NO + H \quad (21)$$

This sequence of reactions can only occur at very high temperatures. The magnitude of NO_x production from lightning is believed to be 5±3 Tg yr^{-1} [*Schumann and Huntrieser*, 2007]. Uncertainties exist in the amount of NO_x produced per flash, average flash length and global distribution of flash rates making approximation of LNO_x very difficult [*Price et al*., 1997]. Recent studies [e.g. *DeCaria et al.*, 2005; *Cooper et al.*, 2006; *Hudman et al.*, 2007; *Ott et al.*, 2010; *Allen et al.*, 2010] used NO_x production per flash of 460-500 moles NO per flash for modeling analyses of midlatitude convective storms.

2.2.4.2 Fronts and the Warm Conveyor Belt

Frontal systems play an important role in the vertical redistribution of pollutants. In general, high winds associated with the passage of cold fronts clean the boundary layer and contribute to vertical mixing, thus decreasing surface concentrations. Frontal lifting of pollution over the Mid-Atlantic ahead of eastward moving cold fronts, followed by eastward transport in the lower FT, is the principal

process responsible for export of anthropogenic pollution from U.S.

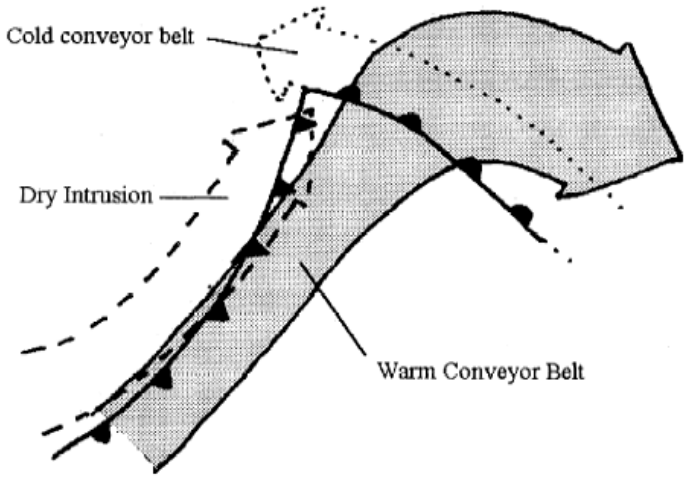

Figure 2.5. Diagram of relative isentropic flow in a midlatitude cyclone. Adapted from [*Browning*, 1990].

Ahead of cold fronts, vertical transport of PBL pollution to the FT occurs within the main ascending branch of an extratropical cyclone, i.e. the warm conveyor belt [*Cooper et al.*, 2004]. A Warm Conveyor Belt (WCB) is defined as rising streams of warm and humid air along lines of constant entropy ahead of the cold front. WCB begins in the PBL equatorward of the cyclone, travels along and ahead of the cold front, ascending and turning anticyclonically ahead of a warm front, if present (Figure 2.5).

For tracing air motion within WCB flow (for both dry and moist adiabatic processes) the wet bulb potential temperature (θ_w) is a conserved property [*Harrold*, 1973] θ_w is attained when a parcel is brought down to 1000 mb from its lifting condensation level along a pseudoadiabat. *Bethan et al*. [1998] showed that ozone was lifted from the PBL to the FT by a warm conveyor belt during the development of a baroclinic wave in the North Atlantic. The authors concluded that while

conveyor belts exhibit well-defined chemical signatures, several chemical tracers (such as O_3, CO, NO_y) and meteorological tracers (i.e. θ_w, RH) must be measured to identify air mass differences. Similarly, Western Europe frequently receives outflow from North America brought over by WCB [*Stohl*, 2001]. Associated with outflow ahead of the front in the FT is the PBL continental outflow behind the front, usually capped at about 2 km altitude by strong subsidence [*Liu et al.*, 2003]. This plume does not travel far, fanning out over the region as the front dissipates.

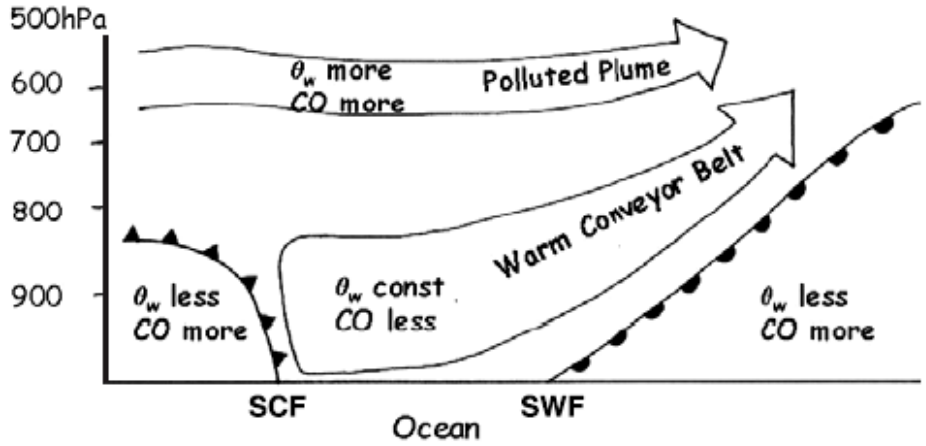

Figure 2.6. Vertical cross section of WCB. SCF – surface cold front, SWF – surface warm front. Clean WCB over the ocean splits pollution plume in the FT. Adapted from [*Mari et al.*, 2004].

2.3 *Regional Chemical Transport Modeling*

Regional air pollution in the eastern U.S. has been extensively studied using numerical prediction models [e.g. *Ryan et al.*, 2000,. *Zhang et al.*, 2006; *Yu et al.*, 2007; *Castellanos et al.*, 2010]. In this dissertation the Weather Research and Forecasting (WRF) model with online Chemistry (WRF/Chem) and the Community Multiscale Air Quality (CMAQ) regional models will be used to analyze air quality.

WRF/Chem provides the capability to simulate chemistry and aerosols from cloud scales to regional scales. WRF/Chem has been developed by NOAA with contributions from NCAR, PNNL, EPA, and university scientists. This numerical model system is ‘‘online’’ in the sense that it simulates trace gases and aerosols simultaneously with meteorological fields in the WRF framework, allowing for feedback between meteorology and chemistry at each time step. Transport of species is done using the same vertical and horizontal coordinates as the meteorological parameters (such as winds) with no spatial interpolation, and with the same physics parameterization with no temporal interpolation. Moreover, online calculation of photolysis frequencies is preferred, because absorption cross-sections of O_3 are temperature dependent and aerosol extinction is humidity dependent. WRF/Chem is an extension of MM5/Chem regional-scale chemical transport model [*Grell et al.*, 2000] to version 3 of the nonhydrostatic WRF community model.

CMAQ modeling system was designed to support a wide variety of modeling tasks ranging from scientific to regulatory inquiries. CMAQ can model multiple air quality subjects: tropospheric ozone, fine particulate matter, toxics, acid deposition, and visibility degradation. CMAQ modeling system incorporates output fields from emissions and meteorological modeling systems through special processors into the CMAQ Chemical Transport Model (CCTM). Then CCTM computes chemical transport modeling for multiple pollutants on multiple scales. The structure of CMAQ allows for flexibility in substituting different emissions processing systems and meteorological models. Yet the model is “offline”, since meteorology fields are computed separately from the chemistry.

Regional models tend to underestimate high ozone values, which poses a problem for operational air quality forecasts. PBL height biases, lateral boundary condition assumptions, and deficiencies in chemical mechanism and emissions can contribute to model uncertainty. *Zhang et al.* [2006] linked underprediction of 1-hr O_3 daily maxima on high O_3 days to overestimated planetary boundary layer depth. *Cai et al.* [2008] found that deficiencies in the Carbon Bond Mechanism 4 (CB-IV) [*Carter*, 1996] can cause underestimation of NO_z ($NO_z = NO_y - NO_x$) removal and OH concentrations, key contributors to ozone production. *Castellanos et al.* [2010] showed that O_3 underprediction in CMAQ is due to removal of NO_x that proceeds too quickly in the CB-IV mechanism. *Gilliland et al.* [2008] showed that CMAQ underpredicts NO_x above the PBL. *Yu et al.* [2007] in a regional air quality modeling simulation with the Eta-CMAQ model performed for the International Consortium for Atmospheric Research on Transport and Transformation (ICARTT) study found that the model reproduced O_3 vertical distributions at low altitudes, but overestimated O_3 above 6 km due to biases in the lateral boundary conditions and a relatively coarse vertical resolution. *Grell et al.* [2005] in WRF/Chem simulations for the summer of 2002 NEAQS field study in northeast U.S. showed reduction in model mean bias and root mean square error in an experiment changing leaf temperature, which determines biogenic emissions of isoprene, important for O_3 formation. *Grell et al* [2005] used the Regional Acid Deposition Model Version 2 (RADM2) chemical mechanism [*Stockwell et al*, 1990]. RADM2 represents organic chemistry through a reactivity aggregated molecular approach [*Middleton et al*, 1990], grouping similar organic compounds into model groups using reactivity weighting. RADM2 includes 21

inorganic species (14 stable species, 4 reactive intermediates, and 3 abundant stable species (O_2, N_2, and H_2O)) and 42 organic species (26 stable species and 16 peroxy radicals). RADM2 chemical mechanism will be used in this dissertation for WRF/Chem modeling simulations.

2.4 *Satellite Measurements*

Currently polar-orbiting low earth orbit (LEO) satellites are widely used for remote sensing of air quality. Polar-orbiting satellites move in a fixed circular orbit approximately 1000 km above the earth in sun synchronous orbit with orbital pass at about same local time each day. A sun-synchronous orbit is defined as a polar orbit that crosses the equator at the same time each overpass. Due to closer proximity to the Earth's surface, polar-orbiting satellites provide higher vertical and horizontal resolution than geostationary satellites; but the temporal resolution is poor – about 12-24 hour measurement cycle for a given location. Polar orbiting satellites may provide full global coverage over 1-16 days, depending on swath width; clouds can inhibit collection of useful information.

Remote sensing refers to using electromagnetic radiation to study atmospheric constituents such as O_3, CO, nitrogen dioxide (NO_2), and formaldehyde (HCHO) without being in physical contact with these gases. Satellite instruments measure spectral characteristics of scattering, absorption and emission of electromagnetic radiation from atmospheric species. Geophysical quantities are extracted from the measured radiances.

Instruments discussed herein employ passive techniques, measuring either solar backscatter ($\lambda < 4$ μm) or thermal infrared radiation ($\lambda \sim 4$-50 μm).

Atmospheric radiative transfer can be expressed as attenuation of solar radiation traversing the atmosphere, known as Beer's Law:

$$I = I_0 e^{-\tau} \tag{22}$$

where I is the backscattered intensity measured by the satellite instrument, I_0 is the intensity of backscattered radiation that would be measured in the absence of absorption, τ is the optical thickness of the slant column. The log of the optical thickness is shown for O_3, NO_2, SO_2, and HCHO in Figure 2.7. Ozone is the main absorber for wavelengths shorter than 350 nm. NO_2 exhibits distinct spectral structure between 425 and 450 nm, wavelengths at which retrievals are generally conducted.

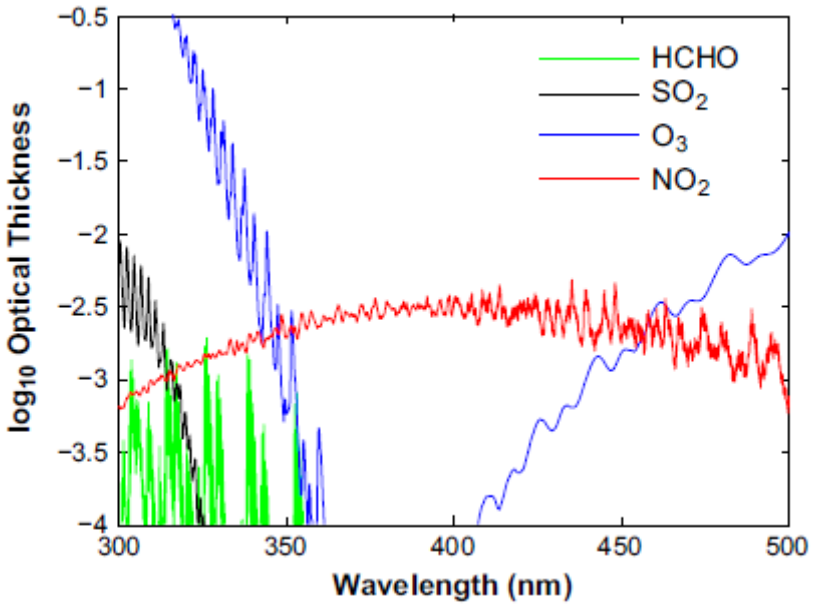

Figure 2.7 Optical thickness of selected trace gases at ultraviolet and visible wavelengths for nominal atmospheric concentrations ($1x10^{16}$ molec/cm^2 for HCHO and SO_2; $5x10^{15}$/cm^2 for NO_2; and 300 DU for O_3. Adapted from [Chance, 2006] and [Martin et al., 2008].

At ultraviolet and short visible wavelengths the land surface reflectivity is less than 5 % [*Koelemeijer et al.*, 2003], molecular scattering is the major component of backscattered radiation. Sensor sensitivity to trace gases in the lower troposphere is highest in the ultraviolet and short visible window. Clouds enhance instrument sensitivity to species above clouds and decrease sensitivity below clouds [*Martin et al.*, 2002; *Millet et al.*, 2006].

Figure 2.8 summarizes the process of conversion of raw sensor data into products fit for comparison with model and in situ data. Sensor data is transmitted to the ground as detector "counts" (Level 0 data) and assigned spatial and temporal header information.

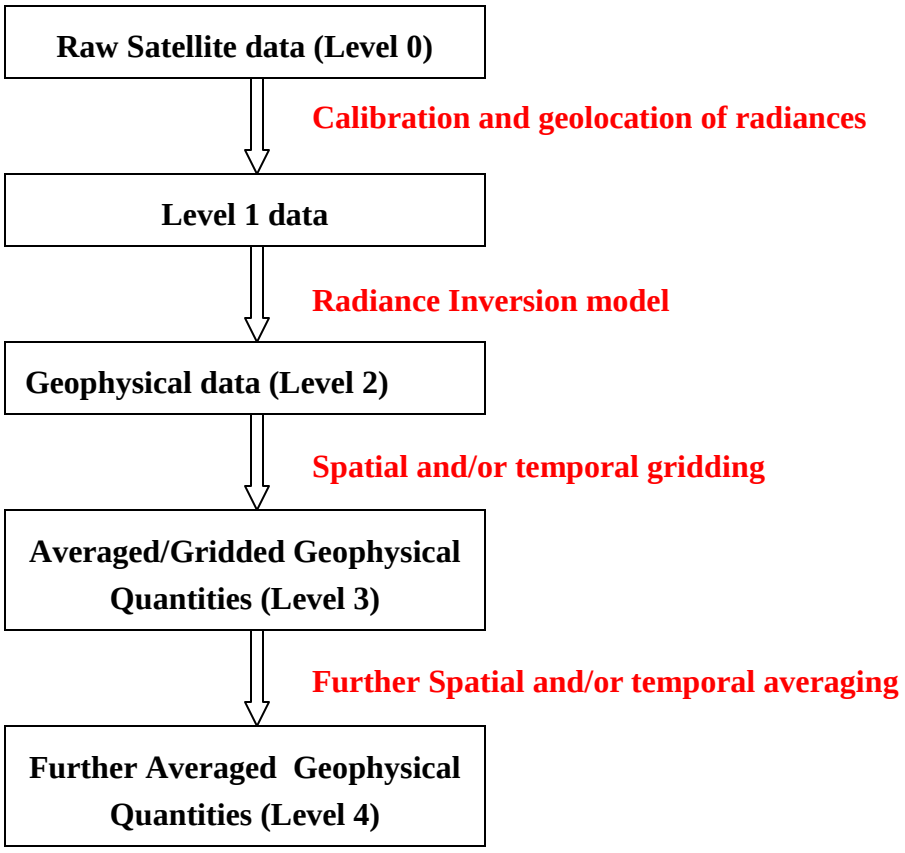

Figure 2.8 Flowchart of satellite measurement processing for comparison with in situ and model data.

The sensor data are transformed into engineering units, calibrated, corrected for biases, and directly linked to geospatial information (i.e. latitude, longitude, date, and time). The resulting Level 1 data are passed through a radiance inversion model producing geophysical quantities (Level 2), such as column O_3. Level 2 data also contain quality-control flags useful for quality control and regridding purposes. These data are most widely used for research due to flexibility of data filtering and manipulation. Level 3 data result from further post-processing such as regridding to a different grid resolution and temporally averaging to produce daily and monthly means. Level 3 data can be utilized for larger-scale climatological studies. Level 4 data are further processed (i.e. averaged in time and space) Level 3 data.

Retrieval of geophysical quantities from measured radiances is constrained with *a priori* information, such as the climatological mean profile shape of the retrieved gas. The retrieved vertical profile represents a vertically averaged quantity of the true profile since the satellite sensor has a finite field of view. When comparing satellite measurements and model simulations with greater vertical resolution than satellite retrievals, retrieval averaging kernels need to be applied to the high-resolution model output so the model is sampled with the same vertical sensitivity as the instrument is sampling the real atmosphere. The averaging kernel (AK) is a mathematical representation of how the vertical structure of the atmospheric profile is mapped into the measured radiances [*Deeter*, 2002]. The averaging kernel used here is a matrix where each row defines the averaging kernel for one particular retrieval level, and each element in this row defines the contribution of other retrieval levels to the retrieved quantity. To compare the satellite profiles with model output,

model ozone profiles (x_{model}) are convolved with the measurement averaging kernel matrix (A) to obtain the same vertical resolution profiles (x'_{model}) as satellite retrievals:

$$x'_{\text{model}} \approx x_{apriori} + \mathrm{A}(x_{\text{model}} - x_{apriori}) \tag{23}$$

Where $x_{apriori}$ is the retrieval *a priori* profile.

In the past, satellite instruments could not directly retrieve tropospheric ozone from space due to the large signature of stratospheric ozone in the total column. Prior studies, using measurements from these instruments determined tropospheric ozone column distributions by subtracting the stratospheric ozone column from the total ozone column [e.g., *Fishman and Larsen,* 1987; *Hudson and Thompson*, 1998; *Ziemke et al.*, 2006; *Schoeberl et al.*, 2007]. The total amount of O_3 in a column air is expressed in Dobson units (DU), where 1 DU equals 2.69 x 10^{16} molecules/cm^2. Total column ozone is approximately 300 DU, of which about 30 DU or 10 % is within the troposphere.

Hyperspectral infrared or ultraviolet instruments such as Tropospheric Emission Spectrometer (TES) [*Beer et al.*, 2001; *Worden et al.*, 2004] and the Ozone Monitoring Instrument (OMI) [*Levelt et al.*, 2006; *Schoeberl et al.*, 2007; *Liu et al.*, 2009] aboard the Aura satellite can measure tropospheric ozone in the free and upper troposphere with coarse vertical resolution. It is still difficult to measure boundary-layer and surface-layer ozone from space. The ability of satellites to detect tropospheric O_3 is critical towards understanding ozone formation in polluted regions, venting into the free troposphere, subsequent transport, and possible descent back into the boundary layer.

2.5 *Summary*

In summary, the summertime problem of poor air quality the Mid-Atlantic region is a combination of meteorological conditions and smog photochemistry. Since no aircraft in situ measurements are available for the analysis of the worst smog event in the past decade (July 2007), a combination of regional chemical modeling and satellite measurements analysis will be performed. In the next chapter I will be using a regional chemical model to simulate a severe air pollution episode. This episode will be further studied with the use of satellite observations in Chapter 4.

Chapter 3 Characterization of an eastern U.S. severe air pollution episode using WRF/Chem

3.1 *Introduction*

The ability to predict lower-tropospheric ozone in a region of high population density such as the Mid-Atlantic is important due to the adverse impacts of ozone on human health. Areas downwind of Washington, D.C., Baltimore, Philadelphia, and New York City report the highest summertime O_3 concentrations in the region. Local vehicle emissions of O_3 precursors, NO_x and volatile organic compounds (VOCs) and transport of power plant generated NO_x from the Ohio River Valley contribute to O_3 production. During the July 7-11, 2007 smog episode the heat island effect in downtown Washington, D.C. contributed to higher recorded O_3 mixing ratios in Baltimore, MD [*Zhang et al*., 2009].

In this chapter, the Weather Research and Forecasting model with chemistry module (WRF/Chem) and the Advanced Research WRF (ARW) core version 3.1.1 [*Grell et al.*, 2005] will be used to study the July 7-11, 2007 smog episode. The performance of this regional air quality model (using RADM2 chemical mechanism) will be evaluated with a focus on simulating O_3 and reactive nitrogen species. WRF/Chem-calculated trace gases and meteorological parameters will be compared to ground observations and ozonesonde profiles. In the next chapter, I will use WRF/Chem to investigate the ability of satellite instruments to detect signatures of the July 2007 smog event from space.

3.2 *WRF/Chem Simulation*

The Weather Research and Forecasting model with online chemistry is a mesoscale numerical weather prediction system designed both for atmospheric research and operational forecasting. This numerical modeling system is ‘‘online’’ in the sense that all processes affecting the gas phase and aerosol species calculation are done in step with the meteorological dynamics, allowing for feedbacks between chemistry and meteorology at each time step [*Grell et al.*, 2005].

WRF/Chem simulations were nested with a 36x36 km outer domain and a 12x12 km inner domain. The outer domain has 170x103 mass points covering the conterminous U.S., and the inner domain has 169x169 mass points extending from the Midwest to Atlantic Ocean, including the Mid-Atlantic region of the U.S. There are 32 vertical layers with 10 layers below 900 hPa. The depths of the lowest 10

Atmospheric Processes	**WRF/Chem**
Radiation	LW: RRTM ; SW: Goddard
Surface Layer	Monin-Obukhov
Land Surface Model	Noah
Boundary Layer	YSU
Cumulus	Grell 3D ensemble
Microphysics	Lin
Photolysis	Fast-J
Meteorological initial and boundary conditions	NARR
Chemical initial and boundary conditions	MOZART-4
Dry Deposition Scheme	Wesely
Chemical Mechanism	KPP RADM2

Table 3.1 WRF/Chem configuration options.

layers are 2 hPa, 3 hPa, 5 hPa, 6 hPa, 10 hPa, 11 hPa, 15 hPa, 18 hPa, 22 hPa, and 26 hPa. The spacing of the vertical layers increases to about 30-50 hPa from the middle

troposphere to the top of the domain (at 100 hPa). The model was initialized on July 6 at 0 UTC and run for 7 days. Initialization using global chemical model fields reduces the need for a long spin up time period.

Model configuration options for the base case simulations (E_BASE) are listed in Table 3.1. Emissions were processed using the Sparse Matrix Operator Kernel Emissions (SMOKE) Modeling System with 2007 Continuous Emissions Monitoring Systems (CEMS) measurements and projected 2009 emissions (closest available to 2007) for all sources from the U.S. Regional Planning Offices (RPO). More information on the emissions used in this study is available at http://www.marama.org/reports/MANEVU_Emission_Projections_TSD_022807.pdf. Initial and boundary conditions for the meteorological parameters were taken from the North American Regional Reanalysis (NARR). Initial and boundary conditions for trace gas and particulate species were taken from the global MOZART-4 model with output at 6-hr time intervals provided by Louisa Emmons (NCAR) [*Emmons et al.*, 2010].

Objective Analysis (OBSGRID) nudging techniques were used to minimize the accumulation of model errors and preserve mesoscale circulations within the model. OBSGRID nudging improves initial and boundary conditions by combining high-resolution upper level (i.e. rawinsonde, aircraft) and surface observations (i.e. temperature, dew point, winds) with global analysis fields of temperature, water vapor, and winds [*Wang et al.*, 2009]. OBSGRID analysis is an important option for lowering analyses error and generating more accurate meteorological data for air

quality simulations. Four-Dimensional Data Assimilation (FDDA) analysis and surface nudging techniques were not used in the base simulation.

To investigate the causes of biases between model and measured O_3 and NO_y species I also performed three sensitivity experiments:

E_DRYDEP: In addition to E_BASE configurations I doubled O_3 dry deposition velocities over all surfaces within the domain. This simulation tests the sensitivity of model O_3 amounts to uncertainties in dry deposition velocities.

E_ CHEM: The default WRF/Chem chemical mechanism (RADM2), used in this work, does not include the influence of two potentially important reactive nitrogen reservoirs: organo-nitrates ($RONO_2$ – including isoprene nitrates) and nitryl chloride ($ClNO_2$). Heterogeneous reactions of N_2O_5 can lead to two different products: HNO_3 and $ClNO_2$. When HNO_3 is created, NO_x is lost and the O_3 production cycle is stopped. When $ClNO_2$ is the product, NO_2 is regenerated in the morning hours allowing production of O_3 to continue [*Thornton et al*., 2010]. Currently, atmospheric chemical models attribute 30-50% of NO_x removal in polluted regions to nitric acid formation ($N_2O_5+H_20 \rightarrow 2HNO_3$) [*Alexander, et al., 2009*]; nitric acid is subsequently deposited. For E_CHEM, in addition to E_BASE configurations I set the rate of this reaction to zero, thus crudely approximating the maximum possible impact of recycling of NO_x through $ClNO_2$ chemistry on modeled surface O_3 mixing ratios. Moreover, in the atmosphere isoprene nitrates comprise 12-20 % of the NO_y budget over the eastern U.S. [*Perring et al.,* 2009]. Isoprene nitrates are a major removal pathway for nitrogen oxides from the atmosphere. The importance of isoprene increases with decreasing latitude in the Eastern U.S. due to spatial

distribution of high isoprene emitting vegetation and temperature dependence of isoprene emissions [*Guenther et al.,* 2006]. Implementation of these NO_x pathways in chemical mechanisms should enhance O_3 in the northeast U.S., by extending the lifetime of NO_x and its availability for O_3 formation, and reduce O_3 bias in the southeast U.S. by short circuiting the PAN to O_3 pathway.

E_FDDA: In addition to E_BASE configurations I included FDDA analysis nudging technique. Temperature, water vapor, and winds were nudged toward NARR analysis fields for the outer 36-km domain. This simulation investigates the effects of using analysis nudging on prediction of chemical fields.

The strength of FDDA nudging is set by the magnitude of nudging coefficients for horizontal winds (u and v), temperature (T) and water vapor (q). The nudging coefficients for the WRF/Chem simulations were selected based on the Ozone Transport Commission (OTC) WRF Protocol developed for the Maryland Department of the Environment (MDE) in support of regional State Implementation Plan (SIP) air quality modeling forecasts [*MDE*, 2010].

Domain	**Variable Nudged**	**Nudging Coefficient**
Outer Domain	U and V winds	5.0×10^{-4}
Outer Domain	Temperature	5.0×10^{-4}
Outer Domain	Water vapor mixing ratio	1.0×10^{-5}
Inner Nest	U and V winds	2.5×10^{-4}
Inner Nest	Temperature	2.5×10^{-4}
Inner Nest	Water vapor mixing ratio	1.0×10^{-5}

Table 3.2 WRF nudging coefficients for u,v, T, and q fields.

The nudging coefficients for u,v, T and q are summarized in Table 3.2.

3.3 *In-situ observations*

Ozone and reactive nitrogen observations from rural and urban sites are used to evaluate the model's performance in simulating urban and rural air characteristics during a major smog event in the eastern U.S. Domain-wide model output was evaluated using ozone observations from the Air Quality System (AQS). AQS is an Environmental Protection Agency (EPA) program that collects hourly near-realtime surface pollutant observations from several hundred stations across the U.S. AQS data are available for download at http://www.epa.gov/ttn/airs/airsaqs/. Detailed air quality evaluation was performed using data from an AQS site at Aldino, MD (suburban, 39.6°N, 76.2°W); Pinnacle State Park, NY (rural, 42.1°N, 77.2°W, elev. 504 m) [*Schwab et al., 2009*]; Great Smoky Mountains, TN (rural, 35.6°N, 83.9°W, elev. 793 m) (data available from http://www.nature.nps.gov/air/Monitoring/MonHist/index.cfm); and Southern Aerosol Research and Characterization (SEARCH) sites in Atlanta, GA (urban, 33.8°N, 84.4°W) and Yorkville, GA (rural, 33.9°N, 85.0°W) (data available at http://www.atmospheric-research.com/studies/search/). These are the few stations in eastern U.S. that continuously monitor true NO_y mixing ratios without loss of HNO_3 as is typical of most commercial NO_x analyzers [e.g. *Poulida et al.*, 1994; *Schwab et al.*, 2009]. Vertical characteristics of the extent of the polluted air mass are analyzed using Beltsville, MD ozonesondes [*Yorks et al.*, 2009].

3.4 *Ozone Episode during July 7-11, 2007*

Figure 3.1 and Figure 3.2 depict surface analysis maps and model synoptic events, respectively, for July 6 – 12, 2007. According to the National Centers for Environmental Prediction (NCEP) surface analysis maps, a cold frontal system moved off the East Coast on July 6, 2007 12 UTC (Figure 3.1a), shifting winds to northwest and decreasing humidity. WRF/Chem surface analysis shows the wind shift in the Washington, DC area associated with the passage of the cold front (Figure 3.2a). On July 7, 2007 a high pressure system was centered over the Ohio River Valley and the Great Lakes area. Maximum temperatures reached 30°C and no precipitation was observed. Ensuing high temperatures, clear skies, and plentiful sunlight contributed to onset of ozone production.

a) July 6, 2007 12 UTC

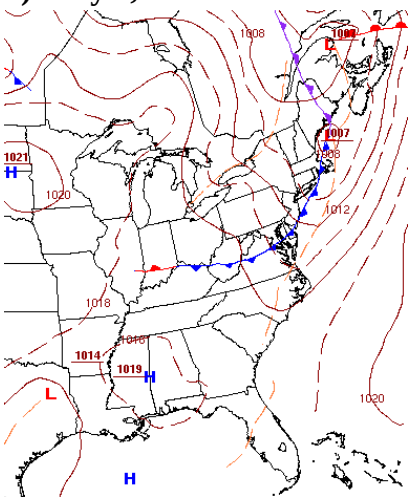

b) July 8, 2007 18 UTC

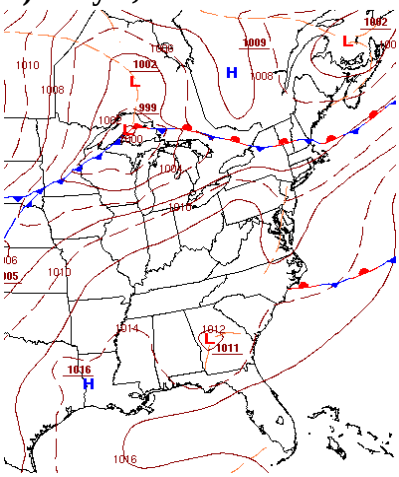

c) July 9, 2007 18 UTC

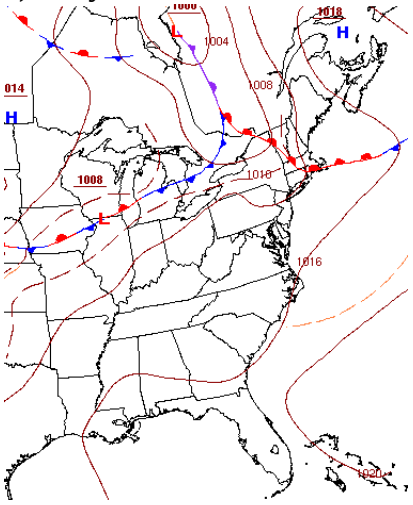

d) July 10, 2007 18 UTC

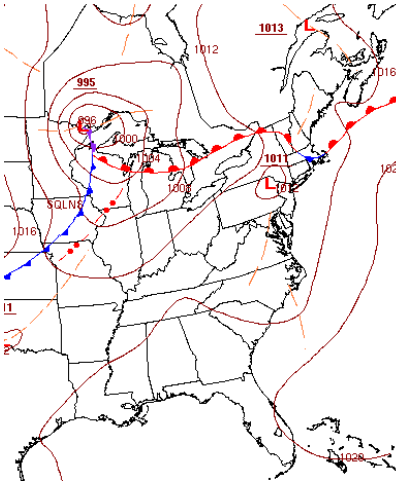

e) July 11, 2007 18 UTC

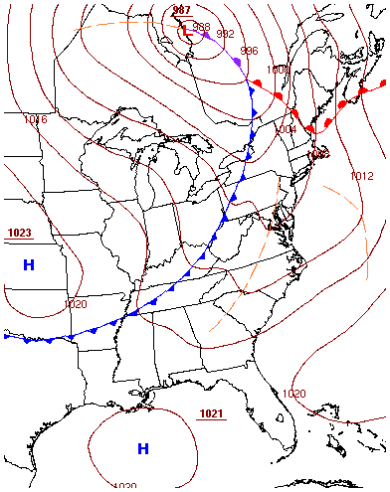

f) July 12, 2007 3 UTC

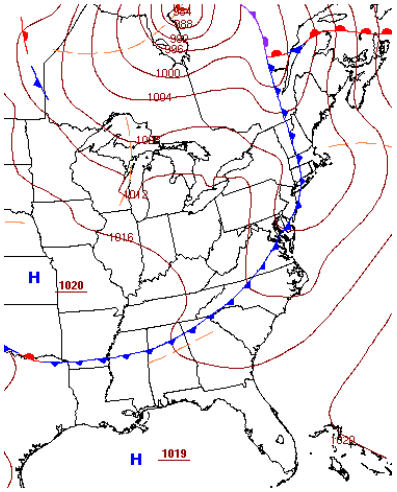

Figure 3.1 NOAA North American analysis of surface pressure on a) July 6, 2007 12 UTC. b) July 8, 2007 18 UTC, c) July 9, 2007 18 UTC, d) July 10, 2007 18 UTC, e) July 11, 2007 18 UTC and f) July 12, 2007 3 UTC, contoured by 4 hPa.

On July 8, a midlatitude cyclone began forming over the Great Lakes (Figure 3.1b, Figure 3.2b). Maximum temperatures remained near 30°C in the Mid-Atlantic region. High temperatures, sunny skies, and moderate southwest winds set the stage for strong photochemical ozone formation. As the cyclone moved to the northeast over Canada, the anticyclone off the southeast U.S. coast moved over the Mid-Atlantic region. On July 9 and 10, temperatures in the Mid-Atlantic region reached 35-37°C. GOES-12 infrared image on July 9, 18 UTC shows clear sky conditions in the Washington/Baltimore metropolitan area (Figure 3.3). On July 9 and 10, temperatures in the Mid-Atlantic region reached 35-37°C. Sunny, stagnant conditions contributed to accumulation of ozone with weak surface winds from the southwest (Figure 3.1c, Figure 3.2c). On July 10 and 11, a surface trough was aligned just east of the Appalachian Mountains (Figure 3.1d, Figure 3.2d); large-scale southwest flow dominated along the eastern sea-board, transporting pollutants from the southeast to New England. The model is in agreement with the surface analysis as to the location of the isobars (Figure 3.1e, Figure 3.2e). The cold front associated with the midlatitude cyclone near James Bay pushed through the Baltimore Washington Metropolitan area around 3 UTC on July 12, 2007 (Figure 3.1f, Figure 3.2f). The smog event ended as the cold front brought cleaner, cooler air into the region. Overall, WRF/Chem satisfactorily simulated the synoptic circulation patterns that contributed to the July 2007 smog episode in the Mid-Atlantic region.

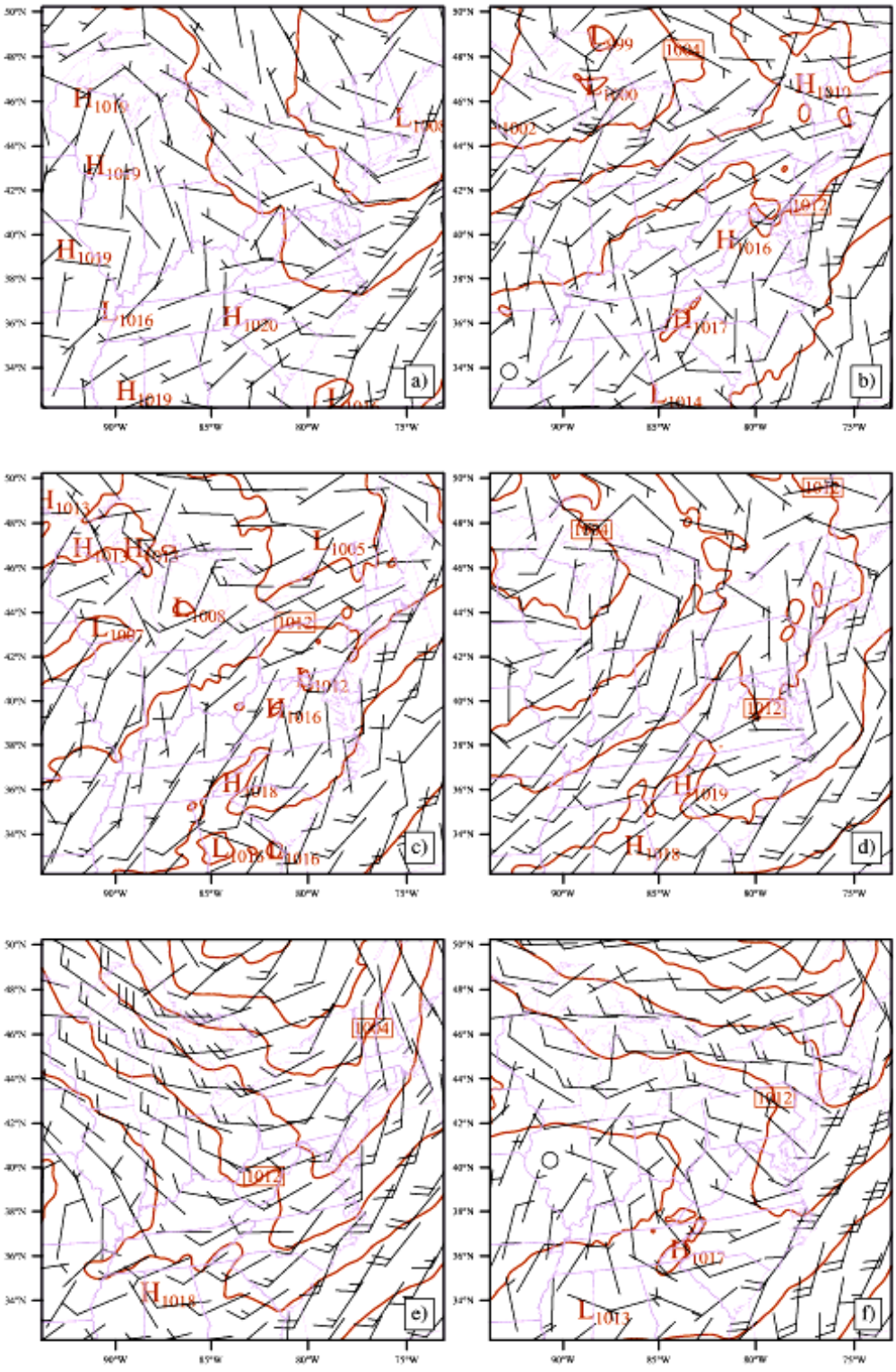

Figure 3.2 WRF/Chem sea level pressure (contoured by 4 hPa, black lines), and surface wind vectors on a) July 6, 2007 12 UTC. b) July 8, 2007 18 UTC, c) July 9, 2007 18 UTC, d) July 10, 2007 18 UTC, e) July 11, 2007 18 UTC and f) July 12, 2007 3 UTC.

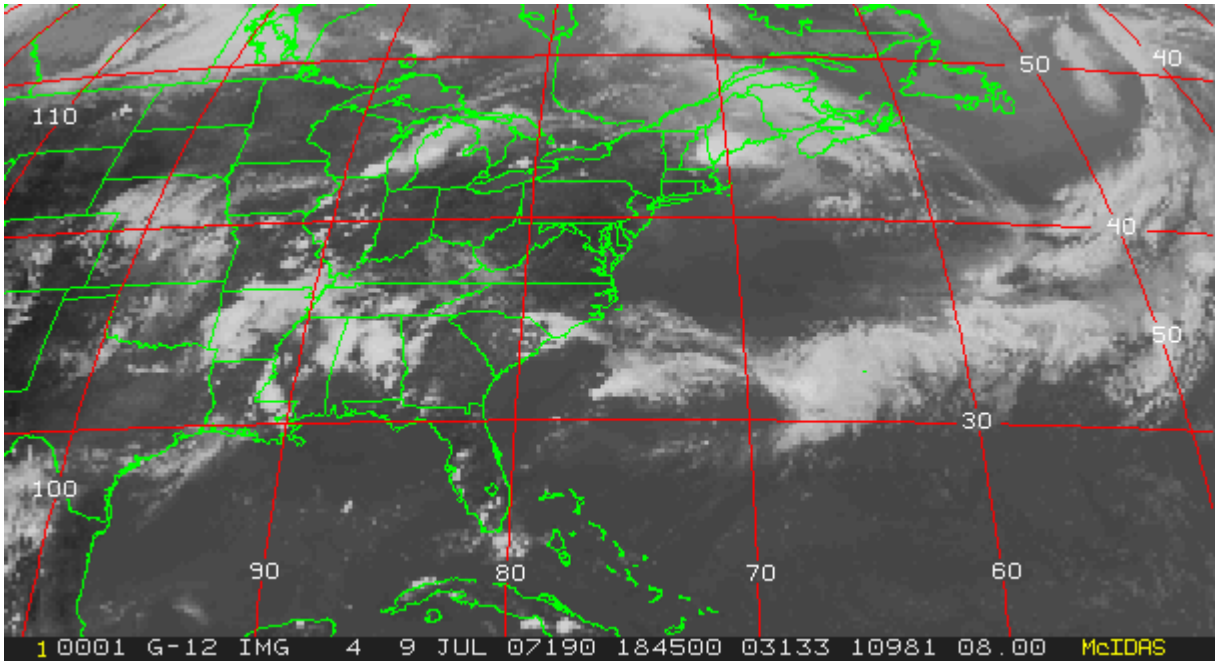

Figure 3.3 GOES-12 infrared image for July 9, 2007 18:45 UTC.

3.5 *Model comparison to AQS surface observations*

3.5.1 Characteristics of simulated ozone

The WRF/Chem simulation is evaluated against surface ozone monitoring stations. For each day of the simulation, 8 hour maximum surface ozone fields were calculated and interpolated to the location of AQS measurements within the nested domain. On July 6, surface stations were reporting ozone values in the moderate 55-65 ppbv range in the Baltimore-Washington, D.C. region and New England states (Figure 3.4a). WRF/Chem shows ozone enhancement off the coast of New England states, visible in the AQS coastal measurements extending from Virginia to Massachusetts (Figure 3.5a). North Carolina, South Carolina, Georgia and Tennessee also reported increased ozone – remnants of an earlier July 4-5 pollution episode.

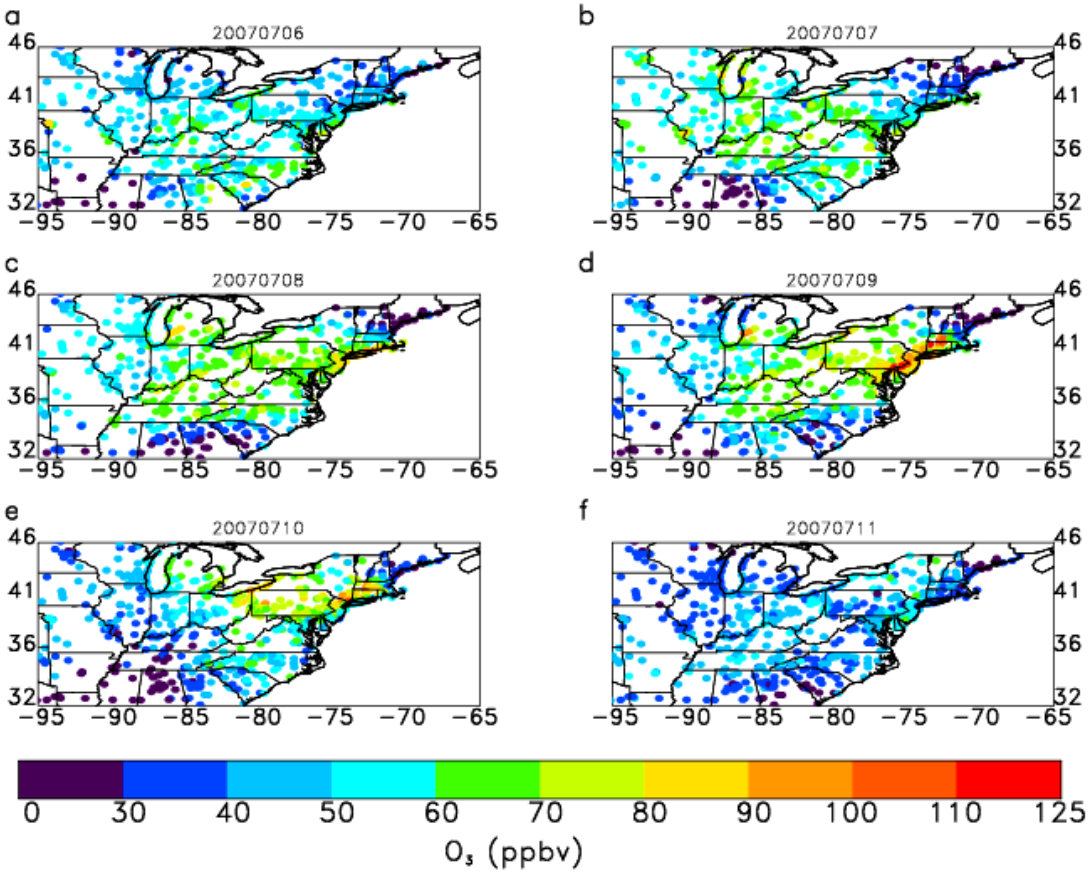

Figure 3.4 Observed surface 8-hr O_3 daily maxima for July 6-11, 2007.

WRF/Chem mean bias on the first day of the simulation is 2.93 ppbv; the model overestimates O_3 in the northeast and southeast by 20-25 ppbv and underestimates O_3 in the Ohio River Valley 5-10 ppbv (Figure 3.6a). The onset of increased photochemistry and stagnation associated with the high pressure system is visible in the gradual increase of surface ozone in observations (Figure 3.4b-Figure 3.4e) and model (Figure 3.5b-Figure 3.5e) from July 7 through July 10. July 9 was one of the worst air quality days recorded in the Mid-Atlantic region in the past decade. AQS 8-hr maximum ozone peaked at 100-125 ppbv along the I-95 interstate corridor, from

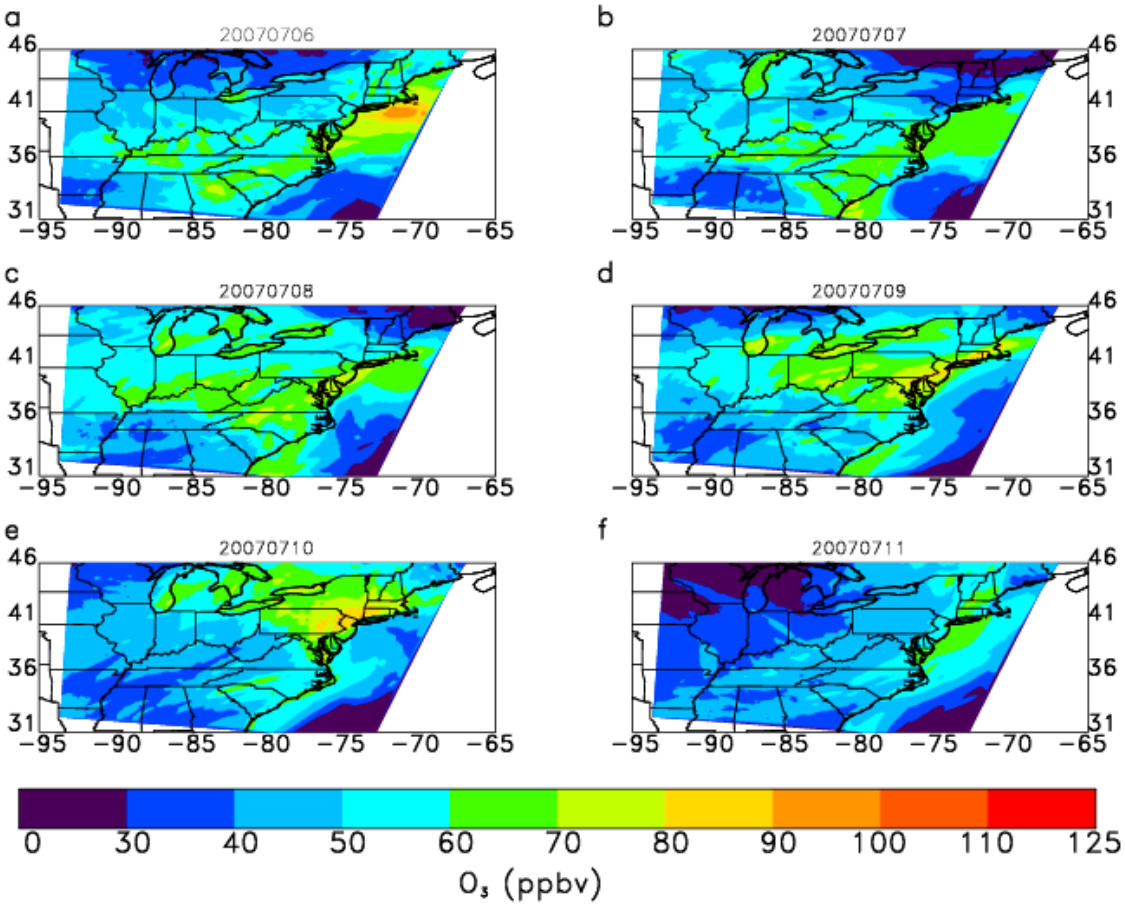

Figure 3.5 Modeled surface 8-hr O_3 daily maxima for July 6-11, 2007.

the Washington-Baltimore metropolitan area to Boston. On this day, the model correctly simulates the spatial distribution of the ozone peak along I-95 north of Maryland, but the peak 8-hr maximum values are underpredicted by 15-20 ppbv (Figure 3.6d). On July 10, the model underpredicts O_3 distributions by 10-23 ppbv along the Ohio River Valley, where a midlatitude cyclone warm front passed. On July 11, observations and model show good air quality conditions following frontal passage across the region.

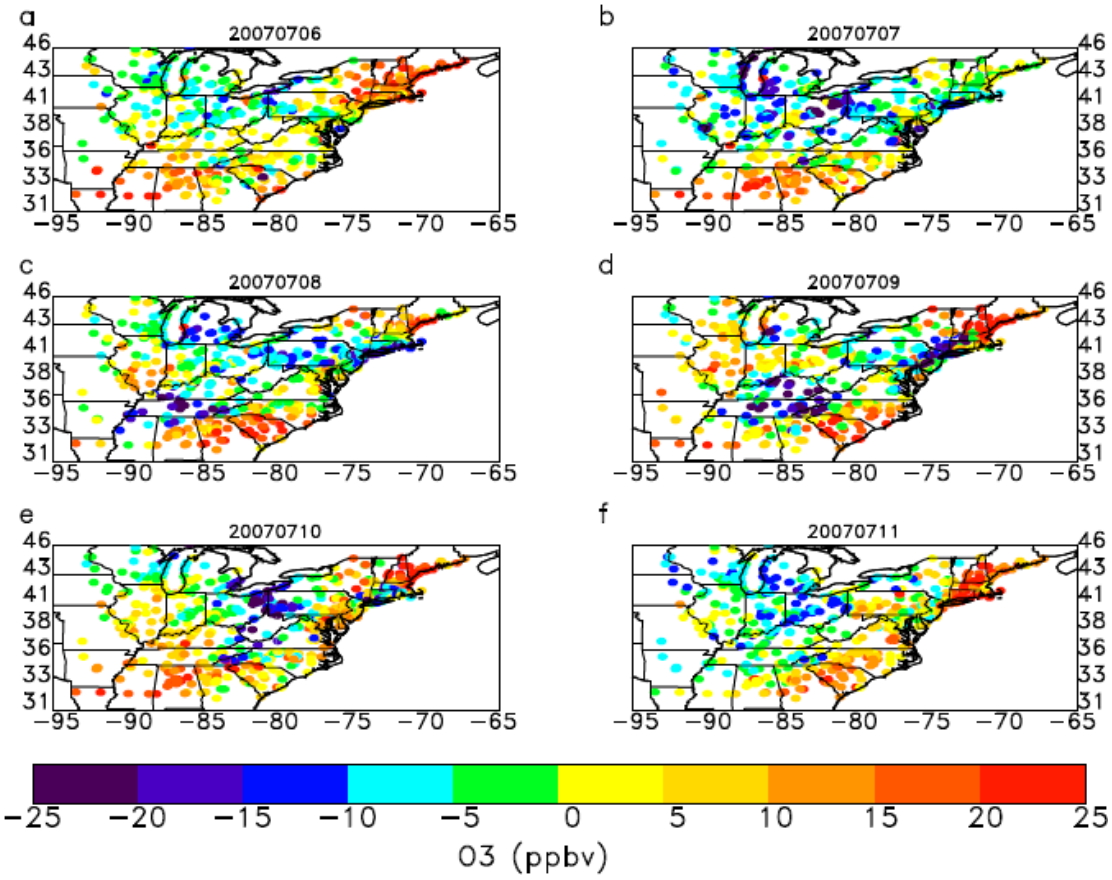

Figure 3.6 Difference between modeled and observed surface 8-hr O_3 daily maxima for July 6-11, 2007.

Measure of modeled and observed 8-hr maximum difference is defined as average mean bias (MB):

$$MB = \frac{1}{N}\sum_{1}^{N}(Mod - Obs), \quad (1)$$

where *Mod* and *Obs* are modeled and observed ozone mixing ratios.

Table 3.3 examines daily average mean biases over two regions: northeast U.S. states (MD, DE, PA, NJ, NY) and southeast (NC, SC, GA, AL, MS) for the E_BASE and E_FDDA simulations. Opposing regional biases exist in the northeast and southeast in E_BASE and E_FDDA simulations. WRF/Chem (E_BASE) underpredicts O_3 in

the northeast by 4.62-6.93 ppbv, and overpredicts O_3 in the southeast by 6.3-10.5 ppbv.

WRF/Chem (E_FDDA) simulated 8-hr maximum O_3 is slightly better on July 8 and 9 in the northeast with a low bias of 3.43-3.75 ppbv. But July 10 and July 11 O_3 mean biases exceed 11 ppbv in the northeast. Ozone overprediction in the southeast is worsened using FDDA analysis nudging, mean biases are 17.2-24.3 ppbv. Previous photochemical modeling studies conducted for central California have shown that the photochemical model performance did not improve when they used the meteorological fields generated with FDDA [*Tanrikulu et al.,* 2000; *Umeda and Martien,* 2002]. These results highlight the sensitivity of photochemical O_3 production to model generated meteorological fields. Sensitivity of WRF to nudging settings will be examined in more detail in section 3.5.5.

	MB (ppbv) (E_BASE)		MB (ppbv) (E_FDDA)	
	Northeast	**Southeast**	**Northeast**	**Southeast**
20070706	1.14	6.86	0.19	9.26
20070707	-4.62	10.5	-6.09	17.2
20070708	-5.56	9.16	-3.43	19.6
20070709	-6.93	6.30	-3.75	24.3
20070710	0.13	7.28	11.0	21.4
20070711	1.27	7.52	11.8	19.9
All	-2.43	7.94	1.62	20.5

Table 3.3 Daily mean bias for observed and simulated 8-hr maximum ozone at AQS sites for the base WRF/Chem simulation (E_BASE) and WRF/Chem with FDDA nudging (E_FDDA). Bias calculated for two regions: northeast (MD, DE, PA, NJ,NY) and southeast (NC,SC,GA,AL,MS).

3.5.2 Statistical Analysis

3.5.2.1 Discrete Statistics

A scatter plot of the modeled and observed 8 hr O_3 daily maxima at monitoring sites within the 12-km nested domain during July 6-11, 2007 is shown in Figure 3.7. The calculated regression line has a slope of 0.53 and intercept of 25.0. WRF/Chem overestimates low O_3 values and underpredicts high values with a correlation coefficient of 0.70. Previous studies evaluating other regional models, such as CMAQ and MM5-Chem produced similar order of agreement with observations [e.g. *Kang et al.*, 2005, *Mao et al.*, 2010, *Gilliland et al.*, 2008, *Godowitch et al.*, 2008, *Castellanos et al.*, 2010].

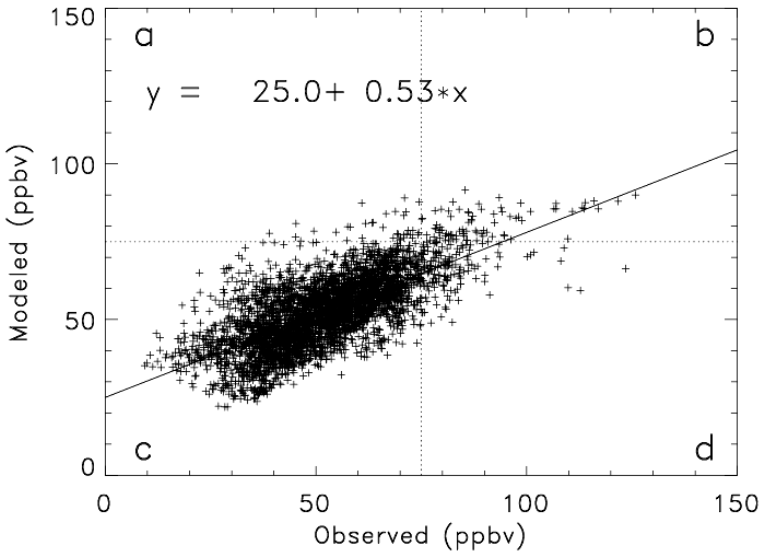

Figure 3.7 Scatter plot of the modeled versus observed 8-hr maximum O_3 for July 6-11, 2007. Exceedance thresholds, least-squares regression line and coefficients are shown.

Figure 3.8 shows the distribution frequency of observed and simulated 8-hr O_3 daily maxima. Observed 8-hr O_3 daily maxima ranged from 9 to 125 ppbv, with the

peak frequency of occurrence of 12 % within 50 – 55 ppbv bin. Modeled 8-hr O_3 daily maxima were within the 22-92 ppbv range, with a peak frequency of 17 % centered at 55-60 ppbv bin. Six percent of AQS measurements and 3 % of model forecasts were in exceedance of the NAAQS 8-hr maximum ozone standard of 75 ppbv. The model underpredicts the frequency of 8-hr maximum ozone mixing ratios less than 40 ppbv and greater than 65 ppbv, but overestimates the frequency in the 40-65 ppbv range. Model O_3 forecasts less than 40 ppbv generally occurred west of the Appalachian Mountains and in northern New England states (Figure 3.9). Model forecasts greater than 65 ppbv occurred in urban areas along I-95 corridor and in the Ohio River Valley. Model forecasts between 40 ppbv and 65 ppbv occurred across the domain. This category included high O_3 biased model forecasts in the southeast U.S. on days of good air quality and low O_3 biased forecasts in the northeast U.S. on days of poor air quality.

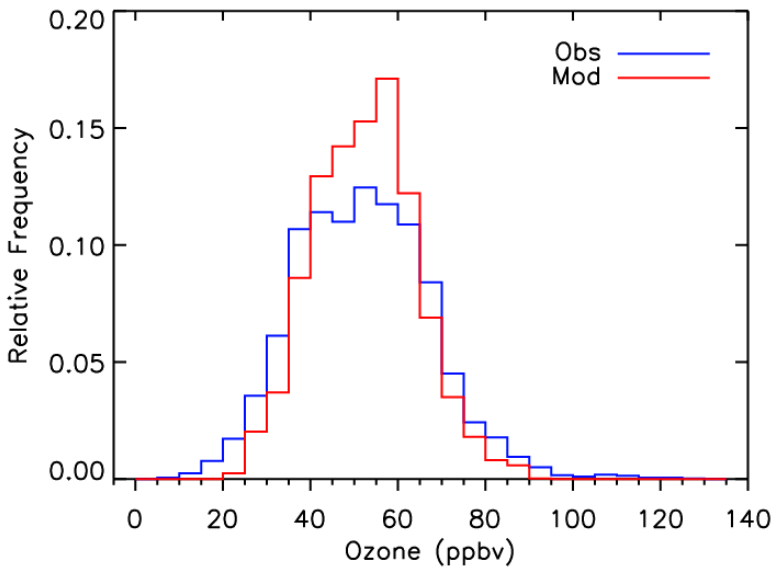

Figure 3.8 Frequency distribution of observed and modeled 8-hr O_3 daily maxima for July 6-11, 2007.

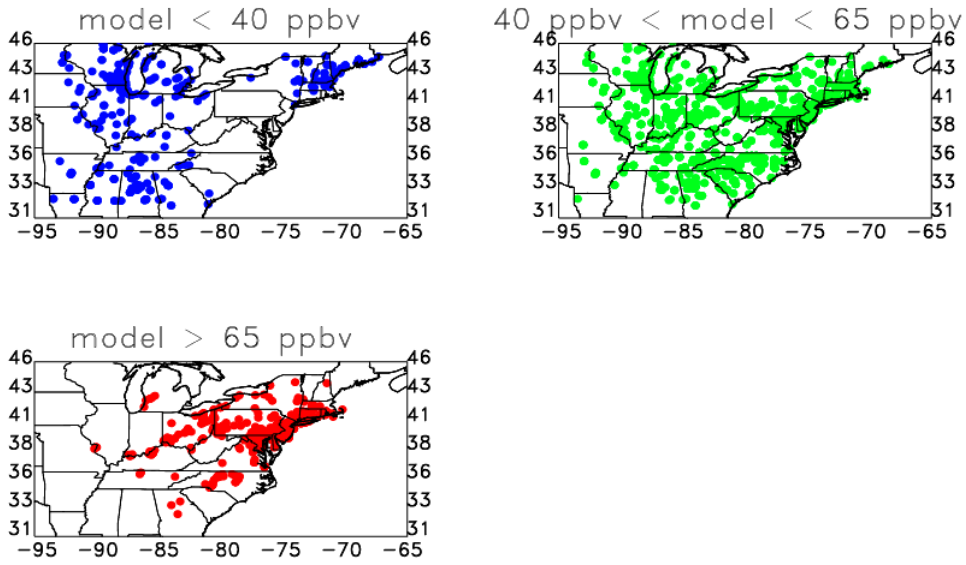

Figure 3.9 Locations of WRF/Chem 8-hr O_3 daily maxima for July 6-11, 2007 where a) model < 40 ppbv, b) 40 < model < 65 ppbv, and c) model > 65 ppbv.

Evaluation of discrete forecasts (observed versus modeled mixing ratios) was done using mean bias, normalized mean bias (NMB), root mean square error (RMSE), normalized mean error (NME), correlation coefficient (r), and standard deviation (σ).

The measures of bias and errors are defined as follows:

$$NMB = \frac{\sum_{1}^{N}(Mod - Obs)}{\sum_{1}^{N} Obs} \times 100\% \quad (2)$$

$$RMSE = \sqrt{\frac{1}{N}\sum_{1}^{N}(Mod - Obs)^2} \quad (3)$$

$$NME = \frac{\sum_{1}^{N}|Mod - Obs|}{\sum_{1}^{N} Obs} \times 100\% \quad (4)$$

where *Mod* and *Obs* are modeled and observed ozone concentrations.

Table 3.4 summarizes discrete observation-model O_3 comparisons. Average mean bias for the episode is 0.59 ppbv, with a standard deviation of ±11.0 ppbv, average NMB is 1.14 %.

Date	MB (ppbv)	NMB (%)	RMSE (ppbv)	NME (%)	r	σ (ppbv)
20070706	2.93	5.86	10.2	15.2	0.48	9.78
20070707	-2.29	-4.22	10.2	14.9	0.69	9.94
20070708	-0.86	-1.5	10.5	14.5	0.73	10.4
20070709	0.23	0.38	13.1	16.9	0.74	13.1
20070710	2.45	4.8	11.9	17.9	0.71	11.7
20070711	1.06	2.57	9.75	18.6	0.37	9.7
All	0.59	1.14	11.0	16.2	0.7	11.0
NAQFC	5.5	11.9	12.7	20.9	0.7	

Table 3.4 Discrete evaluation results for observed and simulated 8-hr maximum ozone at AQS sites for individual days and all days. NAQFC (WRF-CMAQ) performance from [Eder et al, 2009] is also shown for comparison.

Biases on individual days are also small ranging from 2.93 ppbv on July 6 to -2.29 ppbv on July 7 (Table 3.4). This good agreement is partially the result of overpredicted and underpredicted values in different regions of the domain canceling each other as was shown in Table 3.3. Regional biases will be discussed in more detail in section 3.5.3. Current regional air quality model simulations produce similar results [i.e. *Mao et al., 2010*; *Zhang et al.,* 2006]. In terms of error, average WRF/Chem RMSE and NME values (11.0 ppbv and 16.2 %) for this case study are on the lower end of previous studies (12 -18 ppbv and 18-25 %), respectively [e.g. *Kang et al., 2005; Eder et al., 2009; Mao et al., 2010*]. The correlation coefficient (r) between observations and model was approximately 0.7 for July 7-10 but was less than 0.5 on July 6 and July 11. The model performs the best on days when air quality is poor; on these days it simulates correctly the spatial pattern of surface O_3. In

general, the model performance is better than NOAA's National Air Quality Forecast Capability (NAQFC) WRF-CMAQ model performance for July 2007 [*Eder et al., 2009*], with lower NME, RMSE and NMB (Table 3.4).

3.5.2.2 Categorical Statistics

Categorical forecast evaluation was performed for the model nested domain using definitions of accuracy (A), bias (B), hit rate (H), false alarm rates (F), false alarm ratio (FAR), and critical success index (CSI) based on observed and modeled exceedances and nonexceedances. EPA's current National Ambient Air Quality Standard for 8 hr maximum ozone of 75 ppbv was used as the threshold for exceedances. Variables (*a*,*b*,*c*, and *d*) used to calculate categorical metrics are defined as follows: *a* represents a forecast 8-hr exceedance (> 75 ppbv) that did not occur; *b*, a forecast 8-hr exceedance that did occur; *c*, a forecast 8-hr nonexceedance that did occur; and *d*, a nonforecast 8-hr exceedance that did occur (Figure 3.7).

Accuracy (A) is the percentage of true forecasts and given by:

$$A = \left(\frac{b+c}{a+b+c+d}\right) \cdot 100\% \tag{5}$$

Bias (B) is the measure of model's false negative and false positive forecasts. B < 1 indicates underprediction, B > 1 indicates overprediction, and B = 1 indicates no bias.

$$B = \left(\frac{a+b}{b+d}\right) \tag{6}$$

The false alarm rate (F) is the percentage of incorrectly forecast nonexceedances.

$$F = (\frac{a}{a+c}) \cdot 100\% \quad (7)$$

Since F is strongly influenced by correctly forecasted nonexceedances (c), false alarm ratio (FAR) is the percentage of times an exceedance was forecast when none occurred.

$$FAR = (\frac{a}{a+b}) \cdot 100\% \quad (8)$$

Critical success index (CSI) measures how well forecasted and measured exceedances were predicted.

$$CSI = (\frac{b}{a+b+d}) \cdot 100\% \quad (9)$$

Lastly, the hit rate (H) is the percentage of observed exceedances that were forecasted.

$$H = (\frac{b}{b+d}) \cdot 100\% \quad (10)$$

Table 3.5 summarizes categorical evaluations for each day of the episode and for all data. On July 6, 7 and 11, very few air quality violations were observed, so significance of statistics metrics on these days is limited.

For example, the very good accuracy (> 97 %) on these days is somewhat misleading, since *c*, the number of correctly forecast nonexceedances, is very large with respect to *a*, *b*, and *d*. Critical success index and hit rate are better metrics of model performance without consideration of correctly forecast observed nonexceedances. Overall, for this episode CSI is 30.6 %; July 9 stands out with the highest CSI of 43.0 %.

Date	A (%)	B	F (%)	FAR (%)	CSI (%)	H (%)	a	b	c	d
20070706	99.2	0.67	0.34	100	0	0	2	0	594	3
20070707	97.3	0	0	N/A	0	0	0	0	580	16
20070708	92.6	0.11	0.18	20	8.3	8.5	1	4	548	43
20070709	88.5	0.62	2.83	21.2	43.0	48.6	14	52	480	55
20070710	91.9	0.77	3.3	41.9	33.8	44.6	18	25	527	31
20070711	99.8	0	0	N/A	0	0	0	0	599	1
All	94.9	0.5	1.04	30.2	30.6	35.2	35	81	3328	149
NAQFC	97.4	1.9		80.9	14.2	35.5				

Table 3.5 Categorical evaluation results for observed and simulated 8-hr maximum ozone at AQS sites. Results for July 6, 7 and 11 are not statistically significant, since a and b ≈ 0. NAQFC (WRF-CMAQ) performance from [Eder et al, 2009] is also shown for comparison.

Hit rate measures the percentage of correctly forecast observed exceedances. On July 9 and 10 the model has 48.6 % and 44.6 % hit rate. Bias indicates if forecast exceedances are underpredicted (B < 1) or overpredicted (B>1). On all days the model's forecast exceedances are underpredicted, with the greatest bias on July 10. The false alarm rate is the fraction of nonexceedances that were incorrectly forecast, in other words, forecast smog events that failed to develop. The false alarm rate increased through the duration of the smog episode. On July 9 and 10, FAR values increase from 21.2 % to 41.9 %, due to overestimated 8-hr exceedance forecasts in the I-95 corridor. WRF/Chem categorical statistics for the July smog event are comparable with NOAA's NAQFC model performance, with greater critical success index, lower false alarm ratio and bias, and slightly lower hit rate (Table 3.5).

3.5.3 Model-observation time series comparison

In this section, 1-hr daily measurements from stations in Maryland, New York, Tennessee and Georgia for July 6-13, 2007 are used to evaluate WRF/Chem. Model-observation comparison on an hourly basis can better capture synoptic and chemical processes than smoothed 8-hr maximum data.

3.5.3.1 Aldino, MD

Time series of O_3 and NO_y (NO_y = NO + NO_2 + PAN + HNO_3 + 2*N_2O_5 + HONO + organic nitrates) during July 6-July 13, 2007 at a suburban AQS station in Aldino, MD are shown in Figure 3.10.

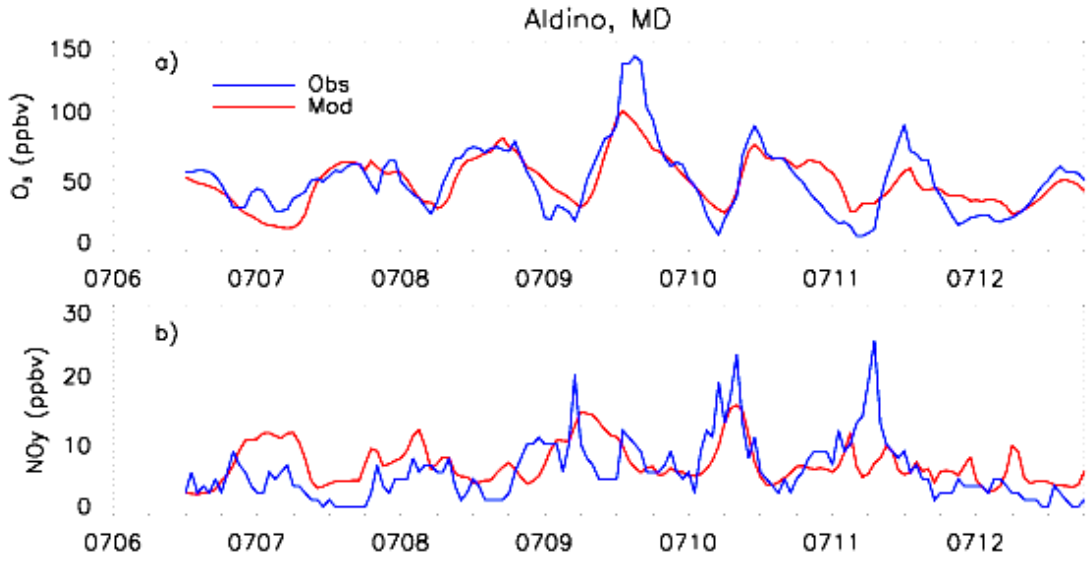

Figure 3.10 Time series of observed (blue) and simulated (red) 1-hr O_3 and NO_y daily maxima at Aldino, MD AQS site for July 6-13, 2007 (LST). Ozone reached a maximum of 139 ppbv for a full hour.

On the Aldino NO_y monitor the converter is located near the instrument inlet, so this represents a true NO_y measurement, without loss of HNO_3 as is typical of commercial compliance NO_x analyzers [e.g. *Poulida et al.*, 1994; *Schwab et al.*, 2009].

Observed and modeled O_3 mixing ratios showed an increasing trend in the daily maximum value from July 6 through July 9. On July 9, the observed O_3 concentration reaches a maximum of 139 ppbv around 2 pm LST, the model underpredicts this peak by 30 ppbv. The short-lived spike of 139 ppbv may be the result of the Chesapeake Bay breeze - a small scale area of convergence formed along the northeast part of Washington, DC suburbs that is difficult to capture with the 12 km model resolution [*Loughner et al*., 2010]. Overall, WRF/Chem captures the general shape of the diurnal cycle of ozone with minima in the early morning and maxima in the afternoon, with a correlation coefficient (r) of 0.84 (Table 3.6a). Afternoon ozone maxima result from photochemical reactions of surface emitted CO, NO, and hydrocarbons [e.g., *Crutzen, 1979*]. Upper level transport of O_3 precursors from upwind emission sources and mixing into the planetary boundary layer also contributes to surface ozone maxima. At nighttime, photochemical production is suspended, and O_3 is lost by reaction with NO, VOC's and by dry deposition. Over the course of the smog event, WRF/Chem O_3 overestimates nighttime minima by 7.26 ppbv (NMB=21.9%) (Table 3.7a); daytime maxima are underpredicted during the peak ozone days of July 9-11. O_3 mean daytime bias is -5.97 ppbv (NMB = -10.0 %) and mean daytime RMSE is 14.3 ppbv (NME = 17.4 %) (Table 3.6a). The passage of a cold front seen in Figure 1f is evident in the decrease of observed and simulated O_3 at nighttime and early morning on July 12. O_3 amounts at Aldino were sensitive to O_3 dry deposition velocities. Sensitivity simulation where O_3 dry deposition velocity in the model was doubled (E_DRYDEP) reduced nighttime O_3 by 11.4 ppbv

a) Aldino	MB (ppbv)	NMB (%)	RMSE (ppbv)	NME (%)	r	std (ppbv)
O_3	-5.97	-10.0	14.3	17.4	0.84	13.1
NO_y	1.32	24.0	4.08	54.7	0.53	3.88
b) Pinnacle	**MB (ppbv)**	**NMB (%)**	**RMSE (ppbv)**	**NME (%)**	**r**	**std (ppbv)**
O_3	-7.33	-14.3	9.2	16.1	0.86	6.58
CO	12.0	8.42	24.2	14.6	0.3	23.4
NO_y	-0.15	-5.01	0.88	24.7	0.74	0.92
NO_x	0.03	3.44	0.71	52.5	0.12	0.78
NO_z	-0.16	-8.57	0.47	21.4	0.83	0.49
Temp	0.35	1.45	2.19	6.2	0.87	2.17
c) Smokies	**MB (ppbv)**	**NMB (%)**	**RMSE (ppbv)**	**NME (%)**	**r**	**std (ppbv)**
O_3	-6.82	-13.4	15.4	23.9	0.47	13.9
CO	-17.5	-10.7	54.4	25.4	-0.08	51.8
NO_x	-0.79	-36.3	1.32	49.2	0.44	1.07
Temp	2.25	10.0	3.61	13.6	0.36	2.83
d)SEARCH-JST	**MB (ppbv)**	**NMB (%)**	**RMSE (ppbv)**	**NME (%)**	**r**	**std (ppbv)**
O_3	0.89	2.7	16.0	37.4	0.52	16.1
CO	200.4	93.6	310.3	101.4	0.15	253.7
NO_y	9.67	68.8	19.0	91.0	0.31	16.6
NO_x	8.82	70.6	18.9	101.2	0.27	16.9
NO_z	0.63	36.0	1.65	78.4	0.48	1.55
Temp	1.48	5.56	4.14	12.0	0.18	3.89
e)SEARCH-YRK	**MB (ppbv)**	**NMB (%)**	**RMSE (ppbv)**	**NME (%)**	**r**	**std (ppbv)**
O_3	4.48	12.4	8.73	26.6	0.55	11.3
CO	7.17	5.04	39.9	20.8	0.36	41.0
NO_y	1.97	70.2	3.07	81.2	0.27	2.36
NO_x	1.21	62.6	2.34	89.8	0.3	2.01
NO_z	0.76	86.9	1.05	95.2	0.47	0.73
Temp	1.8	7.35	4.78	14.6	-0.01	4.46

Table 3.6 Discrete evaluation results for individual sites calculated for daytime hours (6 am – 8 pm LST).

a) Aldino	MB (ppbv)	NMB (%)	RMSE (ppbv)	NME (%)	r	std (ppbv)
O_3	7.26	21.9	15.4	39.0	0.52	13.8
NO_y	0.32	4.26	4.21	45.8	0.14	4.24
b) Pinnacle	**MB (ppbv)**	**NMB (%)**	**RMSE (ppbv)**	**NME (%)**	**r**	**std (ppbv)**
O_3	-8.44	-18.0	10.8	21.2	0.81	8.82
CO	3.39	2.25	29.2	16.2	-0.14	32.9
NO_y	-0.4	-13.2	0.7	23.4	0.15	0.74
NO_x	-0.57	-32.0	0.93	48.6	-0.45	0.89
NO_z	0.11	8.45	0.48	35.7	0.62	0.56
Temp	1.42	7.46	2.07	8.74	0.93	1.52
c) Smokies	**MB (ppbv)**	**NMB (%)**	**RMSE (ppbv)**	**NME (%)**	**r**	**std (ppbv)**
O_3	-9.35	-20.2	14.6	28.3	0.26	11.4
CO	-6.69	-4.57	38.5	18.71	0.31	38.2
NO_x	-0.22	-13.2	0.89	43.5	0.58	0.88
Temp	2.04	9.78	2.91	11.9	0.22	2.1
d)SEARCH-JST	**MB (ppbv)**	**NMB (%)**	**RMSE (ppbv)**	**NME (%)**	**r**	**std (ppbv)**
O_3	4.32	39.4	9.9	77.4	0.37	8.99
CO	161.0	58.0	214.6	63.5	0.23	149.5
NO_y	0.44	1.78	18.2	52.9	0.06	18.4
NO_x	-0.41	-1.68	17.9	54.2	0.04	18.1
NO_z	0.85	169.0	1.47	234.8	0.19	1.21
Temp	3.63	16.2	4.18	16.2	0.22	2.08
e)SEARCH-YRK	**MB (ppbv)**	**NMB (%)**	**RMSE (ppbv)**	**NME (%)**	**r**	**std (ppbv)**
O_3	4.46	16.4	6.51	29.8	0.31	8.21
CO	1.38	0.95	36.8	23.5	0.21	39.8
NO_y	0.44	11.3	1.99	42.6	0.26	1.98
NO_x	-0.16	-4.82	1.97	47.5	0.14	2.0
NO_z	0.59	111.1	0.8	127.5	0.22	0.55
Temp	2.46	11.8	3.37	11.9	0.12	2.33

Table 3.7 Discrete evaluation results for individual observation sites calculated for nighttime hours (8 pm – 6 am LST).

changing the NMB from 21.9 % to -12.1% (Table 3.8). Low dry deposition velocity in the standard model simulation contributes to insufficient nighttime depletion of O_3 at Aldino, MD.

a) Day	NMB O_3(%)			NMB NO_y(%)			NMB NO_x(%)		
	E_BASE	E_CHEM	E_DRYDEP	E_BASE	E_CHEM	E_DRYDEP	E_BASE	E_CHEM	E_DRYDEP
Aldino	-10.0	-7.05	-23.1	24.0	18.9	17.9	N/A	N/A	N/A
Pinnacles	-14.3	-9.89	-30.2	-5.01	3.12	-1.18	3.44	13.0	9.42
Smokies	-13.4	-7.61	-23.9	N/A	N/A	N/A	-36.3	-47.7	-48.7
JST	2.7	15.1	-0.98	68.8	75.8	75.3	70.6	74.8	74.9
YRK	12.4	31.0	10.6	70.2	67.7	65.3	62.6	54.8	54.0
b) Night	NMB O_3(%)			NMB NO_y(%)			NMB NO_x(%)		
	E_BASE	E_CHEM	E_DRYDEP	E_BASE	E_CHEM	E_DRYDEP	E_BASE	E_CHEM	E_DRYDEP
Aldino	21.9	25.2	-12.1	4.26	6.16	6.22	N/A	N/A	N/A
Pinnacles	-18.0	-16.3	-37.3	-13.2	-8.67	-10.8	-32.0	-17.9	-21.1
Smokies	-20.1	-15.0	-35.6	N/A	N/A	N/A	-13.2	-16.5	-15.4
JST	39.4	43.6	-10.0	1.78	4.26	4.51	-1.68	1.07	1.32
YRK	16.4	24.0	-7.74	11.3	13.8	14.8	-4.82	-2.06	-0.71

Table 3.8 WRF/Chem E_BASE , E_CHEM, and E_DRYDEP mean a) daytime and b) nighttime O_3, NO_y and NO_x biases for observation sites.

Total reactive nitrogen distributions are influenced by a combination of emission, photochemistry, and transport processes. Aldino station is located in a suburban area, but in close proximity to I-95 interstate (~ 2 km). CO and NO_x emissions for the 12 km grid containing Aldino, are significantly influenced by

interstate traffic. Observed NO_y reaches a maximum concentration in the early morning and secondary maximum in the afternoon (Figure 3.10b). Vehicle emissions of NO_x contribute to the peaks during morning rush hour, especially on weekdays (July 9-11, 2007). During the early afternoon, NO_y mixing ratios fall due to deepening of the planetary boundary layer (PBL), mixing, and loss by deposition. As the PBL height begins to decrease, NO_x mixing ratios increase in the late afternoon. WRF/Chem daytime NO_y normalized mean bias is 24.0 % and NME is 54.7 %. In the sensitivity simulation where NO_x conversion to nitric acid was suppressed (E_CHEM), model daytime O_3 and NO_y mean biases were reduced to -7.05 % and 18.9 %, respectively (Table 3.8). This suburban site is sensitive to perturbations in ozone deposition velocity and N_2O_5 aerosol accommodation coefficient.

3.5.3.2 Pinnacle State Park, NY

Observations of trace species and meteorological variables at Pinnacle State Park research site (elev. 504 m above sea level) are shown in Figure 3.11. At this remote site, trace gas measurements are available only for the beginning and end of the simulated period due to failure of air conditioning in the instrument shelter. Model O_3 tracks the diurnal variation seen in observations (r=0.86). The model underpredicts O_3 at this site, NMB and RMSE for O_3 are -14.3 % and 9.20 ppbv, the greatest negative bias in comparison with all sites (Table 3.6a). Similarly to the Aldino, MD site, the cold front marched through at nighttime on July 11-12 as seen in hourly O_3 and temperature measurements (Figure 3.11a,c).

CO is a good tracer for transport due to its long life time of approximately a month. Predicted daytime CO is generally in good agreement with the observations (NMB:8.42%, NME:14.6%) indicating that transport from upwind sources is sufficiently well represented by the model. The model has the drop in CO due to cold front passage a little early, but overpredicts slightly at other times. Basic diurnal cycles of air temperature (Figure 3.11c) are represented by the model with correlation coefficient r = 0.87. WRF/Chem air temperature is overpredicted by 1.42°C at night and underpredicted by 0.35°C during the day. NO_y, NO_x, and NO_z ($NO_y - NO_x$) measurements are below 8 ppbv (Figure 3.11d-f) characteristic of a rural location, with occasional perturbations by local sources. The model underestimates daytime NO_y by 5.01 % and overestimates NO_x by 3.44 % (Table 3.6b). Part of the modeled enhancement in NO_z and NO_y in the afternoon on July 10, is due to simulation of high HNO_3 in the air mass sampled in the model.

Daytime and nighttime normalized mean biases of O_3 and NO_y were reduced in the E_CHEM simulation (Table 3.8), which provides an upper limit on NO_x recycling at this site. Similar to the Aldino site, prediction of O_3 was improved by extending the lifetime of NO_x and its availability for O_3 formation.

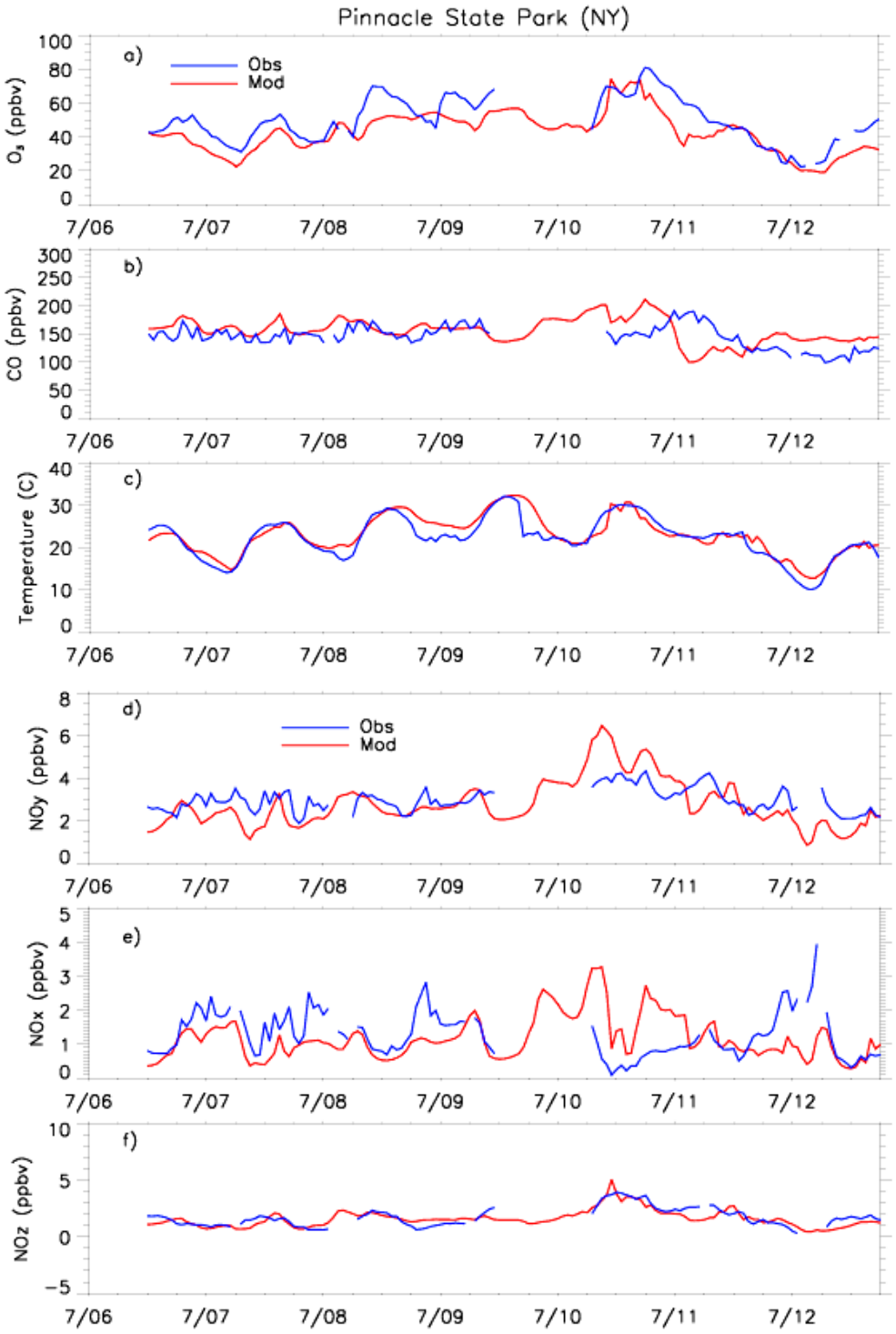

Figure 3.11 Time series of observed (blue) and simulated (red) 1-hr daily maxima at Pinnacle State Park, NY site for July 6-13, 2007 (LST). Missing data on July 9-10 due to failure of air conditioning in the instrument shelter.

3.5.3.3 Great Smoky Mountains, TN

Measurements of O_3, CO, NO_x and air temperature at Great Smoky Mountains site (elev. 793 m above sea level) are shown in Figure 3.12; the model is too clean and too cool. At this site the model does not exhibit observed diurnal variation of ozone, with poor daytime correlation (r = 0.47). Daytime ozone normalized mean bias and normalized error are -13.4 % and 23.9 %, respectively (Table 3.6a). Observed CO amounts and diurnal variations are underestimated substantially by the model. Similar to the Pinnacle site, at this mountain site, the 12 km nested WRF/Chem simulation is not expected to capture the small scale processes associated with orography. On average, the model overpredicts daytime and nighttime air temperature by 2.25°C and 2.04°C, respectively.

WRF/Chem RADM2 chemical mechanism used in this simulation underestimates NO_x at this site, with NMB of -36.3 % and NME of 49.2 %. WRF/Chem shows simultaneous low bias in NO_x mixing ratios and low bias in surface O_3. The results are sensitive to the rate at which N_2O_5 is converted to HNO_3. In E_CHEM sensitivity simulation where the N_2O_5 conversion to HNO_3 was set to zero, daytime O_3 mean bias was reduced from -13.4 % to -7.61 % while mean NO_x low bias increased from 36.3% to 47.7 % (Table 3.8). As at Aldino and Pinnacles sites, increased NO_x recycling reduced the magnitude of daytime and nighttime O_3 biases.

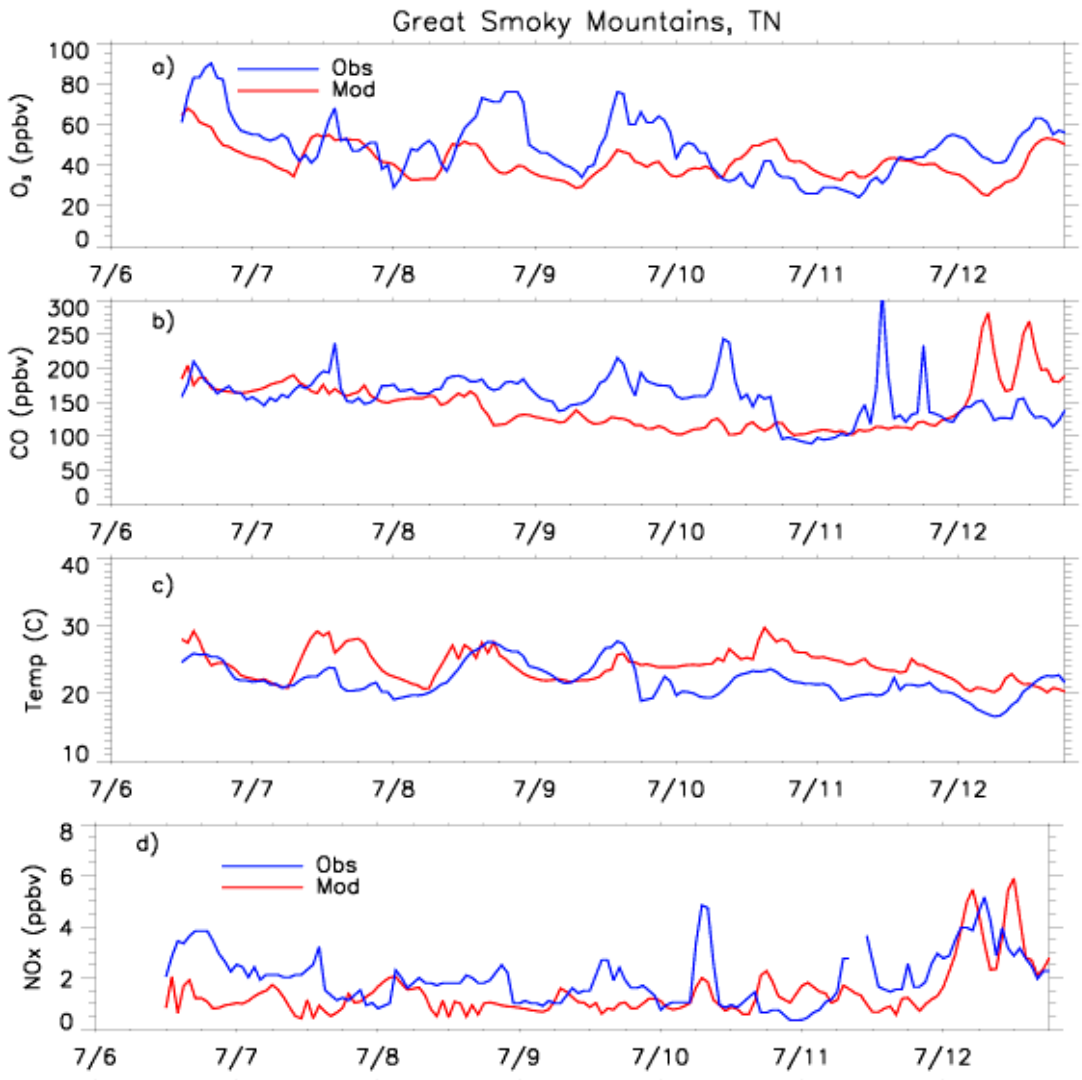

Figure 3.12 Time series of observed (blue) and simulated (red) 1-hr daily maxima at Great Smoky Mountains, TN site for July 6-13, 2007 (LST).

3.5.3.4 SEARCH sites, GA

Figure 3.13 compares observed and modeled trace gas species and meteorological variables at an urban SEARCH Jefferson St site (JST) in Atlanta, GA. Overlaid error bars are 1σ uncertainty in observations of O_3, CO, temperature and NO_y. Observations and the model exhibit the daytime peaks and nighttime troughs associated with ozone production during the day and destruction at night.

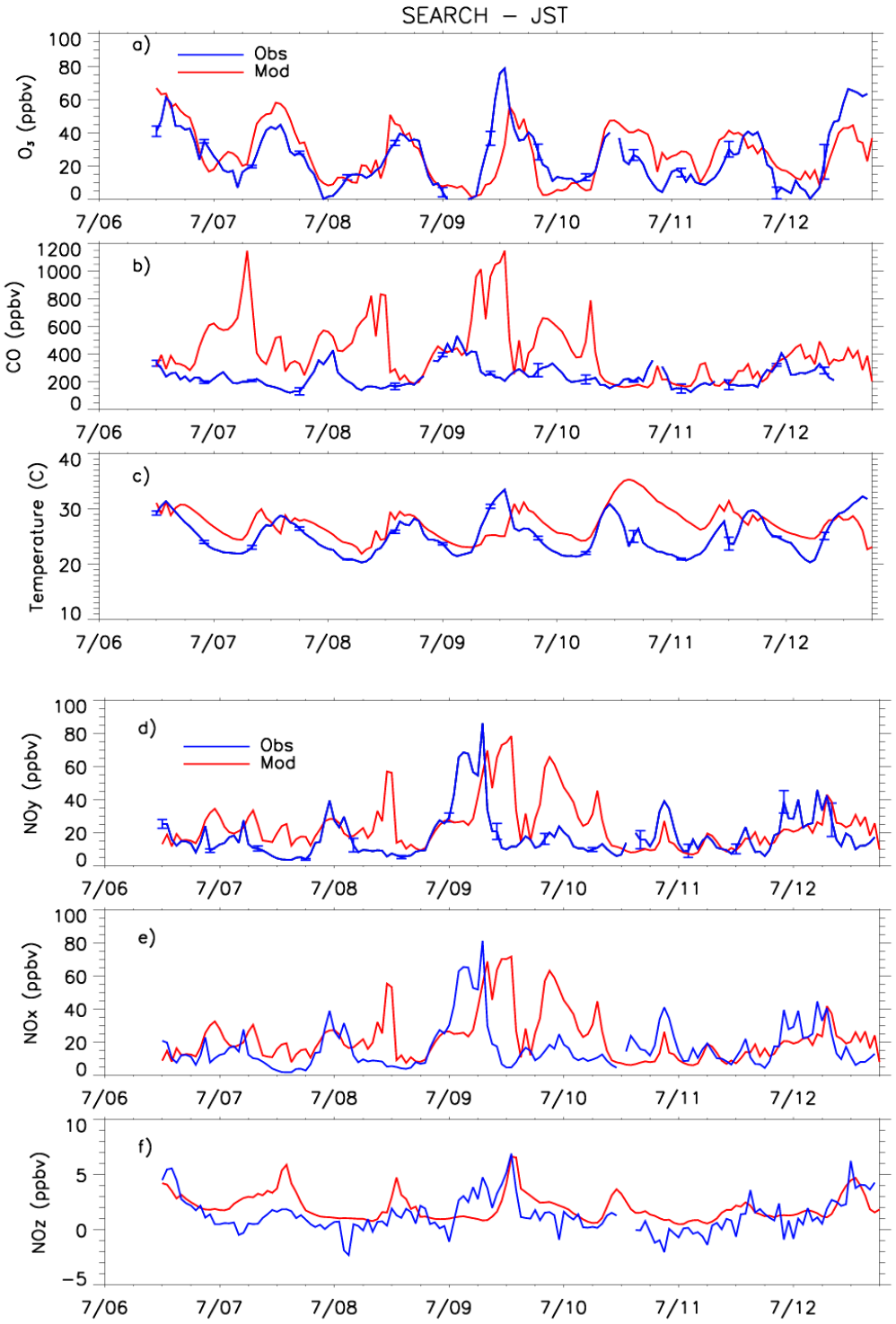

Figure 3.13 Time series of observed (blue) and simulated (red) 1-hr daily maxima at SEARCH – JST, GA site for July 6-13, 2007 (LST). Error bars for O_3, CO, temperature, and NO_y represent 1σ uncertainty in measurements, shown for every 8th hour.

Daytime CO normalized mean bias at this site is 93.6 % and correlation coefficient (r) is 0.15 (Table 3.6). Observed CO mixing ratios (< 400 ppbv) are lower than what is typically observed in an urban region such as downtown Atlanta, GA (600- 800 ppbv) [*Blanchard and Tanenbaum*, 2006]. Observed CO to NO_x ratios are also much lower than EPA published guidelines (10:1 ratio) for an area where a combination of gasoline and diesel fueled vehicles is present (available at http://www.epa.gov/ttn/chief/trends/). These inconsistencies could indicate a problem with the CO measurements. Alternatively, the poor agreement with observations could indicate that CO motor vehicle emissions (MOBILE6) used in this study are overestimated. *Parrish* [2006] showed that CO emissions from motor vehicles in MOBILE6 are overestimated by a factor of 2 in comparison with a fuel-based inventory. Moreover, *Kuhns et al.* [2004] compared MOBILE6 CO emission factors to those measured by vehicle exhaust remote sensing; MOBILE6 CO emission factors were 2 times greater than measured CO emission factors for vehicles less than 13 years old. According to the EPA 2002 national inventory within Fulton County (metropolitan Atlanta), on-highway and off highway motor vehicles accounted for 98% of CO emissions and 87% of NO_x emissions [available at http://www.epa.gov/air/data]. By contrast, in northeastern U.S. on-highway and off highway motor vehicles account for 91 % of CO emissions and 58 % of NO_x emissions; stationary sources (i.e. electric power plants and industrial factories) account for the remaining 42 % of emitted NO_x, Therefore, higher accuracy in model representation of CO and NO_x emissions from mobile sources is needed in the Southeast U.S region.

The model does a reasonable job with daytime ozone maxima, but underestimates peak O_3 on July 9. WRF/Chem daytime ozone mean bias is 0.89 ppbv (NMB of 2.70 %) and RMSE of 16.0 ppbv (NME of 37.4 %), while correlation coefficient is moderate (r = 0.52). Nighttime O_3 mixing ratios below 10 ppbv were observed during most of the comparison period. Single digit O_3 mixing ratios at nighttime are attributed to nighttime depletion of surface O_3 by dry deposition and in situ chemistry with limited re-supply of O_3 – rich air from aloft [*Talbot et al.* 2005]. Nighttime ozone destruction in the model is not as efficient; biases in O_3 dry deposition velocity are a possible explanation. In E_DRYDEP simulation daytime (nighttime) O_3 normalized mean bias was reduced from 2.7 (39.4) % to -0.98 (-10.0) %.

Figure 3.13d and Figure 3.13f compare observed and simulated NO_y, NO_x and NO_z species at JST. WRF/Chem overpredicts daytime NO_y, NO_x and NO_z peaks with normalized mean biases of 68.8 %, 70.6 % and 36.0%, respectively. The modeled peak of NO_y and NO_x on July 9 appears to be predicted but with a 6 hour time lag. Modeled O_3 also lags and does not reach the observed 80 ppbv peak. Observed convective storm over Atlanta, GA at approximately 1 pm local time mixes polluted boundary layer air with cleaner upper level air (Figure 3.3). The timing of the modeled convective storm is about 2 hours late. The storm's strong updrafts lifted polluted surface air into the upper troposphere and downdrafts mixed clean upper-level air through the PBL.

Figure 3.14 compares measurements and simulation results at a rural SEARCH Yorkville, GA site. Overlaid error bars are 1σ uncertainty in observations

of O_3, CO, temperature and NO_y. Available ozone measurements during July 9-12, 2007 period show model daytime and nighttime overestimation with NMB of 12.4% and 16.4%, respectively. This may result from excess import of O_3 or the nighttime mean bias in temperature of 2.5°C. At YRK, CO has no significant diurnal pattern, indicative of the rural nature of this site distant from mobile source emissions. NO_y, NO_x and NO_z daytime normalized mean bias is 70.2 %, 62.6 % and 86.9 %, respectively. Biases between model and observations exceed observation uncertainty. Similarly to JST site, increased O_3 dry deposition at this site improves both daytime and modeled performance (Table 3.8). E_CHEM sensitivity simulation decreased biases in daytime and nighttime NO_x at YRK site, but this contributed to significant overproduction of O_3.

In summary, WRF/Chem captures the diurnal variability of O_3 and NO_y species at Aldino, Pinnacles, Great Smokies and SEARCH sites over the course of the smog episode, terminated by the timely passage of the cold front in the model. Sensitivity simulations tweaking O_3 dry deposition and N_2O_5 accommodation coefficient slightly improved model performance at most of the sites. Accelerated O_3 dry deposition improved nighttime O_3 at Aldino and SEARCH sites. Maximum recycling of NO_x through $ClNO_2$ chemistry improved model performance in the Northeast, especially the remote Pinnacles site, but increased model bias in the Southeast. Model NO_x biases decreased at Pinnacles, JST and YRK sites during the night time and during daytime at the YRK site. Poor model performance in the Southeast can be explained by high temperature bias (>1.5°C) with respect to observations. In WRF/Chem the isoprene emissions by the forests directly depend on

temperature [*Grell et al.*, 2005]. Overpredicted temperatures result in more isoprene emissions, faster reaction rates and overpredicted O_3 fields. In general, the model is much more sensitive to changes in temperature and increased insolation than chemistry. FDDA sensitivity run increased already high temperature bias at Southeast U.S. sites, increasing O_3 MB in Southeast U.S. by 12 ppbv. Where the model succeeds at predicting temperature and NO_x concentrations the calculated O_3 fields agree best with observations. There remains much more to learn about the causes of biases between modeled and measured ozone in the Southeast U.S.

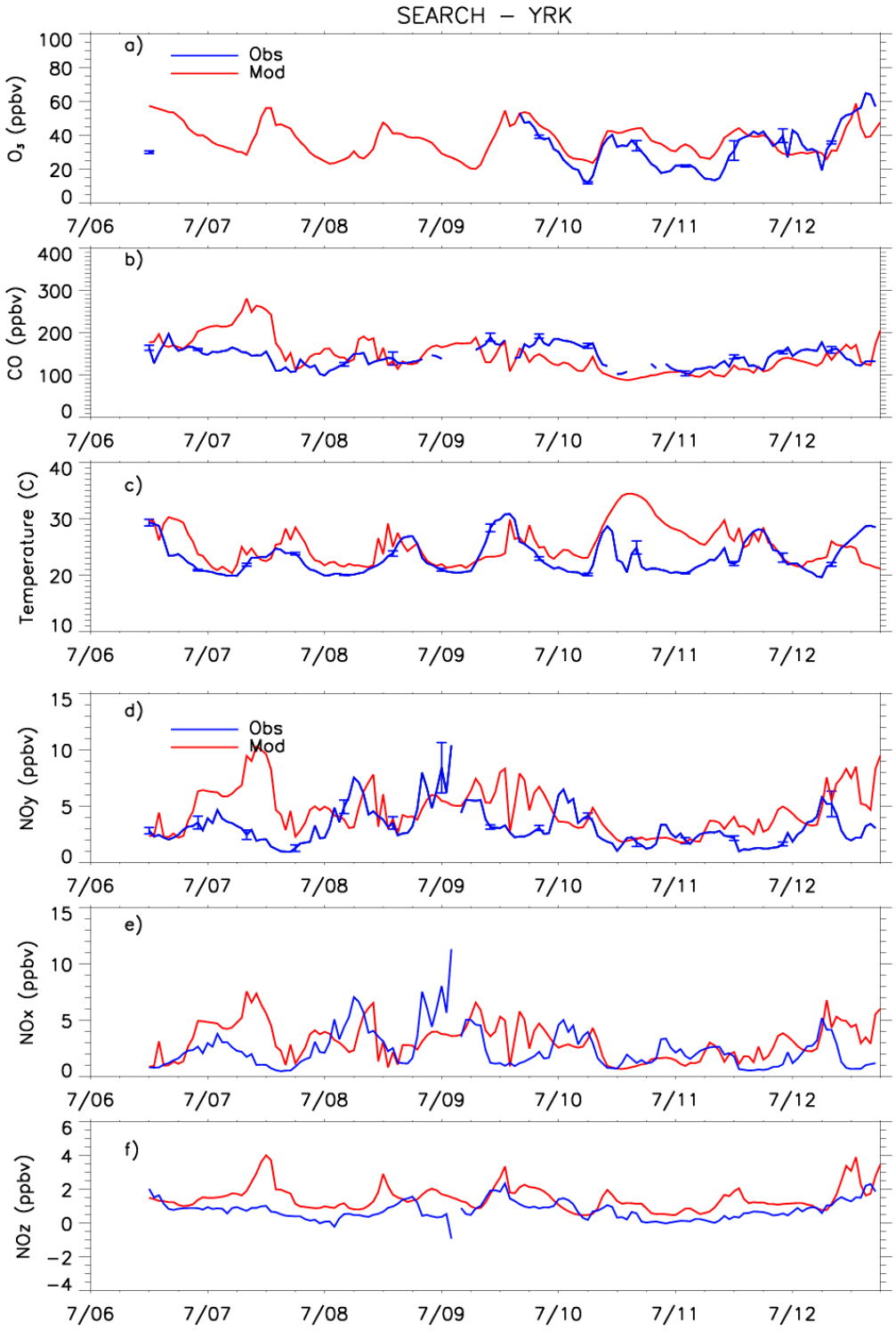

Figure 3.14 Time series of observed (blue) and simulated (red) 1-hr O_3 daily maxima at SEARCH – YRK, GA site for July 6-13, 2007 (LST). Error bars represent 1σ uncertainty in measurements.

3.5.4 WRF/Chem Vertical Analysis

Figure 3.15 shows WRF/Chem simulated O_3 on 6 layers: surface, 950 hPa, 910 hPa, 815 hPa, 730 hPa, and 685 hPa for 18 UTC July 9, 2007. The signature of the smog event in northeast U.S. is most visible from the surface to 730 hPa. Pollutant outflow into the Atlantic from densely populated metropolitan areas along I-95 corridor is greatest in the 950 hPa and 910 hPa layers. Enhanced ozone at 730 hPa and up is associated with upper level regional transport of ozone and its precursors driven by midlatitude cyclonic wind patterns.

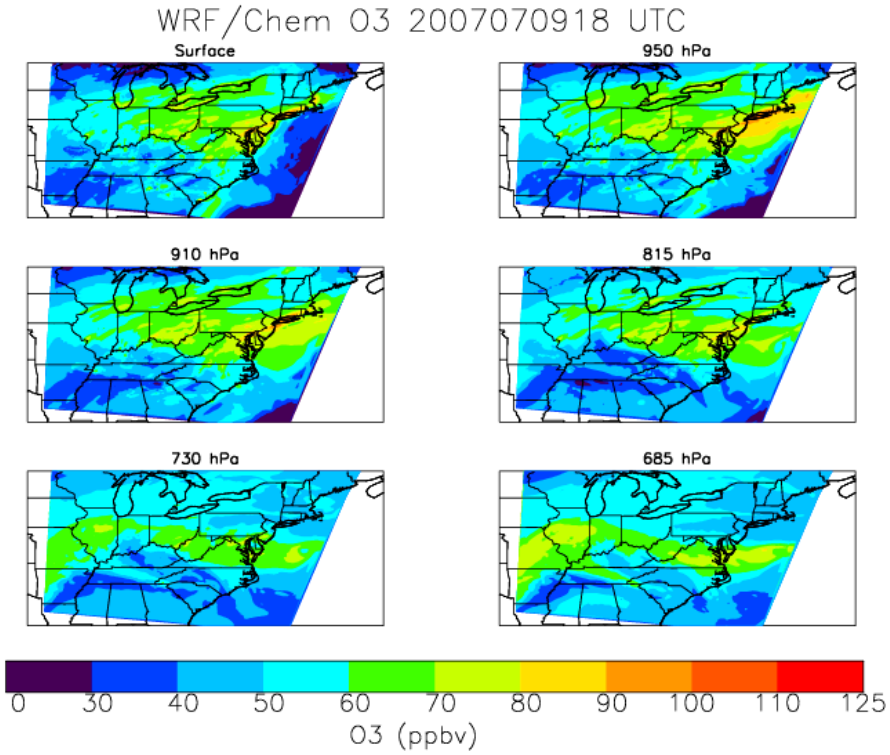

Figure 3.15 WRF/Chem O_3 on surface, 950 hPa, 910 hPa, 815 hPa, 730 hPa and 685 hPa for 18 UTC July 9, 2007.

Several ozonesondes were launched during the July 6-11, 2007 ozone episode at Beltsville, MD (76.5°W, 39.0°N) [*Yorks et al.*, 2009]. Ozonesonde launches took place in a wooded area 19 km northeast of Washington, DC, under the auspices of

Howard University and NASA's Goddard Space Flight Center. Profiles from WRF/Chem experiments are compared to afternoon and nighttime ozonesonde profiles (Figure 3.16).

On July 9 at 18 UTC, a 100-113 ppbv layer of ozone is observed from surface to 800 hPa (Figure 3.16a). WRF/Chem matches the shape of the ozonesonde profile up to 650 hPa, but the magnitude is low by 13-25 ppbv below 800 hPa, as was seen in comparison to surface observations (Figure 3.4d, Figure 3.5d). MOZART-4 overestimates ozone between 550 – 300 hPa, and WRF/Chem overestimates ozone between 600 – 250 hPa by as much as 28 ppbv.

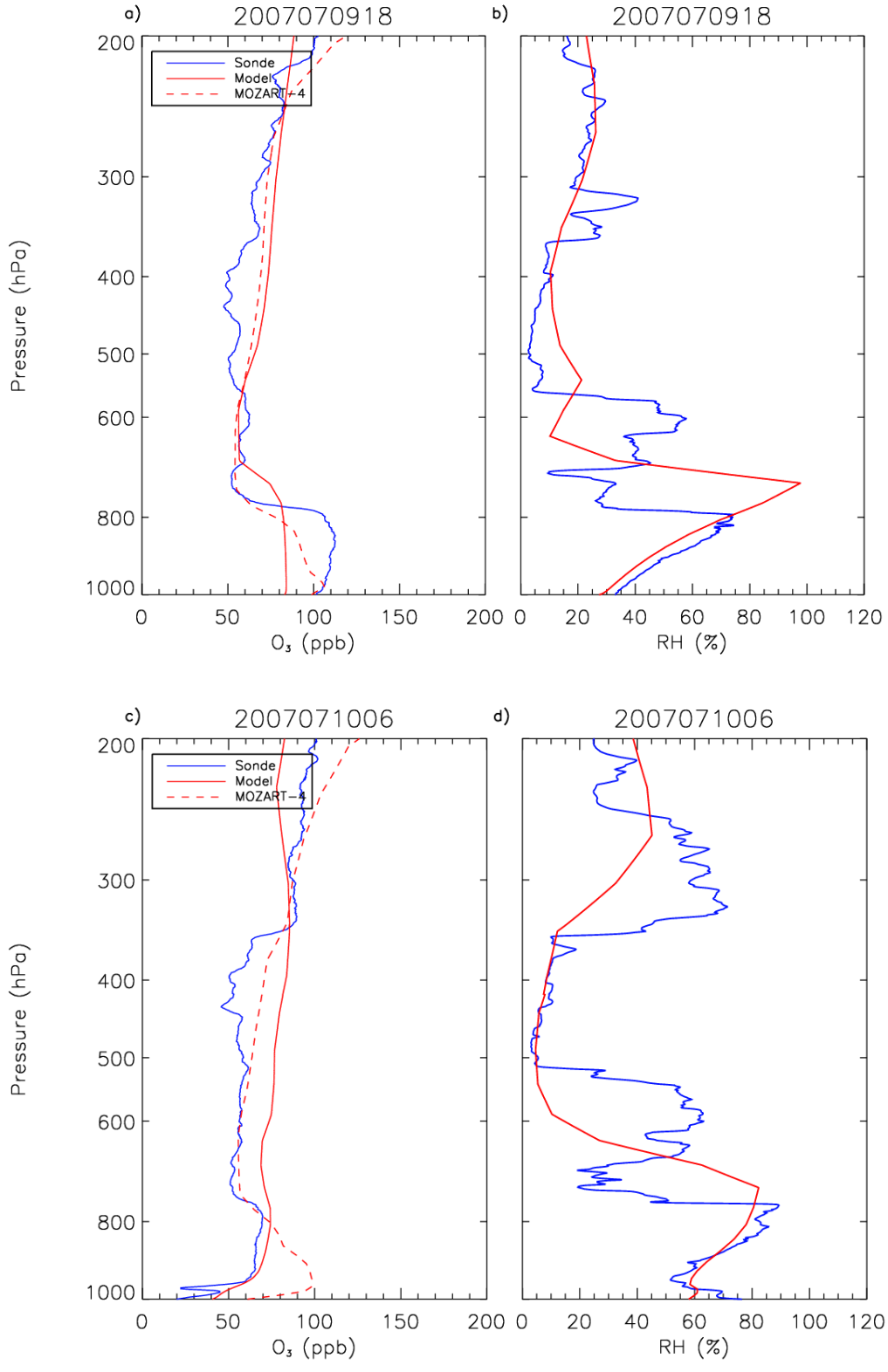
a)
2007070918
b)
2007070918
Sonde
Model
MOZART-4
Pressure (hPa)
200
300
400
500
600
800
1000
0
50
100
150
200
O_3 (ppb)
0
20
40
60
80
100
120
RH (%)
c)
2007071006
d)
2007071006
Sonde
Model
MOZART-4
Pressure (hPa)
O_3 (ppb)
RH (%)

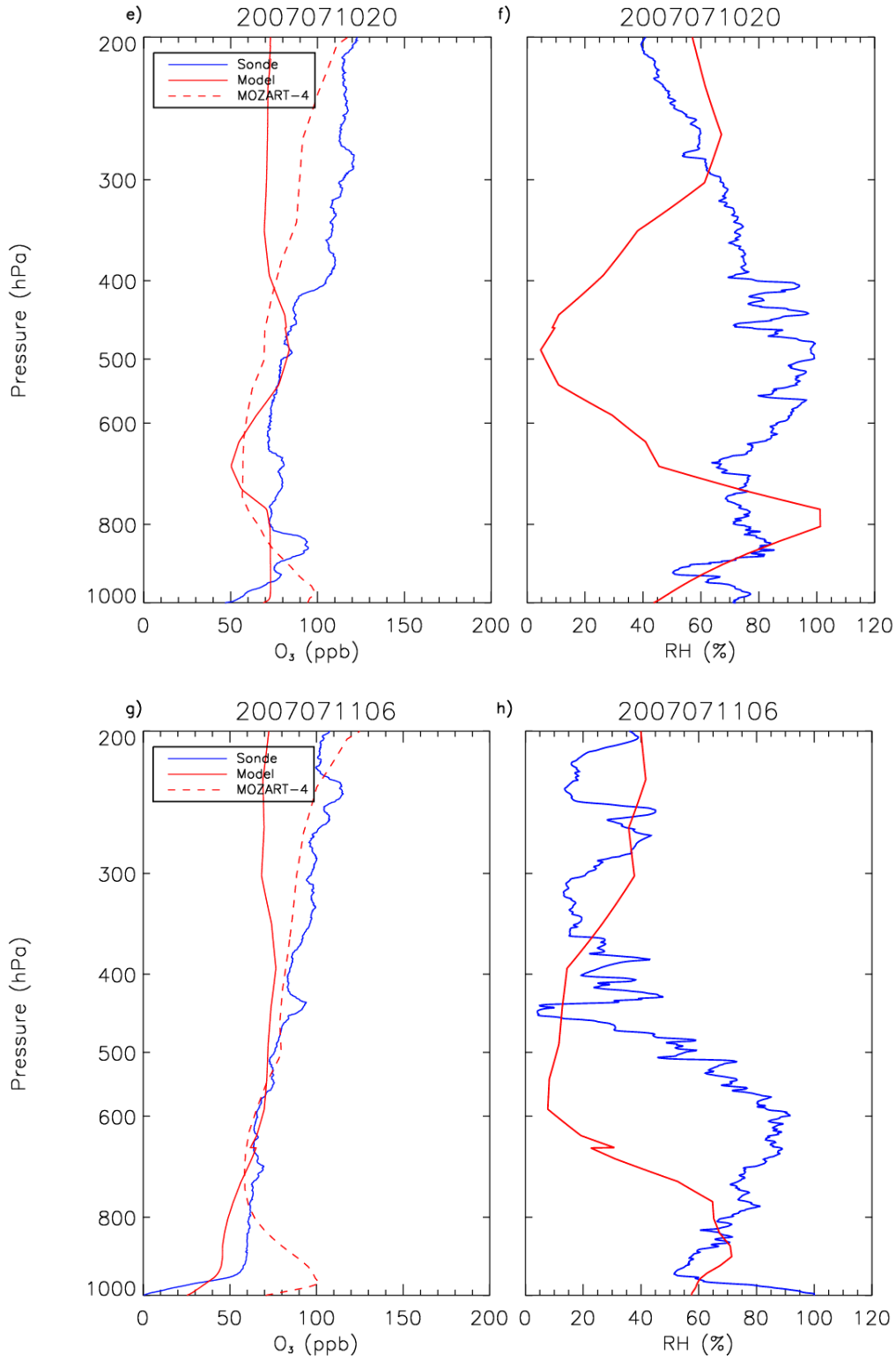

Figure 3.16 Simulated and observed ozone and relative humidity on July 9, 2007 18 UTC (a,b), July 10, 2007, 6 UTC (c,d), July 10, 2007, 20 UTC (e,f), and July 11, 2007, 6 UTC (g,h) at Beltsville, MD. MOZART-4 O_3 is also overlaid in dashed red lines.

The O_3 bias increased by more than 90% above 450 hPa when default chemical boundary and initial conditions were replaced by MOZART-4 fields. More than 90 % of the model bias above 450 hPa is due to MOZART-4 O_3 contribution. These findings agree with previous work by *Yu et al.* [2007], who reported overestimation of O_3 above 6 km due to lateral boundary conditions specification and coarse vertical resolution in the model.

Observed and predicted relative humidity increase with altitude from 30 % at the surface to 70 % at 800 hPa (Figure 3.16b). The model relative humidity continues to increase from 800 hPa to 750 hPa reaching 100% at 750 hPa before sharply decreasing to 20 % at 610 hPa. This suggests that the model mixing height is overpredicted by approximately 50 hPa (or 500 m). In the mid to upper troposphere, observed and modeled relative humidity is on average below 30 %, suggesting subsidence and an upper tropospheric origin (Figure 3.16b).

Another sounding was launched 12 hours later at 6 UTC on July 10th (Figure 3.16c). In this ozone sounding there is a local minimum at about 960 hPa. The vertical scale of this inversion is too small to be resolved by the model simulation. MOZART-4 ozone remains very high - peaking at about 100 ppbv at 950 hPa. Observed and modeled ozone mixing ratios in the boundary layer drop below 45 ppbv as ozone is removed by dry deposition and chemical titration. At nighttime, observed ozone in the 960 hPa to 800 hPa layer decreased to 65 ppbv, although above 800 hPa the profile is similar to the 18 UTC sounding up to 350 hPa. The model overpredicts nighttime PBL and mid-tropospheric ozone by 10-20 ppbv, with highest biases at 400 hPa. Observed and modeled relative humidity is enhanced around 800

hPa and 280 hPa. The model does not capture the peak in relative humidity seen at 600 hPa or the minimum between 700 and 800 hPa. In comparison with daytime observations, both the model and observations (Figure 3.16d) show enhanced relative humidity (65-75%) in the 340 hPa to 270 hPa levels; modeled and observed O_3 are enhanced 15 and 25 ppbv, respectively. Ozone production halts at night within the PBL, regional advective redistribution of ozone enhances mixing ratios at upper levels (above 350 hPa), while accumulated ozone in the mid troposphere (600-350 hPa) is greater than on previous day. Overall, model measurement agreement for ozone is good given the resolution of the model.

In the afternoon sounding on July 10, 20 UTC (Figure 3.16e), surface ozone is just 50 ppbv increasing with altitude to 95 ppbv at 830 hPa. Above the planetary boundary layer, ozone increases with height reaching 110-120 ppbv in the 400 hPa – 280 hPa layer. This profile is a good example of redistribution of trace species following a convective thunderstorm and transport from upwind sources accompanied by photochemical ozone production [*Dickerson et al.,* 1987*; Pickering et al.,* 1992]. On July 9, 2007 at 18 UTC there was significant thunderstorm activity across Alabama and Mississippi according to the NCDC radar reflectivity archive. GOES-12 IR infrared shows the spatial extent of this storm (Figure 3.3). HYSPLIT [*Draxler and Rolph*, 2003] back trajectory started on July 10, 20 UTC at 400 hPa at Beltsville, MD confirm passage of the sampled air mass through convective storms. Figure 3.17 shows MODIS cloud top pressure during the July 9, 18 UTC storm and the flow of HYSPLIT back trajectory though the storm at approximately 400 hPa. Ozone and its

precursors are lifted from the PBL into the upper troposphere by the storm's strong updrafts, while clean air is brought down by downdrafts.

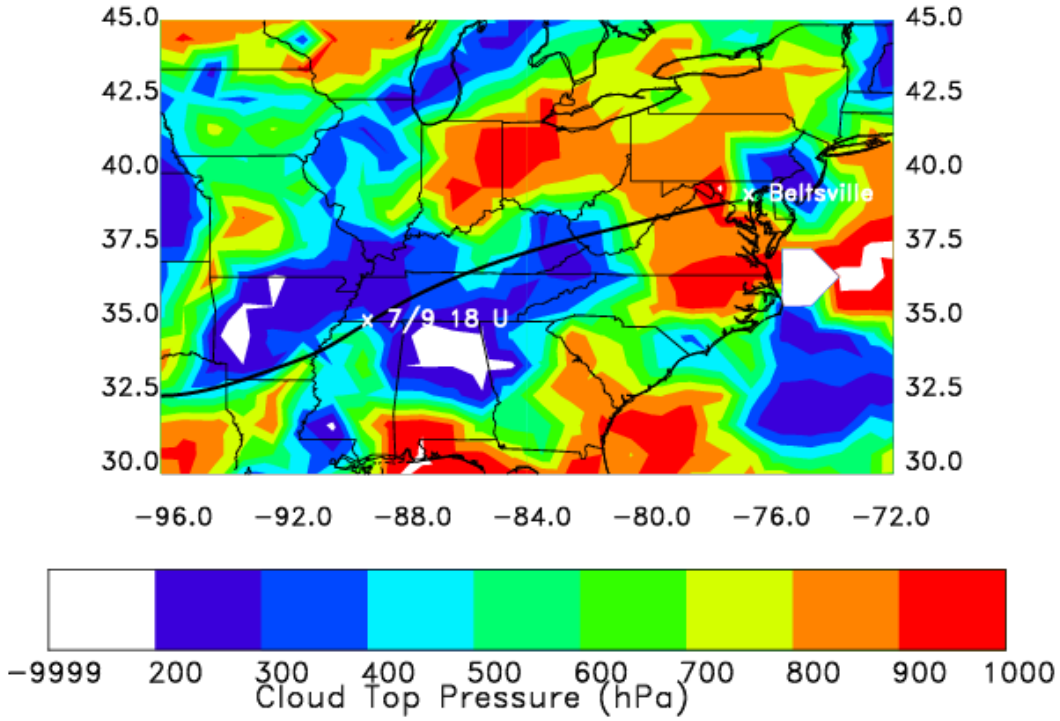

Figure 3.17 HYSPLIT back trajectories started at July 10, 20 UTC at 400 hPa from Beltsville, MD. MODIS cloud top pressure on July 9, 18 UTC is overlaid to show flow of back trajectories through convection in Alabama and Mississippi.

MOZART-4 chemical initial and boundary conditions improve upper level forecast on this day. In the PBL, the model O_3 profile is well-mixed and relative humidity is sharply increasing with height from 40 %. Here sub-grid convective processes are not being resolved in the model with the coarse 12 km resolution.

Yorks et al. [2009] analyzed budgets of free tropospheric ozone for the Beltsville, MD ozone profiles using a laminar identification method (LID) [*Thompson et al., 2007a, 2007b, 2008*] accounting for three processes: stratosphere to troposphere transfer (ST); regional convective redistribution of ozone and/or precursors, with photochemical reactions from lightning-produced NO (RCL); and

advection, including recent transport and aged ozone (AD). On July 9th RCL, ST, and AD accounted for 12.6 %, 14.2 %, and 73 % of the free tropospheric ozone column, respectively (Table 3.9). July 10th and 11th profiles were not influenced by stratospheric intrusion. For early morning July 10th sounding, advection term increases to 89.4% and RCL contribution is 10.6 %.

Date	Time	Trop Hgt (km)	PBL Hgt (km)	RCL (%)	ST (%)	AD (%)	FT O_3 (DU)
July 9	18 UTC	12.9	1.87	12.6	14.2	73.2	33.7
July 10	6 UTC	13.6	1.44	10.6	0.00	89.4	49.8
July 10	20 UTC	12.6	1.80	23.3	0.00	76.7	33.5
July 11	6 UTC	13.6	1.55	41.8	0.00	58.2	43.4
2007 AVG		12.8	1.60	15.3	32.1	52.6	40.6

Table 3.9 Budgets of free tropospheric O_3 for Beltsville, MD soundings, adapted from *Yorks et al.* [2009].

On July 10, 2007 at 17 UTC there was significant thunderstorm activity stretching from Ohio River Valley to Washington, DC area including Beltsville, MD according to the NCDC radar reflectivity archive. During the afternoon July 10th sounding, the advective source of O_3 decreases to 76.7%, and convection contribution increases to 23.3%. Early morning July 11th ozonesonde measurements following regional convective activity show that advection accounts for just 58.2 % of the total column, and regional convective distribution increases to 41.8 %, in agreement with WRF/Chem results. The mean percentage of RCL, ST, and AD contributions for 2007 profiles were 15.3 %, 32.1 %, and 52.6 % [*Yorks et al. 2009*]. July 11 early morning ozonesonde shows significant contribution of regional convective term – resulting from convective thunderstorm activity on July 10.

During the early morning sounding on July 11 (Figure 3.16g), nighttime PBL O_3 is overpredicted by 35 ppbv at the surface. MOZART-4 boundary layer ozone peaks at about 100 ppbv at 950 hPa. The WRF/Chem model is not fully capturing high humidity at the surface (~100 %) and ozone depletion through titration and deposition. This may be related to model turbulent mixing being too fast as shown by *Castellanos et al.* [2010].

A low level jet was present east of the Appalachian Mountains in the afternoon and night time hours of July 10 as well as the afternoon of July 11 (Figure 3.1d, Figure 3.1e). This LLJ formed in the warm sector of a midlatitude cyclone caused by large temperature gradients spanning from behind the cold front to the warm sector. At nighttime the LLJ is strengthened by cooling of high elevation air in the Appalachian Mountains relative to air at the same geopotential height along the east coast. The model shows increased O_3 layer of 70-75 ppbv at 850 hPa at midnight.

The model underpredicts upper tropospheric ozone above 400 hPa by 20-40 ppbv and does not capture observed relative humidity variability. Better relative humidity predictions were obtained for all soundings, when FDDA analysis and surface nudging techniques were used in a separate simulation to nudge water vapor, temperature and winds to NARR analysis and rawinsonde observations. However, FDDA nudging increased surface ozone biases by 25-30 ppbv across the southeast U.S. and mid-tropospheric biases at the location of Beltsville ozonesonde observations. Further sensitivity studies need to be performed to determine the

impact of FDDA nudging coefficients for temperature, wind, and water vapor on chemical processes in the model.

3.5.5 WRF/Chem Nudging Sensitivity Runs

I evaluated the impact of nudging the WRF runs with FDDA to see if it improves the simulation of weather and has an impact on computed O_3 fields. Differences in simulated O_3 mixing ratios in E_BASE and E_FDDA runs depend on representation of meteorological fields in the model. Figure 3.18 shows 6-hr accumulated precipitation, surface pressure and winds for E_BASE (or E030) and E_FDDA (or E028) experiments and hourly, multi-sensor National Precipitation Analysis (NCEP) Stage II 6-hr accumulated precipitation for July 9, 18 UTC. Nudging surface winds (u and v) and upper level u,v, T and q in the E_FDDA simulation produces substantial differences in surface pressure fields around the surface High over Virginia and West Virginia (~ 41°N, 80°W). E_BASE surface pressure fields are in better agreement with analyzed NOAA surface pressure fields (as was shown in Figure 3.1c) Also the location and intensity of convective storms south of 38°N is very different in the E_BASE and E_FDDA runs. E_BASE compares better with NCEP accumulated precipitation fields (Figure 3.18c). E_BASE captures the squall line passing over Lake Michigan, convective storm off the coast of North Carolina and storms stretching from Alabama to Georgia.

Differences in storm locations in E_FDDA lead to hotter surface temperatures in parts of South Carolina and Georgia (Figure 3.19) and lower soil moisture fields (Figure 3.21) in comparison with North American Regional Reanalysis used for model initialization and nudging. Table 3.10 compares temperature mean biases at

JST (Atlanta,GA) and YRK (Yorkville, GA) SEARCH sites for E_BASE and E_FDDA simulations. E_FDDA simulation has a higher daytime temperature mean bias by 0.46 °C-0.69°C with respect to E_BASE. In general in the southeast U.S., FDDA does not capture the spatial variability in convective storms, underpredicts soil moisture, overpredicts soil and 2 m temperature, leading to faster photochemistry than in the OBSGRID run.

a) WRF/Chem (E_BASE)

b) WRF/Chem (E_FDDA)

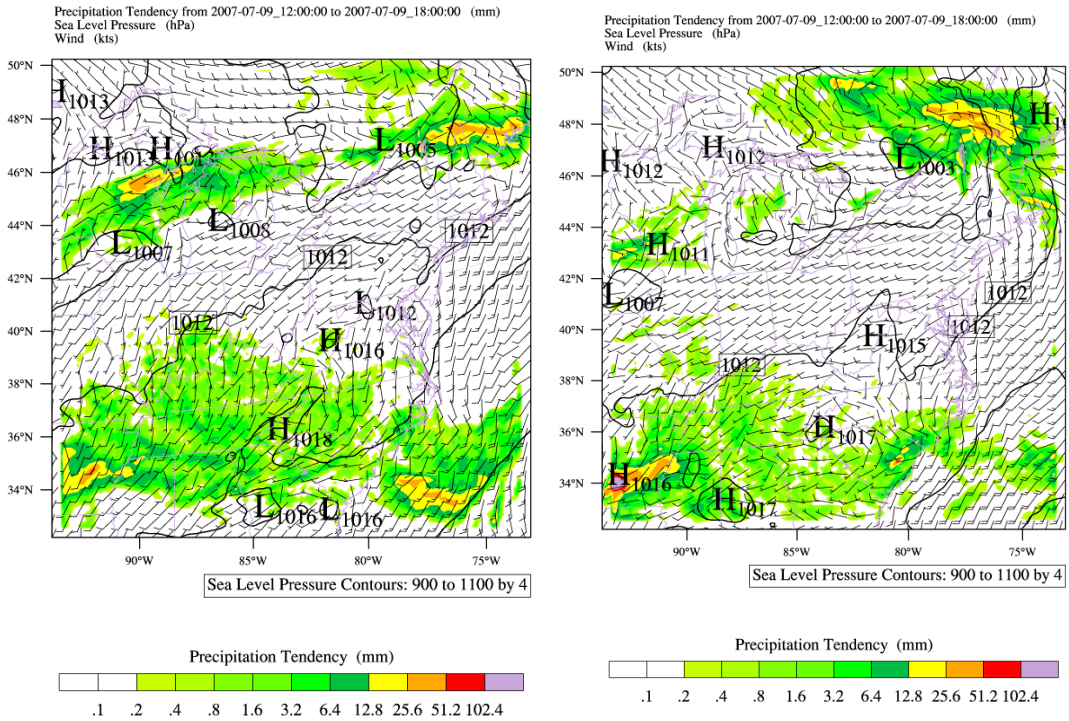

c) NCEP

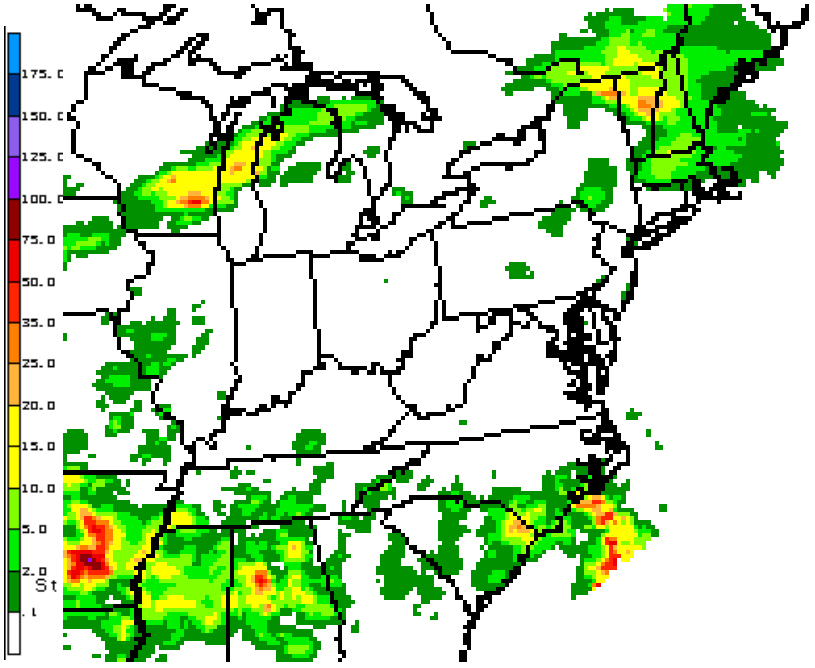

Figure 3.18 Accumulated 6 hr precipitation, surface pressure and surface wind barbs ending July 9, 18 UTC for a) E_BASE (or E030), b) E_FDDA (or E028), and c) NCEP Stage II Multi-sensor precipitation data.

a) WRF/Chem (E_BASE)

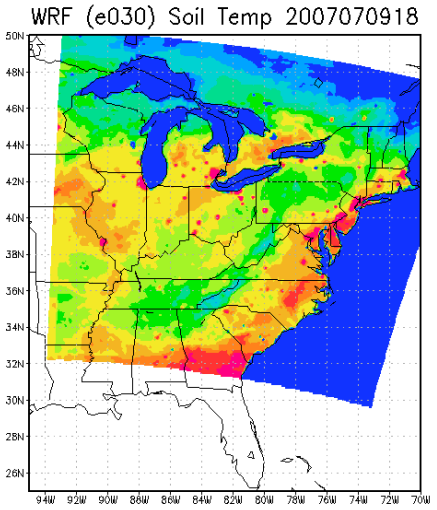

b) WRF/Chem (E_FDDA)

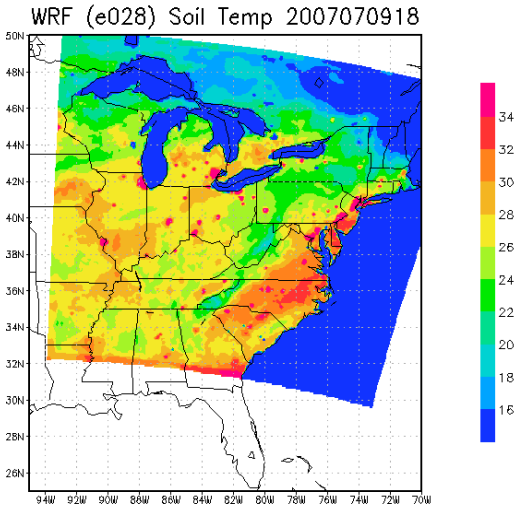

c) NARR

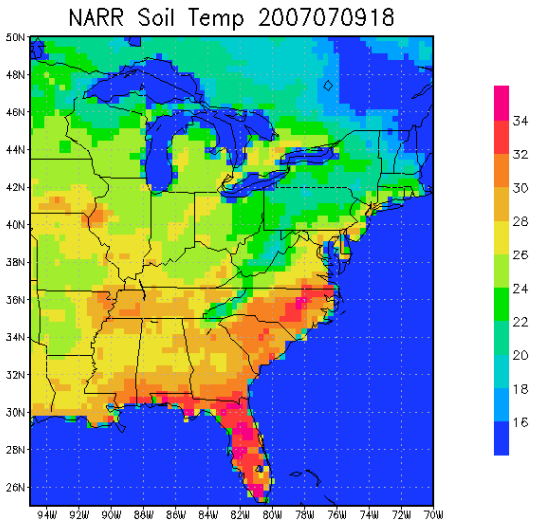

Figure 3.19 Soil Temperature on July 9, 2007 18 UTC for a) E_BASE (e030), b) E_FDDA (e028), and c) NARR.

a) WRF/Chem (E_BASE)

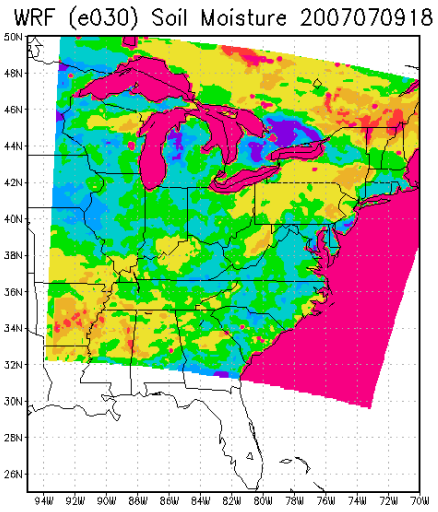

b) WRF/Chem (E_FDDA)

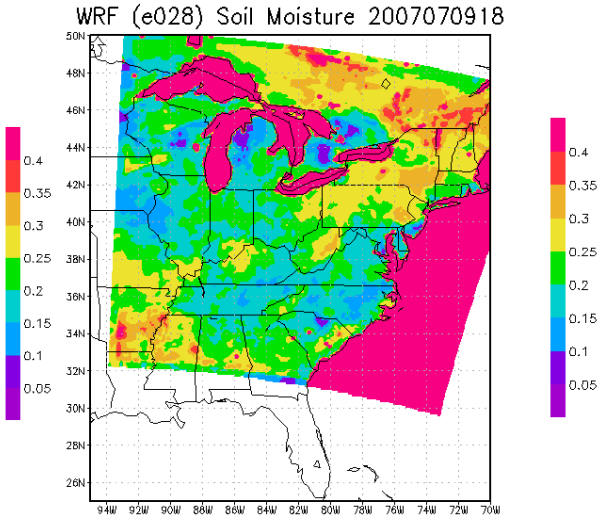

c) NARR

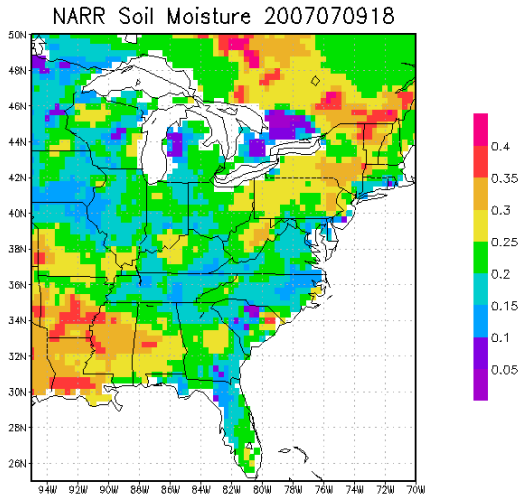

Figure 3.20 Soil moisture on July 9, 2007 18 UTC for a) E_BASE (e030), b) E_FDDA (e028), and c) NARR.

	Yorkville, GA (YRK)		Atlanta, GA (JST)	
	Day	Night	Day	Night
E_BASE	1.8	2.45	1.48	3.63
E_FDDA	2.26	2.45	2.17	3.87
Difference	0.46	0	0.69	0.24

Table 3.10 Daytime and nighttime temperature mean bias (°C) for E_BASE, E_FDDA at SEARCH YRK and JST sites. Also the difference between E_FDDA and E_BASE mean biases is shown.

I performed three additional sensitivity simulations to investigate the effect of nudging factors on WRF forecast of convective events in the model. I set nudging options for PBL and upper level dynamical nudging one at a time to single out the nudging coefficients that produce the largest errors in the meteorological simulation (Table 3.11). To preserve mesoscale model circulations, u and v nudging factors and T and q factors need to be set consistently (personal communication with Da-Lin Zhang).

	U,V Nudging		T, q nudging	
Experiment	PBL	Upper Level	PBL	Upper Level
E028	N	Y	N	Y
E030	N	N	N	N
E038	N	Y	N	Y
E039	N	N	N	Y
E040	N	Y	N	N

Table 3.11 Selected nudging coefficients for PBL and upper level FDDA nudging in WRF experiments E028,E030, E038 – E040. For E028 nudging was performed for outer 36 km domain only. For E038-E040 nudging was performed for 36 km and 12 km domains.

For the three additional sensitivity runs (E038, E039, E040) nudging in the PBL was turned off. Nudging of temperature in the PBL can cause static instability if it is inconsistent with temperature above the surface layer [*Stauffer et al.* 1991]. The

water vapor mixing ratio is not nudged in the PBL because supersaturation may occur when surface temperature is not nudged [*MDE,* 2010]. E038 included nudging effects of u and v winds, temperature and water vapor in the upper model levels. E039 simulation only included upper level T and q nudging, and E040 only included upper level u and v nudging. Figure 3.21 shows 6-hr accumulated precipitation, surface pressure and winds for E038, E039, and E040 experiments. Nudging upper level winds (E038 and E040) substantially changes surface isobar locations around the Washington-Baltimore metro area. The experiment with no u and v wind nudging (E039) produces surface pressure winds in closer agreement with E_BASE and NOAA surface pressure analysis.

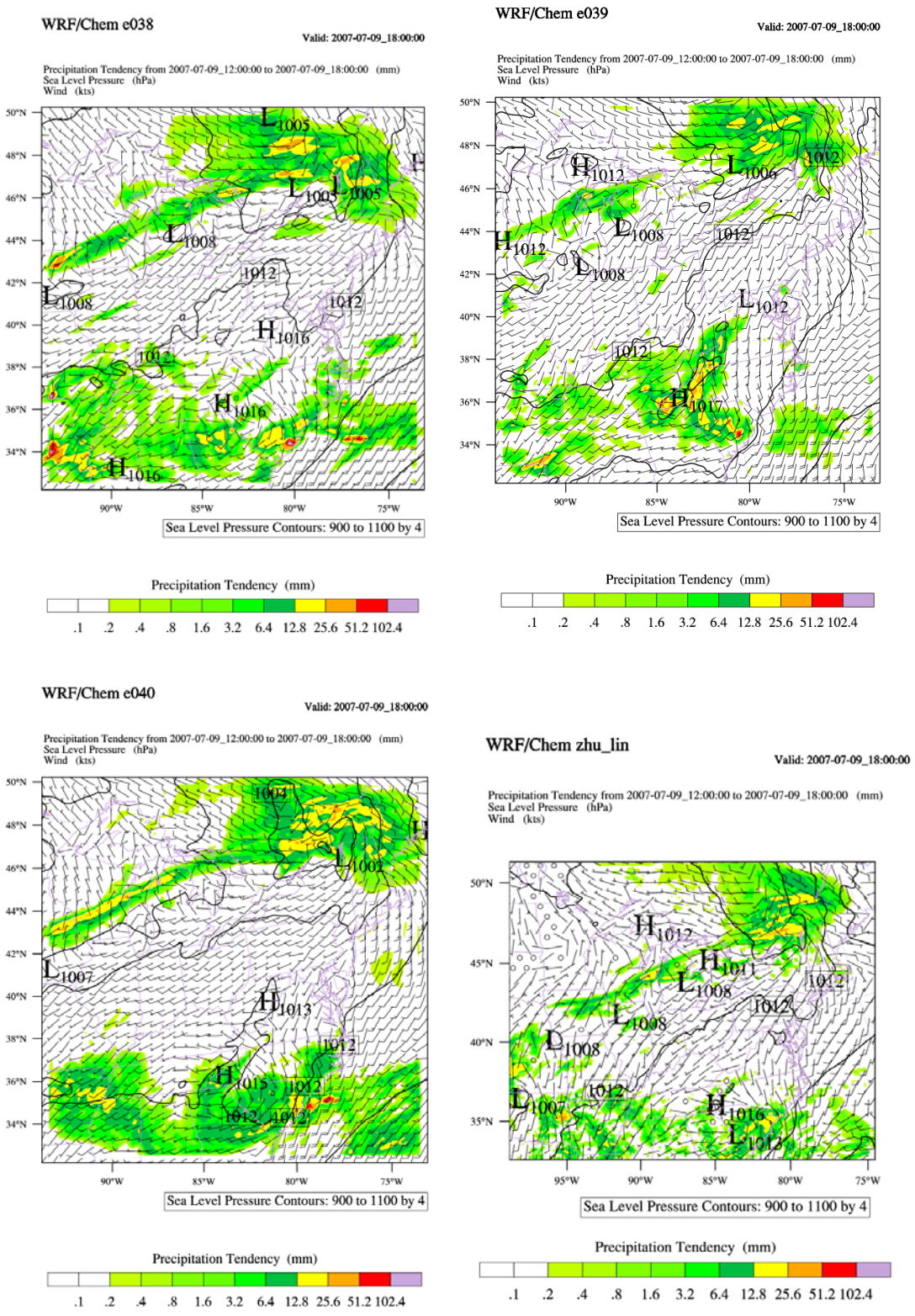

Figure 3.21 Accumulated 6 hr precipitation, surface pressure and surface wind barbs ending July 9, 18 UTC for a) E038, b) E039, c) E040, and d) [*Zhang et al*, 2010] simulation.

E038 and E40 produce larger 6-hr accumulated precipitation fields within the Great Lakes squall line and off the coast of southeast U.S, in closer agreement with the NCEP precipitation observations. Nudging only T and q (E039) produces most of the accumulated precipitation in the southeast U.S over parts of Georgia, North Carolina and Tennessee; while the peaks were observed from Arkansas to Alabama.

Zhang et al. [2010] improved WRF forecast for July 9, 2007 using both OBSGRID and FDDA nudging (Figure 3.21d). *Zhang et al* [2010] used NCEP North American Mesoscale (NAM) analysis meteorological input fields and soil moisture fields, available every 3 hours and a two times faster integration time step of 90s. Based on representation of convective storms E038 FDDA nudging experiment is better of the four that were performed for this dissertation. Yet E_BASE (OBSGRID and no FDDA) experiment compares better with observed surface pressure and precipitation fields and *Zhang et al.* [2010] simulation. OBSGRID nudging improved model performance and FDDA nudging led to more errors for the modeling setup used in this dissertation. The differences in meteorological initial and boundary conditions, longer integration time step and a difference in radiation scheme could account for the differences in the FDDA nudging results with respect to *Zhang et al*. [2010] WRF simulation.

3.6 *Summary*

I have examined model performance in simulating a severe smog episode of July 2007 in eastern U.S. using surface trace gas observations from EPA AQS, Pinnacle State Park, Great Smoky Mountains, SEARCH stations, and ozonesondes from Beltsville, MD. Modeled 8-hr O_3 daily maxima suggest that WRF/Chem

simulates well the onset and dissipation of the smog event. The model simulates correctly the spatial pattern of surface ozone over most of the domain. Mean bias, root mean square error and correlation coefficient (r) from WRF/Chem 8-hr O_3 maximum and observations during July 6-11, 2007 were 0.59 ± 11.0 ppbv, 11.0 ppbv, and 0.7, respectively. However the low mean biases are partially the result of underpredicted O_3 in the northeast and overpredicted O_3 in the southeast. The model had the greatest hit rate of 48.6 % on July 9 and averaged 30.2 % false alarm ratio over the simulated period.

WRF/Chem captures mean ozone mixing ratios, but shows less variability than is observed. The model underestimated the magnitude of the 8-hr maxima observed on July 9, 2007 in the densely populated northeast. WRF/Chem has difficulty correctly representing O_3 mixing ratios in the southeast, showing a high bias of 8-11 ppbv at the peak of the smog event. Comparison at individual sites showed that the model captures the diurnal variations in O_3 and passage time of the cold front. WRF/Chem underpredicts daytime O_3 at rural Pinnacles, NY and Great Smokies, TN sites and suburban Aldino, MD AQS site. In JST and YRK, GA sites daytime and nighttime O_3 is overpredicted. Ozone overprediction in the southeast U.S. is attributed to overpredicted temperature (>1.5°C) in the model. In a separate run, 3-D analysis nudging increased surface ozone biases by 12 ppbv in the southeast U.S. This is attributed to increased insolation and temperature in the FDDA run.

The RADM2 chemical mechanism used in this simulation does not account for NO_x lifetime-extending reservoir species: organo-nitrates and nitryl chloride. For future work, the lifetime of NO_x in model could be tuned (by adjusting reaction rates

within known uncertainties, for example) to match observations, but additional observations of alkyl nitrates and other NO_y species would help develop a more accurate and explicit chemical mechanism. In sensitivity simulation where heterogeneous production of HNO_3 was eliminated to simulate the maximum effect of recycling of NO_x through $ClNO_2$ chemistry, model NO_x biases decreased at Pinnacles, JST and YRK sites during the night time and during daytime at the YRK site. Daytime O_3 mean biases at Aldino, Pinnacles and Great Smokies sites were reduced by 3-5 ppbv. Another sensitivity simulation showed that O_3 dry deposition velocities contribute to insufficient nighttime depletion of O_3 at SEARCH sites and Aldino, MD.

Analysis of Beltsville ozonesondes showed that the model captures the vertical distribution of ozone up to 600 hPa, but overestimates mid to upper tropospheric ozone mixing ratios. Daytime underestimation of surface O_3 is attributed to overestimated boundary layer height in the model. The overprediction of nighttime O_3 is attributed to high vertical mixing coefficient in the model. Modeled relative humidity profiles are in good agreement with observations below 800 hPa. While the model has difficulty capturing sub grid scale convection events, contributing to local redistribution of trace gases, the general signature of the pollution event is captured well. The model-simulated ozone plume extends into the 815 hPa pressure layer, a portion of the troposphere where ozone information can be retrieved from satellite measurements [*Liu et al.*, 2009]. Since the lowest portion of the free troposphere and the boundary layer are not easily measured from space, WRF/Chem can be used for interpreting the satellite measured tropospheric column ozone in the context of a

major surface pollution event. The focus of the next chapter is interpretation of satellite observations of O_3 and its precursors in the northeast U.S. during this severe smog episode using WRF/Chem.

Chapter 4 The impact of WRF/Chem lightning NO_x sensitivity study and comparison with satellite observations

4.1 *Introduction*

In the previous chapter I showed that WRF/Chem satisfactorily captured the spatial and temporal distribution of O_3 during the July 7-11, 2007 pollution episode. In general, the WRF/Chem model performance is better than NOAA's National Air Quality Forecast Capability (NAQFC) for July 2007 [*Eder et al., 2009*]. In this chapter, I will use a combination of model and remote measurements to characterize continental pollutant outflow over the western North Atlantic Ocean during this event. I will analyze a sensitivity simulation with model emissions enhanced in the mid to upper troposphere with lightning-induced nitrogen oxides to quantify effects of lightning on O_3 and NO_2 tropospheric columns. This is the first regional scale WRF/Chem simulation containing lightning-induced nitrogen oxides (LNO_x) for an ozone episode in the eastern U.S. WRF/Chem will be used to interpret satellite measured highly variable species such as tropospheric O_3 and NO_2 on scales on which in situ measurements are insufficient for validation Here I compare the WRF/Chem simulation with satellite observations and discuss the findings of the sensitivity LNO_x WRF/Chem simulation from an air quality perspective. WRF/Chem will be used as a platform to compare the representation of this pollution event by Tropospheric Emission Spectrometer (TES) and Ozone Monitoring Instrument (OMI)

aboard Aura. I will focus on how well the two instruments capture elevated lower tropospheric ozone associated with this poor air quality event.

It is difficult to measure planetary boundary-layer (PBL) and surface-layer ozone from space. The ability of satellites to detect tropospheric O_3 is critical towards understanding ozone formation in polluted regions, venting into the free troposphere, subsequent transport, and possible descent back into the boundary layer. Hyperspectral infrared or ultraviolet instruments such as TES [*Beer et al.*, 2001; *Worden et al.*, 2004] and OMI [*Levelt et al.*, 2006; *Schoeberl et al.*, 2007; *Liu et al.*, 2009] aboard the Aura satellite can measure ozone in the free troposphere directly albeit with coarse vertical resolution. In the past, satellite instruments could not directly retrieve tropospheric ozone from space due to the large signature of stratospheric ozone in the total column. Previous studies determined tropospheric ozone column distributions by subtracting the stratospheric ozone column from the total ozone column [e.g., *Fishman and Larsen*, 1987; *Hudson and Thompson*, 1998, *Ziemke et al.*, 2006; *Schoeberl et al.*, 2007].

CO, with a relatively long lifetime, has also been measured from space and used in identification of boundary layer pollution [*Clerbaux et al.*, 2008]. NO_2 is well suited for studying urban air pollution from space because of its high boundary layer source and short lifetime. U.S. urban and surface sources of NO_x are well quantified in satellite NO_2 measurements [e.g. *Kim et al.*, 2009; *Kar et al.*, 2010]. However when evaluating tropospheric NO_2 columns with remote sensing products, it is imperative to separate lightning-induced nitrogen oxides from local boundary layer pollution. *Hudman et al*. [2007] showed that regional lightning is the dominant

source of upper tropospheric NO_x and increases upper tropospheric ozone by 10 ppbv during the ICARTT campaign over the eastern U.S. and North Atlantic Ocean. *Allen et al.* [2010] scaled Global Modeling Initiative (GMI) CTM flash rates such that on a monthly basis the grid cell flash rates match those of the Optical Transient Detector/Lightning Imaging Sensor (OTD/LIS) [*Boccippio et al.*, 2000; *Boccippio et al.*, 2002; *Christian et al.*, 2003] climatology. They found that lightning-induced NO_x contributes significantly to summertime NO_x (0.09-0.16 ppbv) and O_3 (15-24 ppbv) at 300 hPa over the eastern U.S. *Martini et al.* [2010] found lightning-induced O_3 increases of 6-9 ppbv and 16-20 ppbv in the lower and upper troposphere, respectively, over the western North Atlantic using the UMD CTM. *Martin et al.* [2007] used GEOS-Chem to investigate contribution of LNO_x to O_3 and NO_2 columns in the tropical Atlantic region. *Jourdain et al.* [2009] verified that imposing a production of ~500 moles NO per flash for lightning occurring in the midlatitudes decreased the bias between model (GEOS-Chem) and TES O_3 over the U.S. by 40% compared with a simulation using ~250 moles/flash.

The subtropical Bermuda High is a dominant summertime feature driving eastern U.S. pollution export [*Hegarty et al.*, 2009]. *Li et al.* [2005] analyzed major outflow pathways for North American pollution to the Atlantic Ocean. They found that a semi-permanent upper level anticyclone centered over the southern U.S. in combination with a Bermuda High traps continental convective outflow and allows pollutants to recirculate, age and mix with lightning-induced NO_x emissions in the free troposphere. They also predicted rapid ozone production of 10 ppbv day^{-1} and an ozone maximum (> 80 ppbv) in the upper troposphere across the southern U.S before

export to the Atlantic. The O_3 maximum was confirmed by measurements from the Intercontinental Transport Experiment (INTEX-A) [*Singh et al.*, 2006; *Singh et al.*, 2007] and INTEX Ozonesonde Network Study (IONS) campaign [*Thompson et al*., 2007; *Cooper et al*., 2006]

4.2 *Satellite Instrument Retrievals*

Over the course of the July 7-11, 2007 smog event, TES and OMI instruments on board Aura satellite provided measurements of ozone at the same time (~1:30 pm local time) but from different spectral regions and with differing vertical resolution and sensitivity. Terra's MODIS instrument also provided aerosol optical depth (AOD) measurement at 10:30 am local time.

4.2.1 TES Ozone and CO Profile Retrievals

TES is a high resolution imaging infrared Fourier transform spectrometer [*Beer et al.*, 2001], aboard NASA's Aura, a sun-synchronous polar orbiting satellite with a repeat cycle of 16 days. The TES spectral range is 650-3250 cm^{-1} with an apodized spectral resolution of 0.1 cm^{-1} and a nadir footprint of 5 km x 8 km. Standard TES products include vertical profiles of ozone and carbon monoxide (CO) from nadir observations during the Global Survey and Step and Stare operational modes. Global Survey measurements are about 220 km apart along the orbit track; Step and Stare are spaced every 30 km. The vertical resolution is about 6 km for clear-sky conditions, with sensitivity to the lower and upper troposphere [*Worden et al.*, 2004]. In this study I will use Version 3 (V003) of the TES Level 2 products. The ozone and CO profiles are selected based on quality control flags described in the TES L2 Data

User's Guide [*Osterman*, 2009]. Ozone c-curve retrievals and retrievals with emission layers are removed [*Nassar et al.*, 2008]. TES ozone retrievals exhibit positive biases of approximately 3–10 ppbv throughout the lower and upper troposphere [*Nassar et al.*, 2008]. While aerosols and clouds affect the vertical sensitivity of the TES retrievals, as characterized by the retrieval averaging kernel, they do not increase the bias in TES ozone measurements [*Kulawik et al.*, 2006]. The greatest sensitivity for TES is between 800-600 hPa, though it does have sensitivity throughout the troposphere allowing for a calculation of a tropospheric column ozone value. The TES tropopause height that is used in determining the column is not directly derived from the retrieval. It is based on the Global Modeling and Assimilation Office (GMAO) Goddard Earth Observing System Model (GEOS) version 5.2 tropopause.

4.2.2 OMI Measurements

The Ozone Monitoring Instrument (OMI) also aboard Aura is a nadir-viewing UV/Visible spectrometer that measures direct sunlight and backscattered light from the Earth's atmosphere [*Levelt et al.*, 2006]. OMI measures in three spectral regions (UV-1, UV-2, and VIS) over the wavelength range 270-500 nm with a spectral resolution of 0.42-0.63 nm. OMI provides daily global coverage using a 2-D CCD detector array with a cross-track swath of 2600 km and nadir spatial resolution of 13 km x 24 km. OMI ozone products that are used in this study are the OMI/MLS tropospheric ozone column product (updated from [*Schoeberl et al.*, 2007]) and the OMI level-2 ozone profile product [*Liu et al.*, 2009].

4.2.2.1 OMI/MLS tropospheric O_3

The OMI/MLS tropospheric ozone column is computed by subtracting the Microwave Limb Sounder (MLS) stratospheric column from the OMI total column derived using the OMTO3 algorithm. A forward trajectory model is used to increase the horizontal resolution and coverage of the MLS derived stratospheric column and to match OMI measurement times. Tropospheric column ozone is computed using two definitions of the tropopause: the 3.5 |PVU| surface and the < 2 K km^{-1} surface (approximately the World Meteorological Organization lapse rate criterion for the tropopause). The PV tropopause is lower than the lapse rate tropopause in mid-latitudes [*Schoeberl et al.*, 2007]. To minimize errors due to low PV tropopause, I will use the tropospheric column computed using the lapse rate tropopause. Validation against ozonesonde data shows a systematic negative bias of 5-6 DU due to a combination of biases from OMTO3 total column and MLS stratospheric column [*Schoeberl et al.*, 2007].

4.2.2.2 OMI level-2 tropospheric O_3

OMI level-2 profiles of partial ozone column densities are retrieved from the surface to ~60 km in 24 layers from OMI radiances using the optimal estimation technique [*Liu et al.*, 2005; *Liu et al.*, 2009]. The retrievals are constrained with month and latitude dependent climatological *a priori* ozone profiles and their standard deviations derived from 15 years of ozonesonde and Stratospheric Aerosol and Gas Experiment (SAGE) data [*McPeters et al.*, 2007]. The retrieved profiles contain ~6-7 degrees of freedom for signal, with 5-7 in the stratosphere and 0-1.5 in

the troposphere. In the tropics and mid-latitude summer, tropospheric information generally peaks between 500-700 hPa with vertical resolution of 9-14 km, and the retrievals are effectively sensitive to ozone down to ~800-900 hPa. OMI retrievals have been validated against ozonesonde observations [*Liu et al.*, 2009]. In Northern mid-latitude summer, tropospheric OMI profiles agree within 5% with ozonesonde observations and OMI tropospheric ozone columns show a negative bias of 1.6 DU. The OMI tropopause pressure is based on NCEP/NCAR 40-year reanalysis daily 12 pm LST tropopause pressure.

4.2.2.3 OMI NO_2

In this chapter I use two tropospheric NO_2 column products: the OMI NASA standard product (Level 3) [*Bucsela et al.*, 2008; *Celarier et al.*, 2008] and the Dutch OMI NO_2 (DOMINO) data product [*Boersma et al.*, 2007]. Each of these algorithms begins with the same slant column but differ in their separation of the stratospheric column from the tropospheric column and in their calculation of the tropospheric air mass factor. These differences lead to substantially different tropospheric column amounts [e.g., *Bucsela et al.*, 2008]. *Lamsal et al.* [2010] found that over the continental U.S. the mean summertime standard product NO_2 column was 22% higher than the DOMINO product and 67-74% higher than indirect estimates of columns based on bottom-up emission inventories and in situ surface layer measurements; the DOMINO column has a 25-33% high-bias with respect to the inferred columns. For this work, both the standard and the DOMINO products provide a good representation of the spatial NO_2 distributions. I will focus on their precision rather than absolute accuracy during the time period of interest.

4.2.2.4 OMI HCHO

I use column HCHO Level-2 gridded product (v003) with a horizontal resolution of 0.25°x0.25° [*Chance*, 2002]. The OMI instrument uses spectral windows from 327.5 to 356.5 nm for measuring HCHO. The overall error in the tropospheric HCHO column data is 25-31 % [*Millet et al.*, 2006]. OMI retrieved HCHO is averaged over July 2007 for comparison with model calculated HCHO,.

4.2.3 MODIS AOD

I use AOD from the MODIS instrument aboard the Terra satellite that is in Sun-synchronous polar orbit. MODIS uses observations of solar backscatter in seven spectral channels (470–2100 nm) for its aerosol optical depth (AOD) retrieval [*Kaufman et al.*, 1997; *Tanre´ et al.*, 1997]. Validation with the AERONET surface network indicates MODIS retrieval errors are $\Delta AOD = \pm 0.05 \pm 0.2 AOD$ over land [*Chu et al., 2002*] and $\Delta AOD = \pm 0.03 \pm 0.05 AOD$ over ocean [*Remer et al., 2002*] with respect to the AERONET surface network. MODIS AOD is useful in identification of U.S. pollutant outflow events [e.g. *Li et al.*, 2005]. Low MODIS AOD (< 0.2) is usually indicative of low aerosol loading over the ocean; MODIS AOD > 0.5 is frequently seen over urban regions in summertime eastern U.S [*Li et al.*, 2005].

4.3 *WRF/Chem Simulation*

The Weather Research and Forecasting model with online chemistry is used to simulate the outflow of pollutants during a severe smog episode in the Mid-Atlantic.

The base model O_3 simulation of July 6-12, 2007 was described in Chapter 3. The RADM2 chemical simulation is driven with meteorological data from the North American Regional Reanalysis (NARR) and chemical initial and boundary conditions from the MOZART-4 model. In this chapter, lightning NO_x sensitivity simulation is performed to quantify the contribution of lightning NO_x emissions to modeled O_3 and NO_2 tropospheric columns. Currently, there is no thoroughly tested WRF/Chem lightning NO_x algorithm that ensures that lightning emissions are placed in the same grid cells and the same times as parameterized deep convection occurs in the model, although such an algorithm is under development [*Hopkins et al.*, 2010]. Therefore, observed flash rates are used to determine when and where lightning NO_x emissions are placed in the model. The National Lightning Detection Network (NLDN) detects cloud-to-ground (CG) flash rates over the conterminous U.S. with detection efficiency above 90 % [*Grogan*, 2004]. Detection-efficiency adjusted CG flash rates from the NLDN were aggregated onto the model grid each hour. The resulting CG flash rates were then multiplied by z+1 to obtain the total flash rate, where z is the climatological intra-cloud/cloud-to-ground (IC/CG) ratio from [*Boccippio et al.*, 2001] after smoothing as in *Allen et al.* [2010]. I used a production rate per flash (both cloud-to-ground flashes (P_{CG}) and intracloud flashes (Pic)) of 500 moles NO (based on results from cloud-resolved modeling of *DeCaria et al.*, 2005 and *Ott et al.*, 2010) to calculate LNO_x contribution. Recent studies [e.g. *Cooper et al.*, 2006; *Hudman et al.*, 2007; *Jourdain et al*., 2009; *Allen et al.*, 2010] have used NO_x production per flash of ~500 moles NO per flash for analyses of tropospheric composition using the FLEXPART, GEOS-Chem, and GMI models. In the vertical,

lightning-induced NO emissions are proportional to pressure convoluted by the segment altitude distribution of flashes from Northern Alabama Lightning Mapping Array (LMA) [*Koshak et al.*,2004; *Koshak et al.*,2010].

4.4 *Circulation and convection setting*

The meteorological setup for the July 6-12, 2007 smog episode was described in detail in Chapter 3. Over the course of the O_3 event a subtropical Bermuda High pressure extended into the eastern half of U.S. It produced warm and humid weather conditions, large-scale subsidence, and light south-westerly surface winds. A mid-latitude cyclone formed over southern Canada on July 8, and persisted over southern and central Canada, intermittently retreating northeastward under the influence of the Bermuda High. Convection ahead of the warm and cold fronts associated with the mid-latitude cyclone produced lightning over the eastern U.S. Throughout this work, I will analyze the contribution of lightning activity on July 8-11 to tropospheric O_3 and NO_2 columns.

GOES East infrared images (Figure 4.1a) and NLDN lightning maps (Figure 4.2a) on July 8, 12 UTC indicated lightning-generating severe storms over the Great Lakes and off the coast of South Carolina and Georgia. On July 9, 18 UTC the cold front portion of the mid-latitude cyclone stalled over Illinois and Iowa, and the warm front passed over northern New England. NLDN reported lightning activity throughout the central U.S and over New Hampshire; locations of convective bands are confirmed by GOES imagery (Figure 4.1b). On July 10, a squall line ahead of the approaching cold front passed through Illinois, Missouri, and Oklahoma, generating severe lightning conditions (Figure 4.1c). Another band of thunderstorms passed

through the Washington, D.C.-Baltimore metropolitan area. The strongest storm appears off the North Carolina coast in the continental pollutant outflow region on July 10, 18 UTC. July 11, 18 UTC shows widespread convection ahead of a cold front passing from the northwest through the Mid-Atlantic region and marking the end of the smog episode (Figure 4.1d).

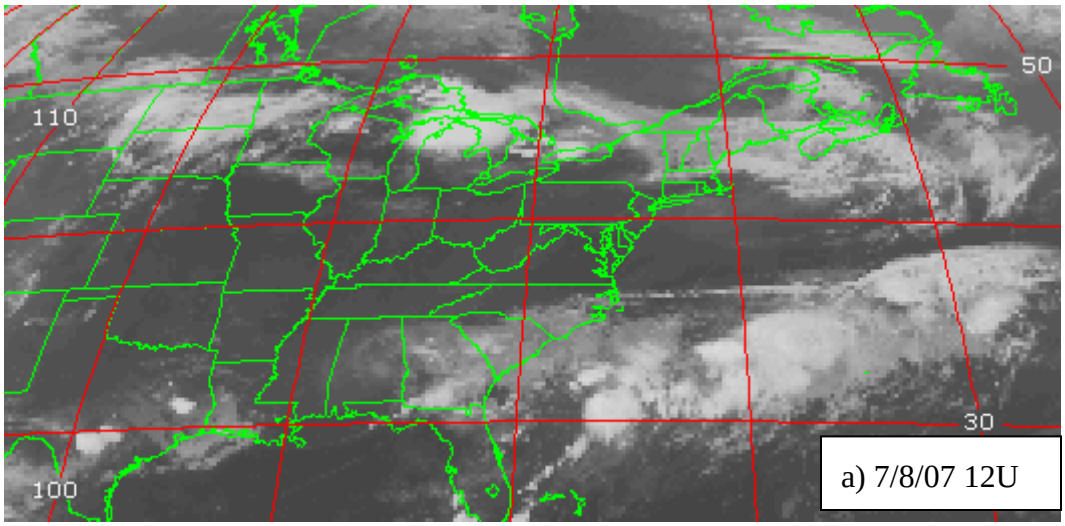

a) 7/8/07 12U

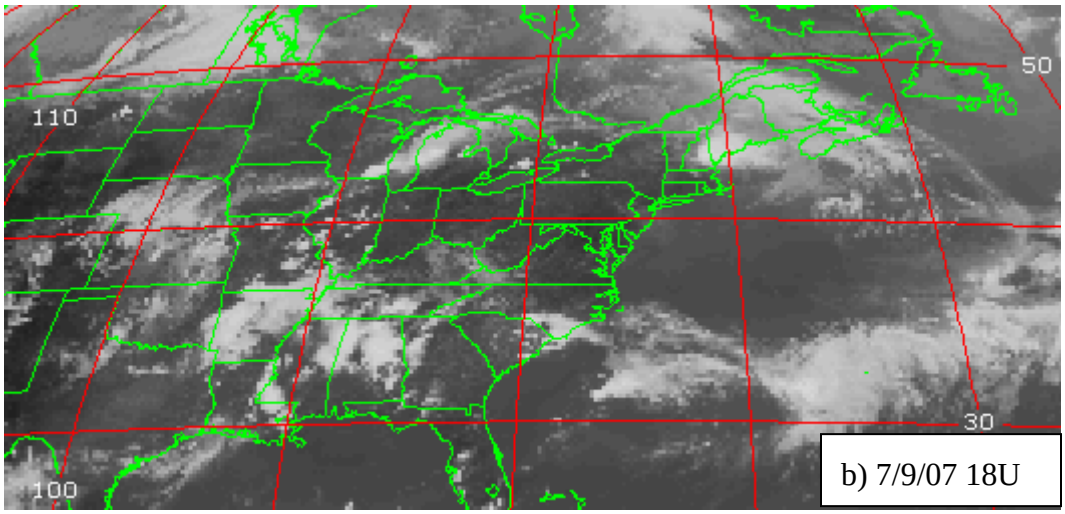

b) 7/9/07 18U

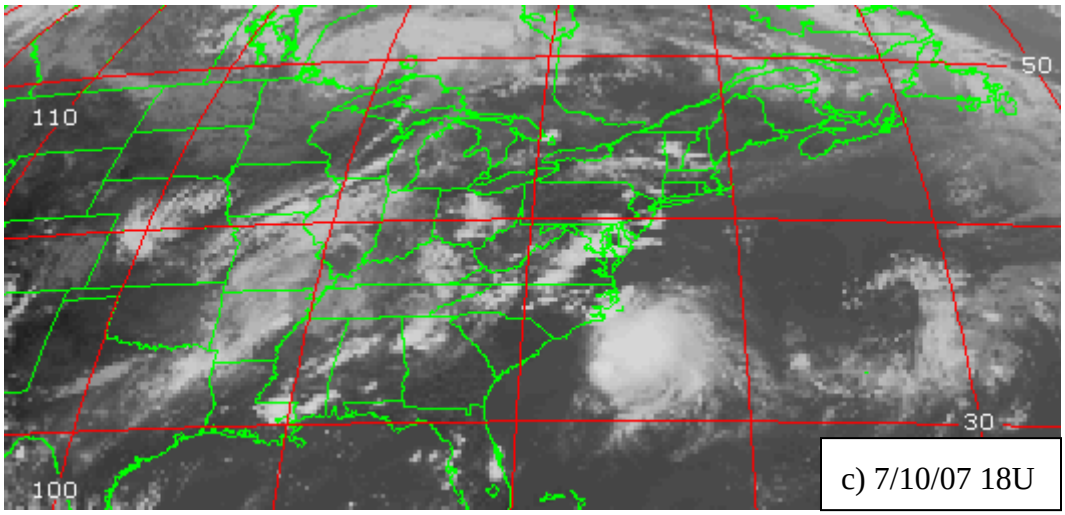

c) 7/10/07 18U

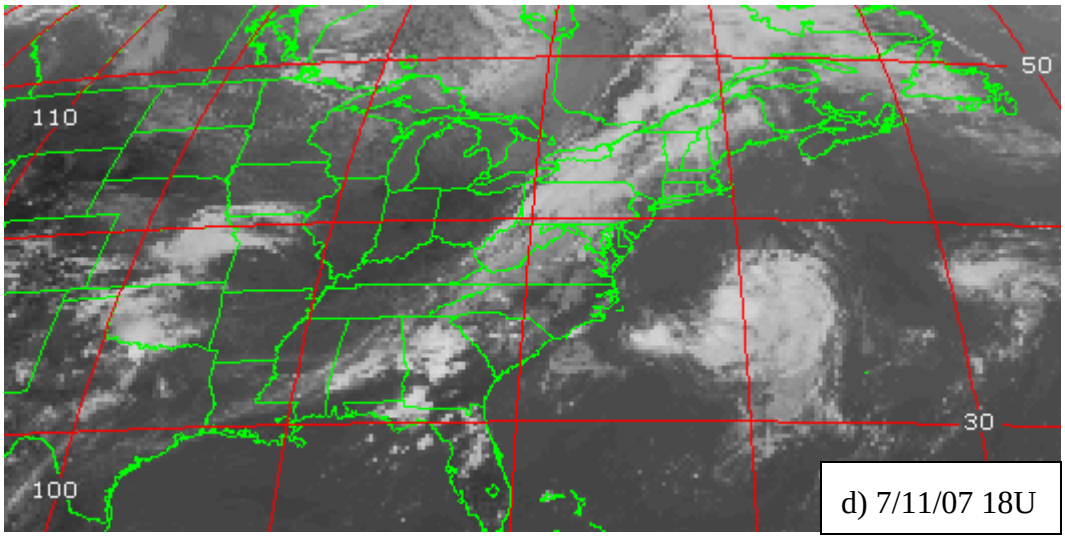

Figure 4.1GOES East infrared images (available at http://www.class.ngdc.noaa.gov) for selected convective storms during July 8-11, 2007.

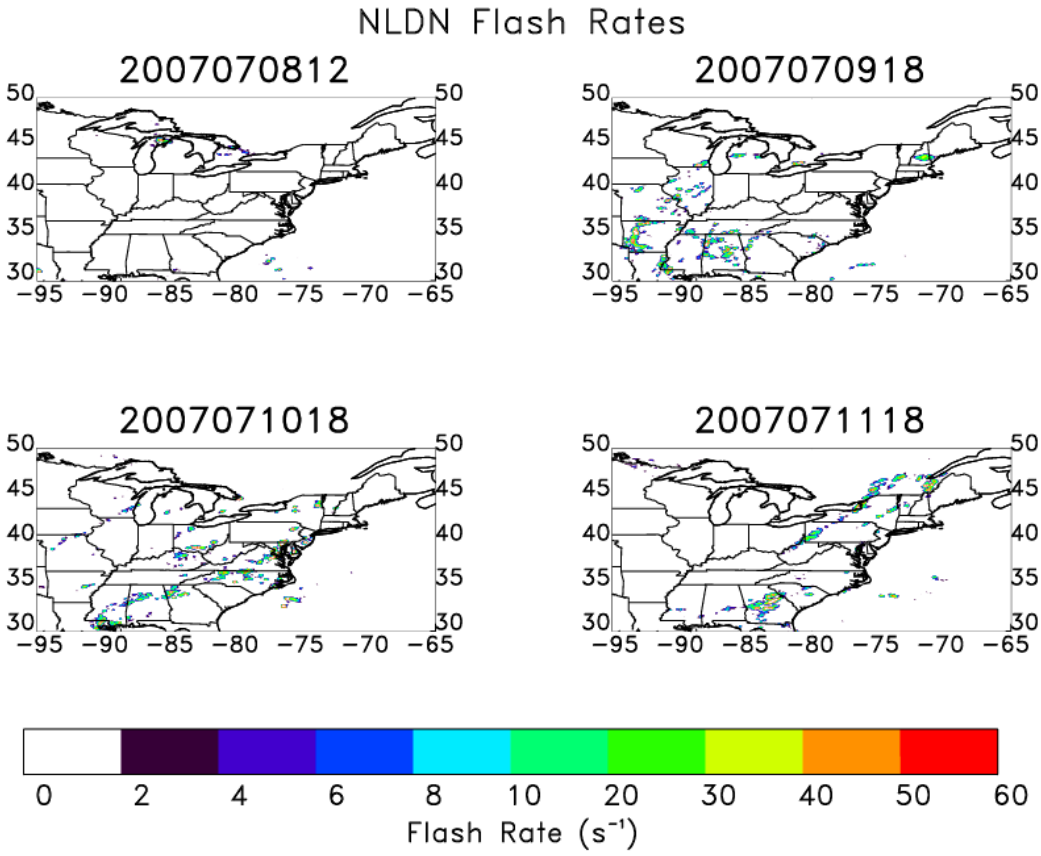

Figure 4.2 NLDN 24-hr flash rates for selected convective storms during July 8-11, 2007.

Figure 4.3 shows WRF/Chem 6-hr accumulated precipitation fields for the four time periods corresponding to the flash rate observations. WRF/Chem simulates the spatial distribution of convective storms in agreement with GOES IR imagery. Storms with simulated 6-hr accumulated precipitation fields > 0.4 mm correlate well with locations of NLDN lightning flash rates indicating that WRF/Chem captures the extent of convection in agreement with observations, and lightning NO_x emissions are placed correctly in the model. In the next section, the contribution of lightning NO_x emissions to tropospheric NO_2 and O_3 columns will be discussed.

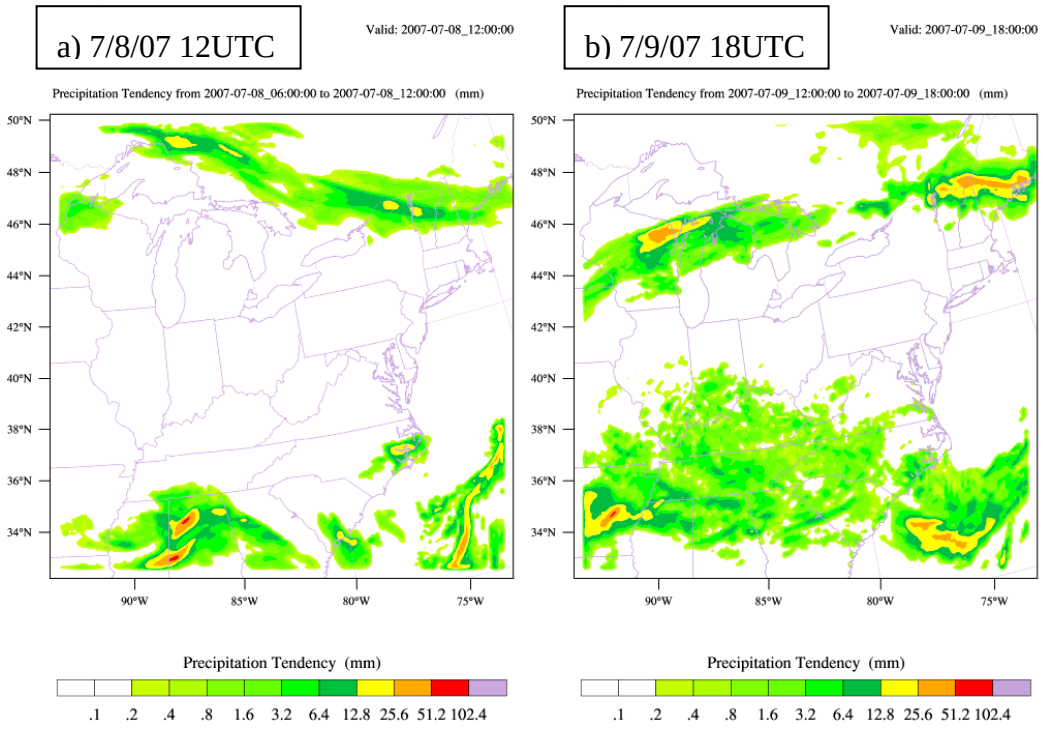

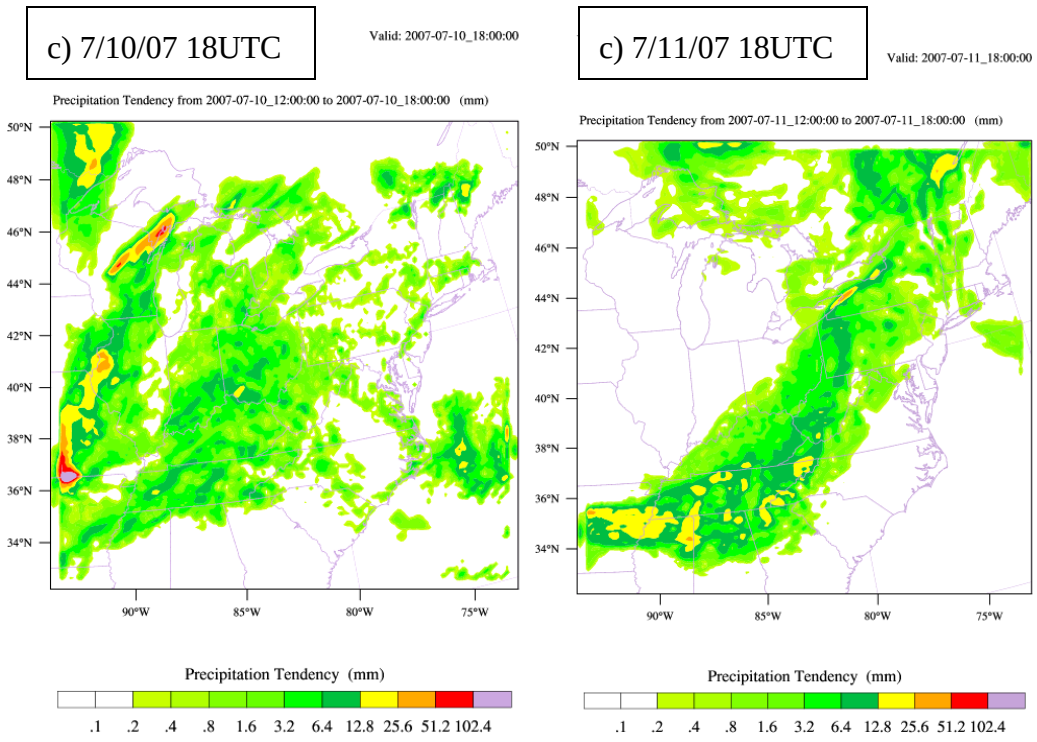

Figure 4.3 WRF/Chem 6-hr accumulated precipitation for convective storms on a) July 8, 12 UTC, b) July 9, 18 UTC, c) July 10, 18 UTC, and d) July 11, 118 UTC.

4.5 *Results and Discussion*

4.5.1 Lightning NO_x sensitivity study

4.5.1.1 WRF/Chem and OMI NO_2 comparison

The WRF/Chem simulation with lightning NO_x emission is used for interpretation of OMI and TES O_3 maxima off the east coast over the Atlantic where there are no in situ observations. First, I compare LNO_x WRF/Chem simulation with the OMI NO_2 tropospheric column. Figure 4.4 compares tropospheric NO_2 columns from the LNO_x and base modeling simulations with the OMI Standard NASA Level 3 gridded (0.25°x0.25°) product and the OMI DOMINO product on July 9, 18 UTC. OMI NO_2 cloud-free data availability is best on this day of the simulation. OMI

DOMINO Level 2 was aggregated onto a 0.5°x0.5° grid; OMI DOMINO averaging kernel was not applied to the model for this comparison. OMI NASA standard product shows more cloud-free pixels than the DOMINO product. Both OMI products and the base and LNOx model simulations show enhanced NO_2 in the densely populated northeast, along the major urban corridor stretching from Washington, D.C/Baltimore to New York City. Over this corridor, OMI standard NASA product shows NO_2 columns of 8-10 $x10^{15}$ molecules/cm^2 while OMI DOMINO product shows columns of 4-6$x10^{15}$ molecules/cm^2. WRF/Chem LNO_x sensitivity run and base case indicate 4-6 $x10^{15}$ molecules/cm^2 along the northeast urban corridor. NO_2 columns within the pollution outflow plume off the eastern U.S. over the Atlantic Ocean are measured at 1-4 $x10^{15}$ molecules/cm^2 (OMI NASA), mostly 1-2$x10^{15}$ molecules/cm^2 (OMI DOMINO) and 1-2 $x10^{15}$ molecules/cm^2

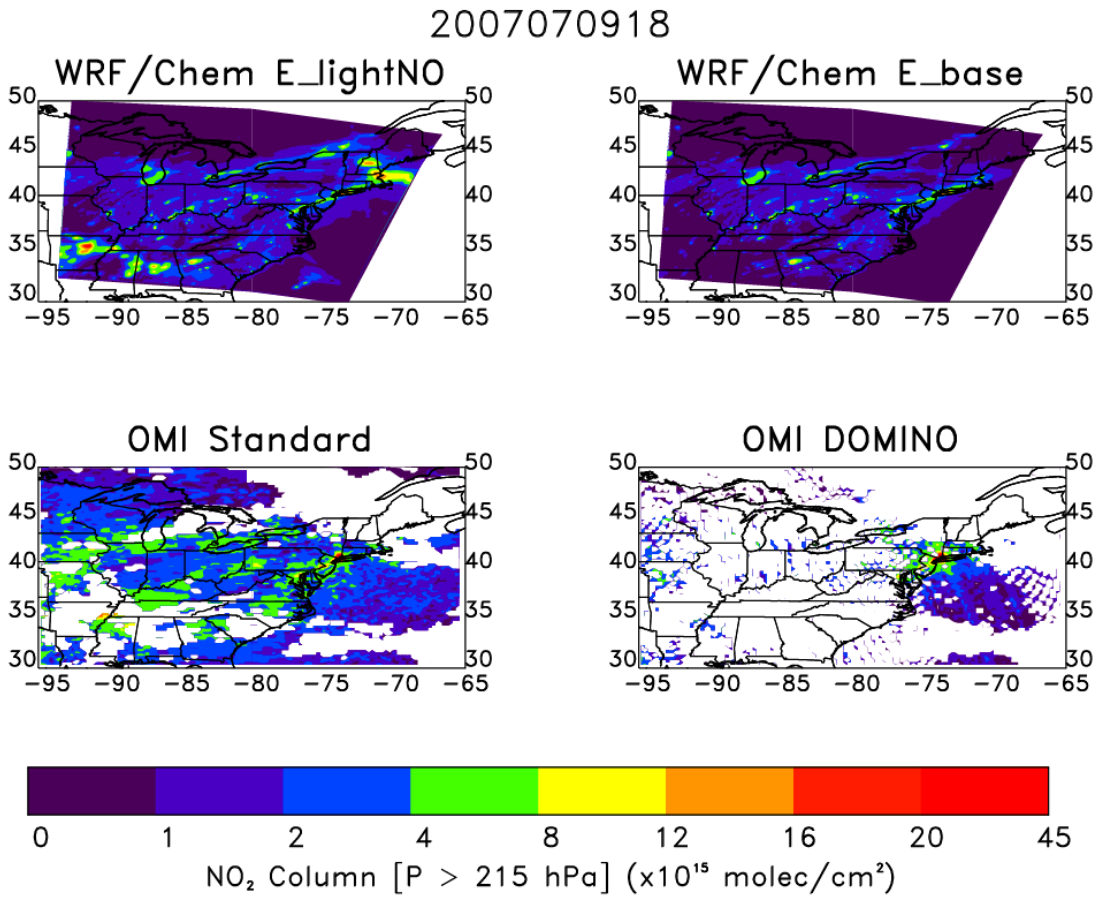

Figure 4.4 Distributions of tropospheric NO_2 columns for July 9, 18 UTC for a) WRF/Chem simulation with lightning NO emissions (E_lightNO) , b) WRF/Chem with standard emissions (E_base), c) OMI (NASA standard), and d) OMI DOMINO.

(WRF/Chem). Major urban areas such as New York, Washington/Baltimore, and Chicago are clearly visible in OMI and the model. Signatures of power plant NO_2 emissions are also seen in the Ohio River Valley and Pennsylvania. In rural regions across the domain the model underpredicts column NO_2 by 30-40 % with respect to OMI standard product. OMI standard product provides the best data coverage on July 9, 18 UTC – at the time of thunderstorm activity stretching from Arkansas to Georgia in the southeast and in northern New England. Unfortunately, extensive cloud cover north of Massachusetts limits model comparison with satellite for that storm. Part of

the NO_2 increment due to lightning seen in the model (Figure 4.4) over Arkansas is visible in the OMI NASA standard product. Within the cloud-free portion of the OMI NO_2 signal, the model calculates NO_2 column values of 4-10 $x10^{15}$ molecules/cm^2, with maxima reaching 14.8 $x10^{15}$ molecules/cm^2. OMI NASA standard NO_2 product shows peak values of $10.6x10^{15}$ molecules/cm^2 to the south of the model peak. OMI DOMINO product shows 2-4 $x10^{15}$ molecules/cm^2 in the vicinity of the storm, but most of the signal is lost due to extensive cloud cover. Overall, lightning sensitivity simulation produced expected NO_2 tropospheric enhancement in the vicinity of convective storms, as identified by OMI on July 9.

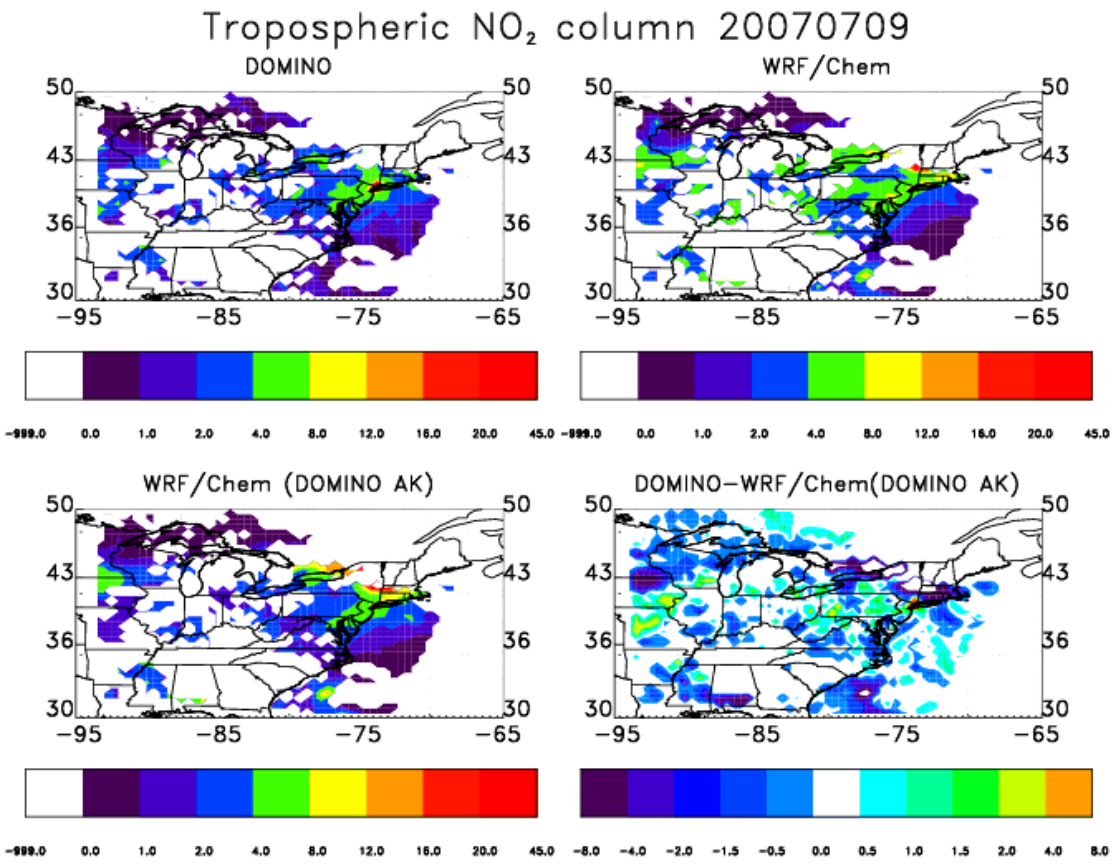

Figure 4.5 Distributions of tropospheric NO_2 columns for July 9, 18 UTC for a) DOMINO product b) WRF/Chem simulation with lightning NO emissions (E_lightNO) on 0.5°x0.5° DOMINO grid, c) WRF/Chem after application of the DOMINO averaging kernel, and d) difference between DOMINO and WRF/Chem (DOMINO AK).

Figure 4.5 shows the comparison of DOMINO product and WRF/Chem model before and after application of the DOMINO averaging kernel on a 0.5°x0.5° degree grid. Application of the DOMINO averaging kernel slightly decreased WRF/Chem tropospheric column along the northeast urban corridor and the Ohio River Valley. The difference between DOMINO and WRF/Chem convolved with DOMINO AK is 0.5-1.5 ppbv over parts of Maryland, Pennsylvania, and New Jersey. Large negative differences on the edge of extensive clouds in Northern New England are probably due to large errors in DOMINO retrievals in the presence of clouds. In general, WRF/Chem processed with DOMINO AK is in agreement with DOMINO NO_2 product.

4.5.1.2 WRF/Chem and OMI HCHO comparison

Average OMI and WRF/Chem tropospheric HCHO columns averaged over July 6 – July 11, 2007 are shown in Figure 4.6 and Figure 4.7, respectively. Highest HCHO values are expected in regions with high deciduous, coniferous and mixed forest density such as along the Appalachian Mountains and also along agricultural areas. Emitted isoprene quickly reacts with hydroxyl radical (OH) in the presence of sunlight to form HCHO. WRF/Chem is underestimating the peak HCHO column values in the Southeast U.S. This suggests that some of the model biases in the Southeast U.S. (discussed in Chapter 3) are not caused by high biogenic VOC emissions in the model. In fact, specification of isoprene emissions is an inherent model uncertainty. Here, biogenic emissions are calculated each time step using the BEIS3.11 algorithm. Biogenic isoprene emissions are a function of temperature and photosynthetic active radiation [*Guenther et al*., 1993]. Isoprene emissions are highly

dependent on the leaf temperature assigned to a model grid box [*Pierce et al*., 1998]. *Grell et al.* [2005] improved model performance for the summer of 2002, by assigning ambient air temperature to leaf temperature, instead of the default ground surface temperature.

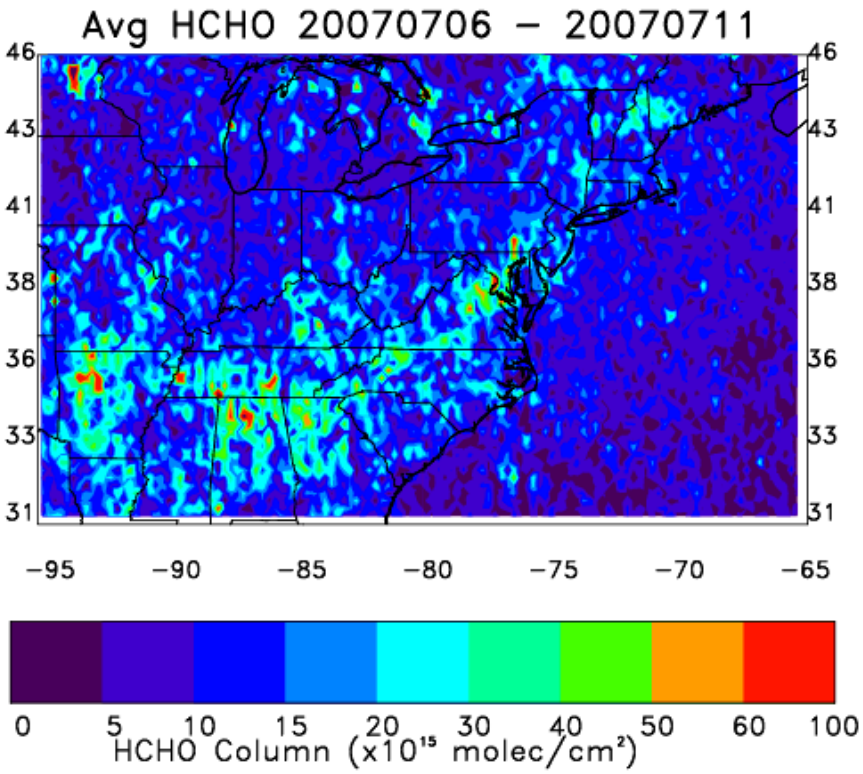

Figure 4.6 OMI total column HCHO averaged over July 6 – July 11, 2007. July 2007 monthly mean OMI HCHO is similar to this 7-day mean. Stratospheric contribution to total HCHO column is small.

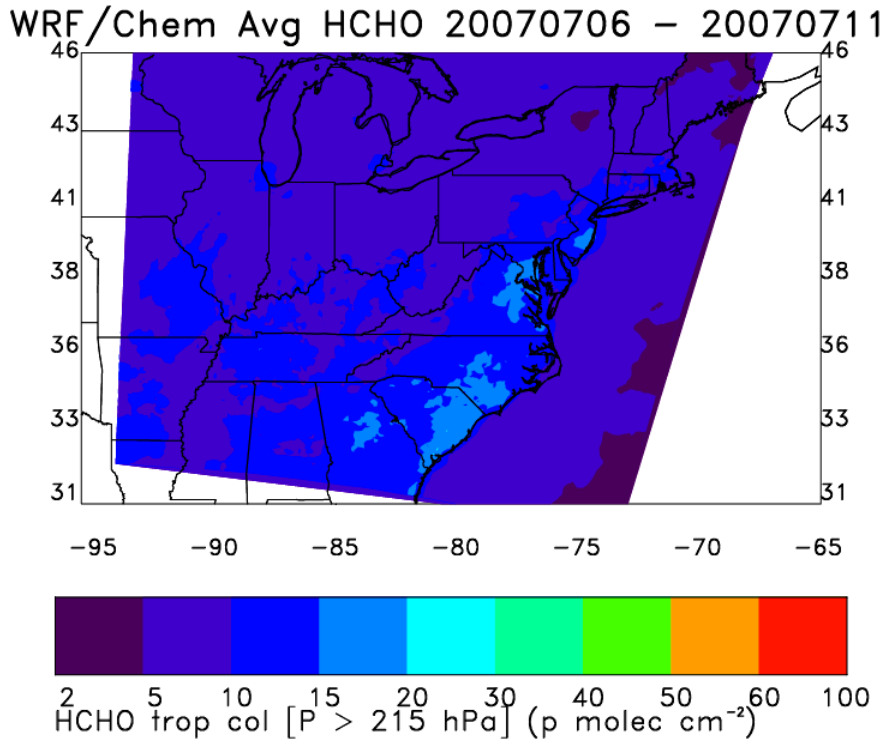

Figure 4.7 WRF/Chem tropospheric column HCHO averaged over July 6-11, 2007.

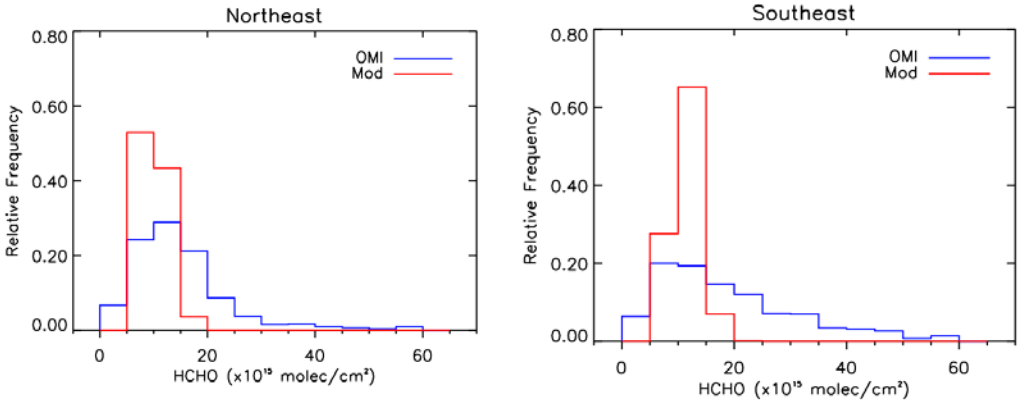

Figure 4.8 Frequency distribution of satellite-retrieved (blue line) and modeled HCHO (red line) for July 6-11, 2007 for a) Northeast U.S. [80°W-90°W; 32°N-36°N], and b) Southeast U.S. [75°W-82°W; 36°N-42°N].

Figure 4.8 shows the frequency distribution of WRF/Chem and OMI HCHO for July 6-11, 2007 over the northeast U.S. [80°W-90°W; 32°N-36°N], and Southeast U.S. [75°W-82°W; 36°N-42°N]. The maximum model HCHO columns are approximately 20 x10^{15} molec/cm^2; observed HCHO peaked at 60 x10^{15} molec/cm^2.

The model overpredicts the frequency of average HCHO columns less than 15 $x10^{15}$ molec/cm^2. In general, HCHO columns in the model are underpredicted. The base case simulation and lightning sensitivity simulation produced similar results. Inclusion of lightning NO_x emissions has little impact on HCHO tropospheric column.

4.5.1.3 WRF/Chem NO_2 Column Sensitivity

The contribution of lightning NO_x emissions to the tropospheric column is defined as the difference between lightning NO_x sensitivity simulation and the base simulation described in Chapter 3. Figure 4.9 shows the July 8 -11, 2007 change in tropospheric NO_2 columns associated with lightning NO_x emissions. Largest lightning NO_x contributions are seen over and downwind of convective events. On July 8 and 9, large scale subsidence associated with an anticyclone over the Mid-Atlantic region suppresses convection and lightning activity. On July 8, 12 UTC, the LNO_x contribution in the vicinity of convective storms over the Great Lakes and off the coast of South Carolina (i.e. where LNO_x NO_2 column fraction is more than 80 %) is 4.14-4.61 $x10^{15}$ molecules/cm^2, with peak values of 15-22 $x10^{15}$ molecules/cm^2. These values are larger than what was obtained for eastern U.S. by *Martin et al.* [2007]. The contribution of lightning-induced NO_x from these storms to downwind TES and OMI O_3 retrievals during the Mid-Atlantic smog event will be examined in more detail in section 4.5.2. Afternoon thunderstorm activity is seen on July 9 over northern New England and part of southeast U.S. July 10 stands out with greatest LNO_x contribution across the domain. A band of thunderstorms passing through the Washington, D.C.-Baltimore metropolitan area is clearly seen in peak NO_2 values of

12-14 x10^{15} molecules/cm^2.

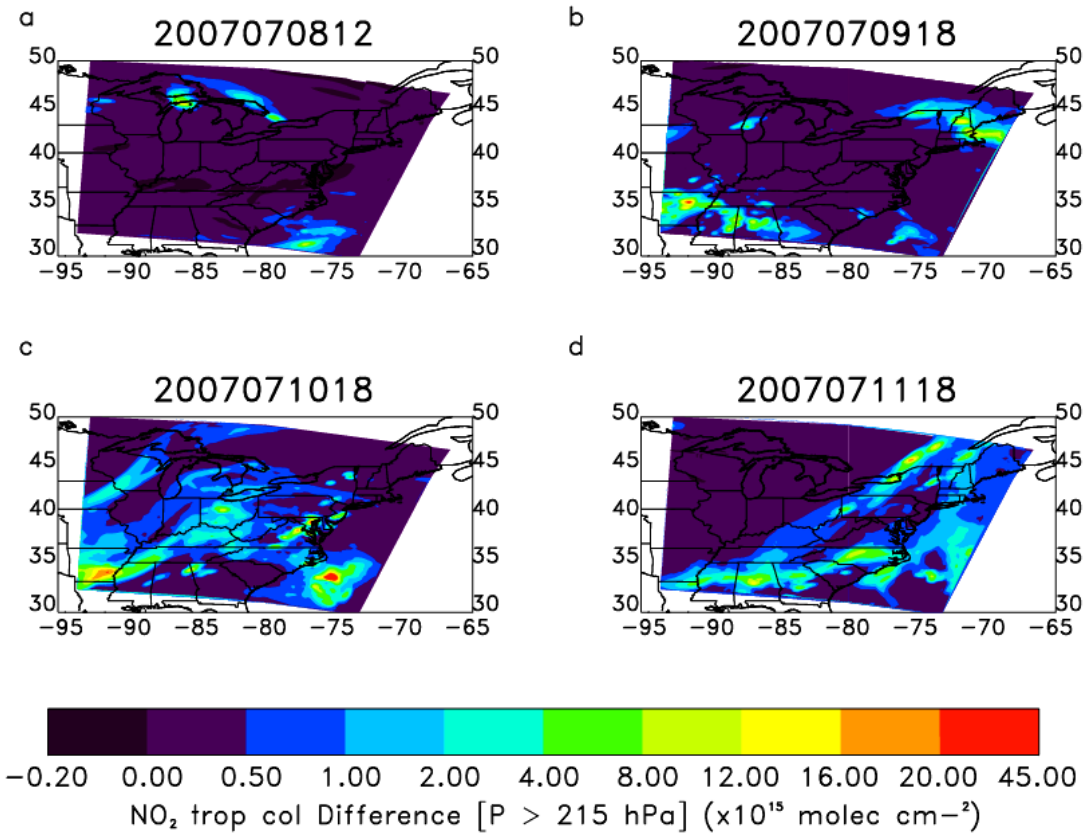

Figure 4.9 NO_2 tropospheric column difference between WRF/Chem simulation with lightning NO emissions (E_lightNO) and standard simulation (E_base) for July 8-11, 2007 smog event.

Upper level O_3 enhancements associated with convective activity in this region were analyzed in more detail using Beltsville, MD ozonesondes and WRF/Chem in section 3.5.4. The strongest storm appears off the North Carolina coast in the continental pollutant outflow region with ΔNO_2 above 40 x10^{15} molecules/cm^2. While the calculated twenty four hour accumulated precipitation within the storm off the coast of North Carolina on July 10, 18 UTC was 12-25 mm in the model and 100-125 mm in NCEP hourly, multi-sensor National Precipitation Analysis (NCEP NPA). The model is possibly underestimating the intensity of convective vertical mixing within these intense storms. July 11, 18 UTC shows widespread convection ahead of a cold

front passing from the northwest through the eastern U.S. The cold front pushes anthropogenic pollution in combination with lightning-induced NO_x off the east coast over the western North Atlantic.

4.5.1.4 WRF/Chem Surface and Column O_3 Sensitivity

Next, I determine the contribution of lightning NO_x to surface O_3 and tropospheric column O_3. Figure 4.10 shows the increase in model surface 8-hr maximum ozone in the Mid-Atlantic region due to lightning NO_x emissions. Ozone increases are expected in regions of enhanced NO_2 (seen in Figure 4.9) and downwind of convective events. Transport of lightning-produced NO_2, photochemical production of O_3, and longer lifetime explain more widespread ΔO_3 distribution than ΔNO_2 (compare Figure 4.9 and Figure 4.10). On July 8, the effects of convective storms over the Great Lakes on surface O_3 are negligible; thunderstorms off the southeast coast produced 4-6 ppbv enhancements. On July 9, 6-8 ppbv surface O_3 enhancements are seen over Arkansas, northern Alabama, and in the pollutant outflow region off the coast of North Carolina. July 10, 2007 convective activity in the Midwest increased surface O_3 by 4-6 ppbv slightly improving average hit rate from 44.6% in the base simulation to 46.4 % and critical success index (CSI) from 30.6 % to 31.1 %. Greatest enhancements of 8-10 ppbv are seen in the southeast U.S. on July 11. Overall, lightning emissions slightly increased surface O_3 model bias and error with respect to Air Quality System (AQS) (Table 4.1), but improved representation of the upper troposphere (as will be discussed in Table 4.4).

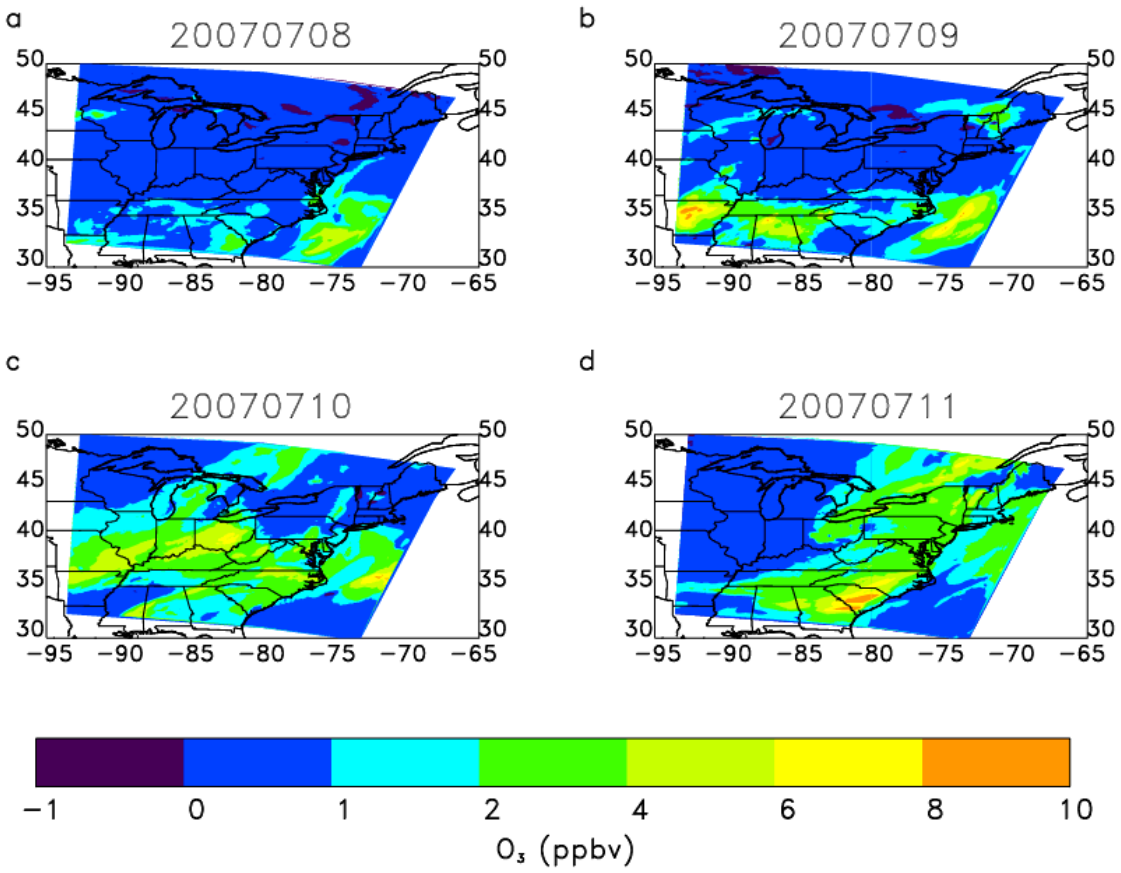

Figure 4.10 Surface 8-hr maximum ozone difference between WRF/Chem simulation with lightning NO emissions (E_lightNO) and standard simulation (E_base) for July 8-11, 2007 smog event.

The contribution of lightning NO to surface O_3 is shown as a function of surface O_3 concentrations (from e_base) in Table 4.2. In general, the LNO_x contribution to 8-hr maximum O_3 is largest on good air quality days (e.g., $O_3 < 65$ ppbv); contributions on poor air quality days are usually small. Although, on July 11, widespread convection ahead of the approaching cold front yields average ΔO_3 values of 1.51-1.99 ppbv for all levels of air quality. Typically, lightning-generating convective storms are conducive to mixing polluted boundary layer with cleaner upper level air; conversely, worst air quality days result from stagnant conditions and lack of convective storms.

	MB (ppbv)	NMB (%)	RMSE (ppbv)	NME (%)	r	σ (ppbv)
E_base	0.59	1.14	11.01	16.22	0.7	10.99
E_lightNO	1.46	2.81	11.39	16.89	0.68	11.29

Table 4.1 Average discrete evaluation results for observed and simulated 8-hr maximum ozone at AQS sites for WRF/Chem base (e_base) and lightning sensitivity run (e_lightNO). Evaluation of discrete forecasts was done using mean bias (MB), normalized mean bias (NMB), root mean square error (RMSE), normalized mean error (NME), correlation coefficient (r), and standard deviation (σ).

	O_3 <65	65 ≤ O_3 < 75	75 ≤ O_3 <85	O_3 ≥85
20070708	0.57	0.43	0.42	0.25
20070709	1.14	0.29	0.22	0.18
20070710	1.70	0.86	1.02	0.78
20070711	1.51	1.86	1.99	
All	1.23	0.61	0.62	0.50

Table 4.2 Mean contribution to surface 8-hr maximum O_3 (ppbv) in e_lightNO, varying with model air quality in the e_base simulation.

Figure 4.11 shows WRF/Chem recent lightning contribution to tropospheric column ozone. Lightning makes a broad contribution across the domain due to upper tropospheric NO_x lifetime of a few days. On July 9, 6-9 DU enhancements are seen off the coast of southeast U.S. Most notable enhancements of 10-12 DU are on July 10 and July 11, days of widespread convective activity in the region. O_3 enhancements of 10-12 DU are seen in the pollutant outflow region off the North Carolina coast on July 10 and over northern New England on July 11. Results from this section will be used to distinguish lightning-induced O_3 from anthropogenic O_3 within tropospheric column observed from space.

My results should be considered in the context of nonlinear response of O_3 production to LNO_x emissions. I cannot quantify LNO_x O_3 production in the real

atmosphere. The lightning-induced O_3 contribution is due to a combination of sources, such as LNO_x emissions and anthropogenic or natural hydrocarbons entrained into convective thunderstorms.

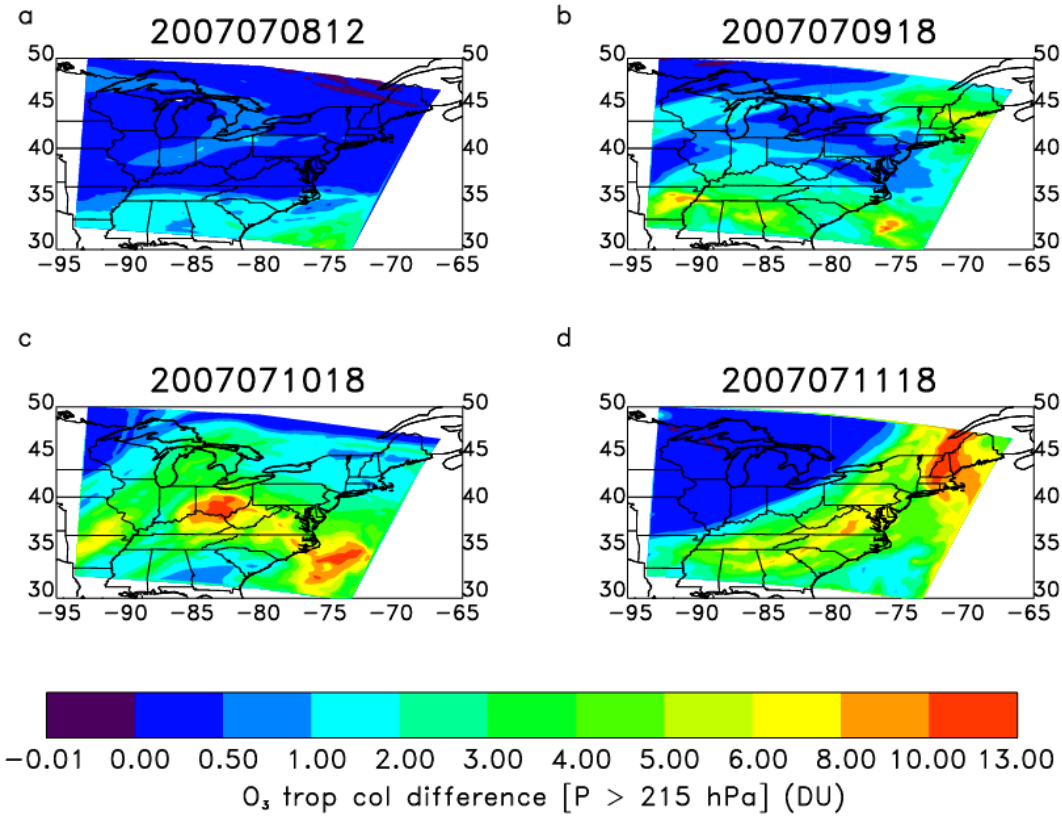

Figure 4.11 O_3 tropospheric column difference between WRF/Chem simulation with lightning NO emissions (E_lightNO) and standard simulation (E_base) for July 8-11, 2007 smog event.

Another limitation of the LNO_x sensitivity simulation is possible introduction of LNO_x emissions in the mid to upper troposphere where model convection is not co-located. This could result in slower LNO_x dispersal, temporary accumulation of NO_x and excessive O_3 production in the model, in the presence of O_3 precursors. Until a WRF/Chem algorithm that allocates LNO_x emissions to modeled convection grid cells is available [*Hopkins et al.*, 2010], approximation methodology used here is a starting point for WRF/Chem LNO_x studies.

4.5.2 Model and Satellite Measurement Comparison

For comparison with TES special observations, OMI and WRF/Chem model ozone profiles are sampled along the Aura orbit for the TES Step and Stare observations over the Mid-Atlantic region on July 7, 9 and 11, 2007. All profiles are interpolated onto the TES pressure grid. In the next section, I compare TES, OMI, OMI/MLS, and WRF/Chem derived tropospheric column ozone sampled along the TES orbit. This comparison does not use TES and OMI averaging kernels, and is meant as a qualitative comparison of the spatial distribution of model-based and satellite-based TCO values. In order to take into consideration the vertical sensitivity of TES and OMI instruments, in section 4.5.2.3 I apply TES and OMI averaging kernels to WRF/Chem for comparison of TES and OMI ozone retrievals.

4.5.2.1 TCO and AOD analysis

Figure 4.12 shows OMI/MLS (top), OMI (second row), and WRF/Chem (third row) calculated tropospheric column ozone over the Mid-Atlantic region for July 7, 2007 18 UTC (left), July 9, 2007 18 UTC (center) and July 11, 2007 17 UTC (right). TES TCO is overlaid on top of each sub-plot. The bottom row compares model smoothed with OMI averaging kernel (background) and model smoothed with the TES averaging kernel (filled circles) for the same time period. Discussion of averaging kernel analysis will follow in section 4.5.2.3. TES profiles that were filtered out based on the TES quality control flag are not plotted. Outflow of pollution off the U.S. east coast over the Atlantic Ocean is captured by all satellite products and the model during the three days of comparison.

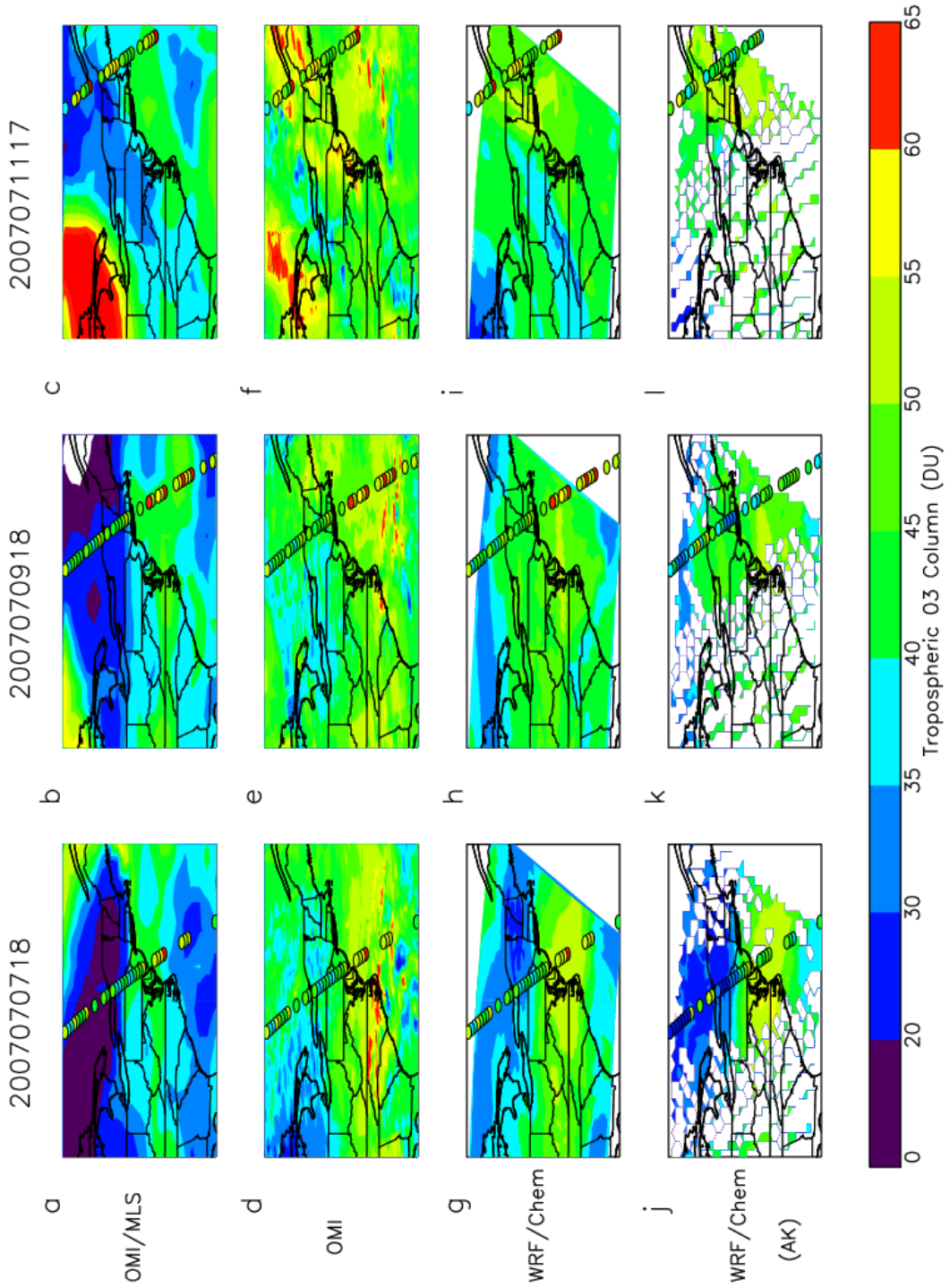

Figure 4.12 OMI/MLS (top row), OMI (second row), E_lightNO WRF/Chem (third row) tropospheric column ozone over the Mid-Atlantic region for July 7, 2007 18 UTC (left), July 9, 2007 18 UTC (center) and July 11, 2007 17 UTC (right). TES TCO is overlaid on top of each sub-plot. The bottom row shows WRF/Chem smoothed with OMI averaging kernel (AK) and WRF/Chem smoothed with TES AK (filled in circles along TES overpass.). OMI, OMI/MLS, and TES tropopause pressures are used for respective TCO calculations. WRF/Chem TCO was

calculated using the average of OMI, OMI/MLS, and TES tropopause pressure along the TES overpass (i.e. 175 hPa).

On July 7 WRF/Chem and OMI are showing a large region of TCO enhancement (Figure 4.12d and Figure 4.12g) off the east coast of the U.S. downwind of a July 5-6, 2007 smog event in South Carolina and Georgia.

Concurrent high AOD and O_3 are associated with boundary layer pollution outflow. Boundary layer ozone formation is sensitive to column aerosol content and thickness of the aerosol layer [*Kondragunta*, 1997]. AOD from MODIS (Figure 4.13a) indicates enhancements across North Carolina and South Carolina corresponding to the observed OMI O_3 enhancements in Figure 4.12d.

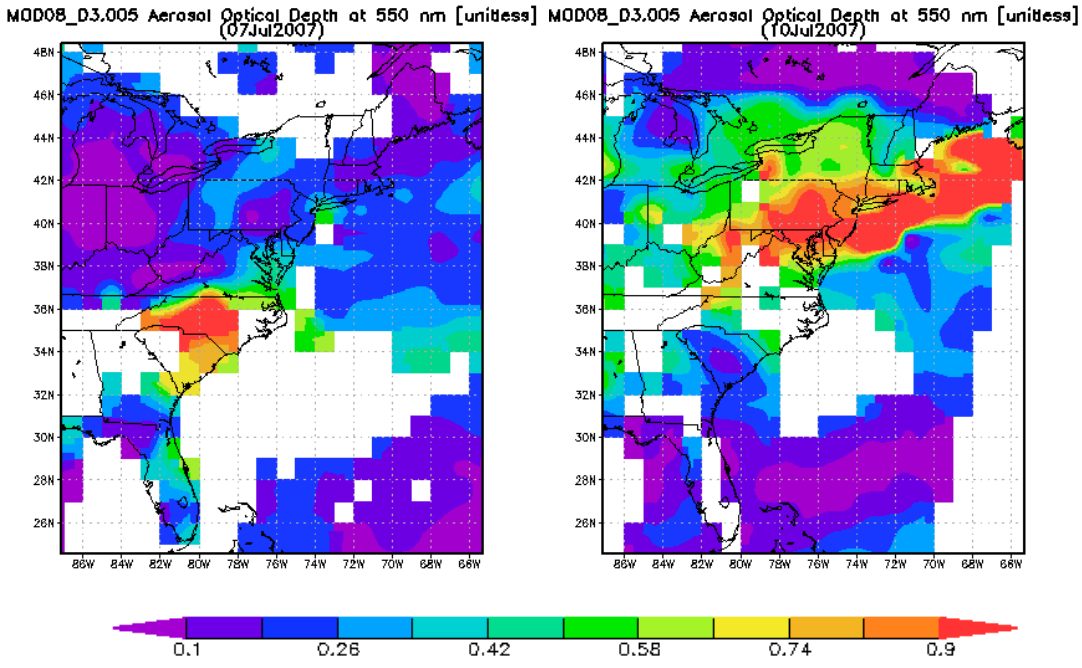

Figure 4.13 Aerosol optical depths at 550 nm from Terra/MODIS for (a) July 7 and (b) July 10. White areas indicate missing data.

Of the three TES overpasses the greatest TCO enhancements (60-64 DU) occur on July 9 in the continental pollutant outflow region over the western North Atlantic Ocean (31°N - 39°N and 71.6°W - 69.1°W). These ozone columns are in the 85th percentile of all July (2005-2008) TES measurements in this region. On the same day, OMI detects peak TCO values off the coast of North Carolina and South Carolina. OMI/MLS detects continental pollution outflow, but TCO values are the lowest of all calculated TCO products not exceeding 50 DU. In addition, OMI/MLS TCO is very low over the Northern New England and Great Lakes states. This is at least partially because the derived stratospheric ozone over northern New England and Canada is believed to be biased high and is subtracted off the OMI total column to yield small TCO values. There are typically systematic low biases in the surface to 200 hPa column [*Schoeberl et al.*, 2007] of about 6 DU due to high bias in the MLS stratospheric column. The biases are not subtracted in the TCO comparison to represent the product as it is available to the scientific community.

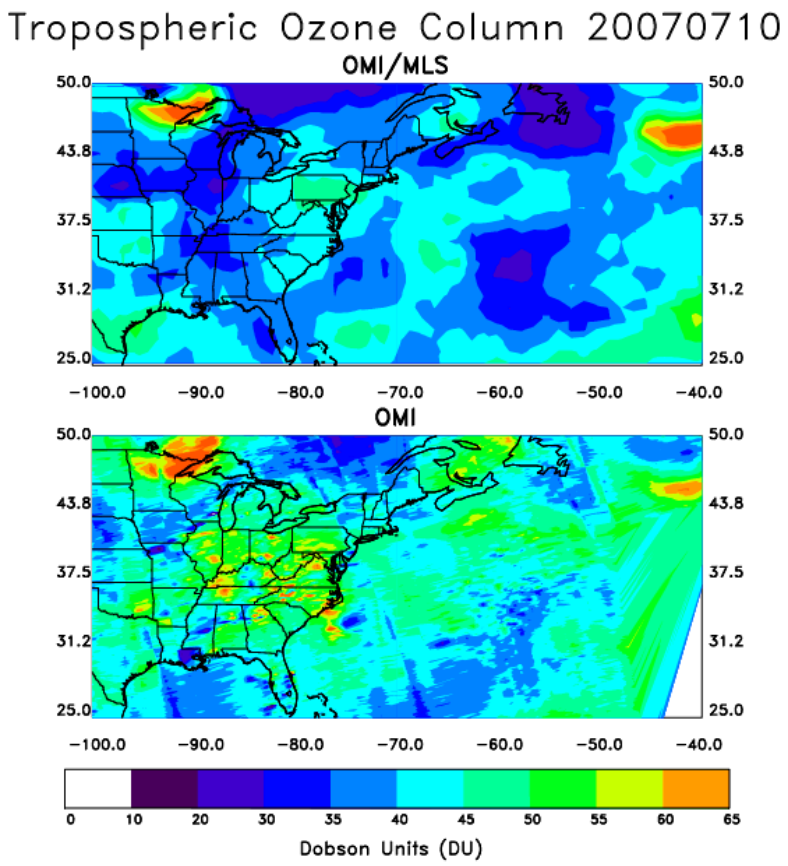

Figure 4.14 OMI/MLS and OMI tropospheric column ozone on July 10, 2007 18 UTC.

Early morning (~10:30 AM) July 10 MODIS AOD shows a mass of particulate matter extending from the mid-Atlantic region and New England out over the ocean (Figure 4.13b). OMI and OMI/MLS show significant TCO amounts across the Washington, D.C region at this time (Figure 4.14). MODIS AOD off the coast of North Carolina is not available, but AOD > 0.5 are visible in pixels adjacent to missing data. OMI observations on July 10 over North Carolina show an O_3 peak of 60-65 DU (Figure 4.14) that is attributed to surface pollution and lightning-induced NO_2 and O_3.

On July 11, a midlatitude cyclone is positioned over the Northeast U.S. with the warm front pushing through Massachusetts and the cold front stretching across

New York, Pennsylvania, and West Virginia (Figure 3.1e). OMI, TES and WRF/Chem identify high TCO values (> 60 DU) over northern New England states and Quebec, Canada associated with convective outflow and lightning ahead of the warm front (Figure 4.12c,f,i). Also a low level jet exists east of the Appalachian Mountains and transports pollution from southwest to northeast mixing with outflow ahead of the cold front as seen in TCO enhancements. High TCO values (> 65 DU) in the OMI and OMI/MLS products on July 11 over the Great Lakes region are associated with proximity of the 300 mb jet stream. The tropopause is ill defined at this location and uncertainties in stratospheric O_3 column are affecting the tropospheric O_3 column. WRF/Chem is unable to capture this intrusion since the model does not have stratospheric chemistry and the stratosphere is not well represented in the regional model. Overall, WRF/Chem simulates the continental outflow of pollution over the Atlantic Ocean in general agreement with satellite detected outflow, except that WRF/Chem peak TCO in the outflow region does not extend as far south as OMI and TES TCO (Figure 4.12g,h).

Differences in tropopause heights range from 0.1-1 km between the three satellite products. To minimize differences in TCO values due to differing tropopause heights, a pressure-averaged mean volume mixing ratio (VMR in ppmv) is calculated following the definition by *Ziemke et al.* [2006]:

$$VMR = 1.27\left(\frac{TCO}{P_{surface} - P_{tropopause}}\right), \qquad (1)$$

where TCO is in DU and P is in hPa.

TES, OMI/MLS, OMI, and WRF/Chem (e_lightNO) calculated tropospheric ozone VMRs along the on July 7, 9, and 11 TES overpasses are shown in Figure 4.15.

To separate the signature of continental outflow pollution I compare TCO VMR values over land and ocean (Table 4.3). Overall, TES detects the highest TCO VMR values, with average values of 47.5-49.5 ppbv over the ocean and 38.1-44.0 ppbv over land. Most of the land retrievals are in the regions of low pollution, while ocean retrievals sample the continental outflow region. OMI and OMI/MLS average TCO is also greater over the ocean. OMI/MLS has the lowest TCO values. WRF/Chem average TCO VMR is 41.8-45.0 ppbv over the continental outflow region and 30.9-44.7 ppbv over land. WRF/Chem simulated outflow region does not extend as far east as sampled on July 9 and 11 by the TES and OMI overpasses. This is probably because the model underpredicted peak 8-hr maximum O_3 on July 9 and was late in clearing out pollutants following the passage of the cold front in late afternoon July 11 (Section 3.5).

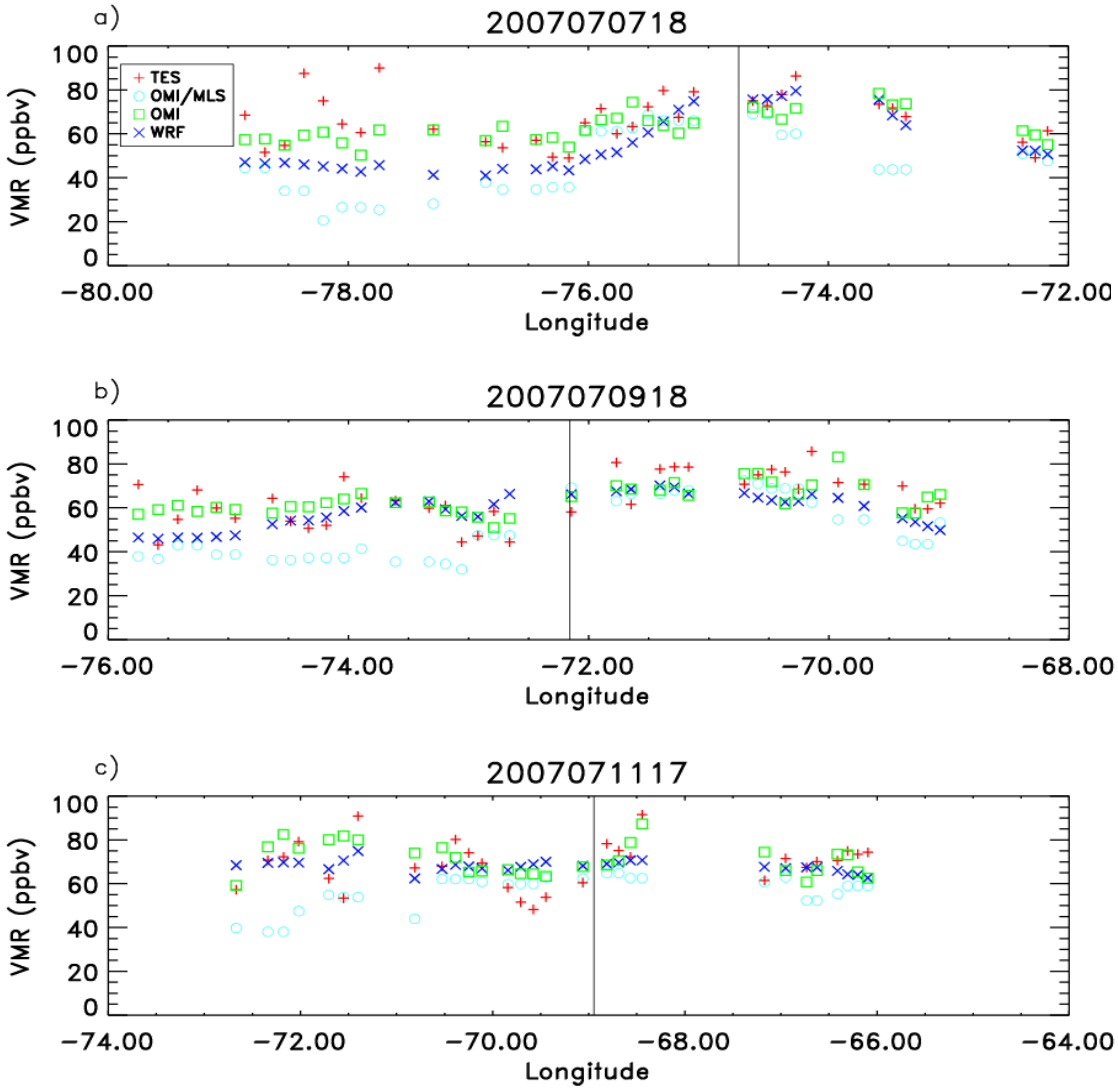

Figure 4.15 TES, OMI/MLS, OMI, and WRF/Chem (E_lightNO) calculated VMR tropospheric column ozone along the TES overpass on July 7, 2007 18 UTC, July 9, 2007 18 UTC and July 11, 2007 17 UTC. Direction of Aura overpass is from southeast to northwest (68°W to 80°W). Vertical line separates land profiles on the left from ocean profiles (right).

Model mean biases and correlations with OMI, OMI/MLS, and TES VMR along TES overpasses for the base and lightning sensitivity simulations are summarized in Table 4.4. Model correlation coefficients (R) are slightly improved from 0.46-0.64 in e_base to 0.47-0.67 in e_lightNO. Model mean bias with respect to OMI and TES is improved from -10.1 and -10.7 ppbv to -5.38 ppbv and -6.40 ppbv with inclusion of lightning NO_x emissions.

	TES (ppbv)		**OMI/MLS (ppbv)**		**OMI (ppbv)**		**WRF/Chem (ppbv)**	
	Ocean	*Land*	*Ocean*	*Land*	*Ocean*	*Land*	*Ocean*	*Land*
7/7/2007	47.5	41.1	36.0	26.7	44.7	39.3	45.0	30.9
7/9/2007	49.5	38.1	40.1	24.3	44.5	39.6	41.8	35.7
7/11/2007	49.5	44.0	39.2	34.1	44.6	47.5	44.6	44.7

Table 4.3 TES, OMI/MLS, OMI, and WRF/Chem TCO averages over ocean and land for July 7, 9, and 11, 2007.

	(WRF, OMI/MLS)		**(WRF, OMI)**		**(WRF, TES)**	
	R	*MB*	*R*	*MB*	*R*	*MB*
E_base	0.64	4.56	0.50	-10.1	0.46	-10.7
E_lightNO	0.67	9.30	0.65	-5.38	0.47	-6.40

Table 4.4 Correlations and mean biases for VMR calculated along TES overpasses for July 7, 9, and 11, 2007.

Mean bias with respect to OMI/MLS increased from 4.56 ppbv to 9.30 ppbv, due to lightning-induced O_3 enhancements over New England that were not seen in OMI/MLS TCO on July 11 but seen in WRF/Chem, TES and OMI (Figure 4.11d, Figure 4.12f, Figure 4.12i). Overall, satellite instruments and the LNO_x model simulation detect the greatest TCO values over the continental outflow region over the ocean. Adding lightning improved model and observation agreement.

4.5.2.2 TES and OMI O_3 and CO zonal averages and *a priori*

Figure 4.16 shows zonal averages (86°W - 68°W) of OMI O_3, TES O_3, TES CO, and their respective *a prioris* along the TES overpass for July 7, 9 and 11, 2007. The enhanced TES O_3 and CO from surface to 700 hPa between 31°N–35°N and 37°N -39°N is due in part to Mid-Atlantic pollution outflow transported by the predominantly westerly upper-level winds. Large enhancements in O_3 and CO are seen in ocean profiles (between 31°N–35°N and 37°N -39°N) that are not identified in the TES *a priori*(Figure 4.16 d,f).

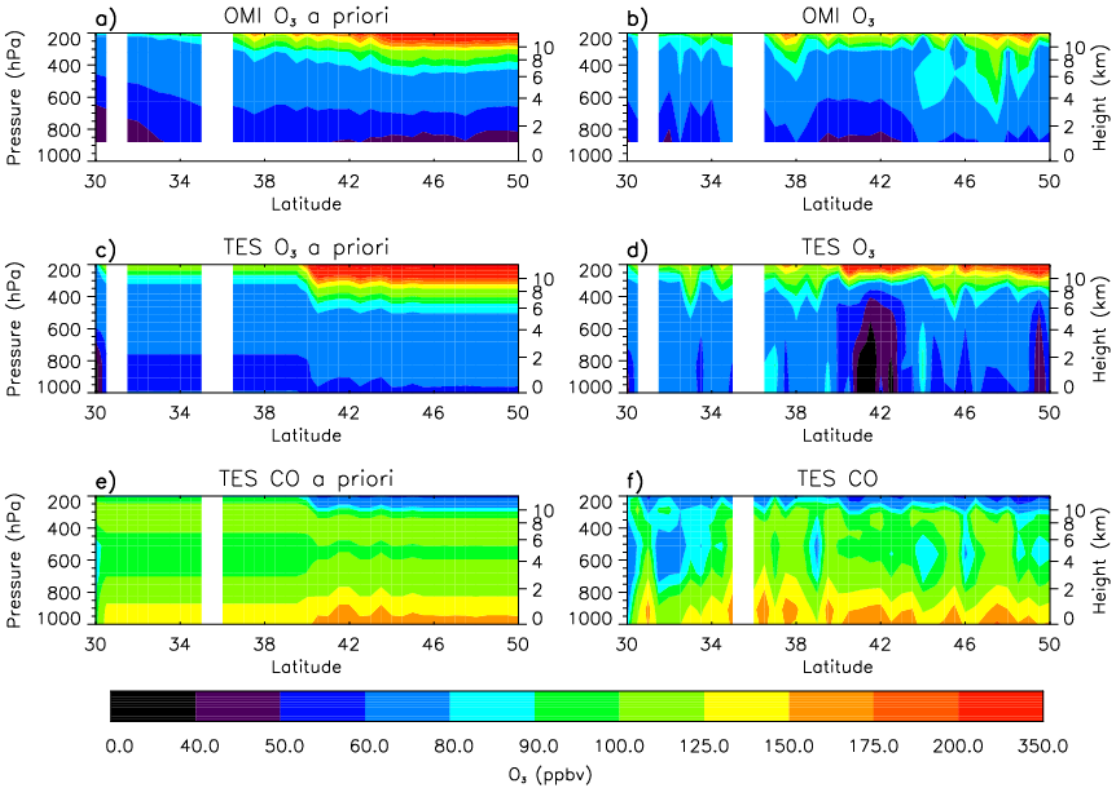

Figure 4.16 Zonal mean (68°W-86°W) concentration of a) OMI O_3 *a priori*, b) OMI O_3; c) TES O_3 *a priori*, d) TES O_3; e) TES CO *a priori*, and f) TES CO averaged over July 7, 9, and 11, 2007.

Surface pollution and lightning-induced O_3 contribute to the high tropospheric O_3 column over the continental outflow region. LNO_x O_3 is also seen in the northern New England high tropospheric O_3 values in TES and OMI. While TES and OMI *a*

priori profiles are similar, OMI shows a greater upper tropospheric O_3 contribution north of 43°N (Figure 4.16b). In these figures, OMI does not show substantial pollution outflow along the TES retrievals, however it does show considerable outflow 1-3° west of the TES overpass (Figure 4.12d, Figure 4.12e).

4.5.2.3 OMI and TES averaging kernel analysis

Direct intercomparison of TES and OMI ozone profile products requires accounting for the different vertical resolutions and sensitivities of the two instruments. TES and OMI retrievals contain unique averaging kernels (AK) and *a priori* profiles. When comparing satellite measurements to model simulations with greater vertical resolution than satellite retrievals, retrieval averaging kernels need to be applied to the high-resolution model output so the model is sampled with the same vertical sensitivity that the instrument is sampling the real atmosphere. The model ozone profiles (x_{model}) are convolved with the measurement averaging kernel matrix (A) to obtain the same vertical resolution profiles (x'_{model}) as satellite retrievals:

$$x'_{\text{model\_TES}} \approx x_{apriori\_TES} + \mathrm{A}_{TES}\,(x_{\text{model}} - x_{apriori\_TES}) \tag{2}$$

$$x'_{\text{model\_OMI}} \approx x_{apriori\_OMI} + \mathrm{A}_{OMI}\,(x_{\text{model}} - x_{apriori\_OMI}) \tag{3}$$

Where $x_{apriori}$ is the *a priori* profile used in OMI or TES retrievals. The difference between the model ozone processed with the TES and OMI O_3 averaging kernels is given by:

$$\Delta \approx x'_{\text{model\_TES}} - x'_{\text{model\_OMI}} \quad (4)$$

Zhang et al. [2010] used a chemical transport model (GEOS-Chem) as a platform for intercomparison of tropospheric ozone retrievals from TES and OMI for 2006. They found that 500 hPa differences between TES and OMI in summertime northern mid-latitudes exceeded 10 ppbv. Here I use WRF/Chem as a basis for comparing TES and OMI O_3 measurements for a smog event in the Mid-Atlantic region. WRF/Chem output is sampled at the location of satellite retrievals and interpolated onto TES (and OMI) pressure levels. Then using Equations 2 (and 3), the TES (and OMI) averaging kernel is applied to the interpolated model profiles to produce WRF/Chem profiles smoothed to represent TES (and OMI) vertical sensitivity.

Figure 4.17 shows the effect of smoothing WRF/Chem O_3 profiles with OMI vs. TES averaging kernels for all co-located Aura retrievals during the July 7, 9, and 11, 2007 smog event separated into retrievals over land and ocean. Correlations between the model smoothed with OMI AK and model smoothed with TES AK over ocean and land are 0.69 and 0.55, respectively.

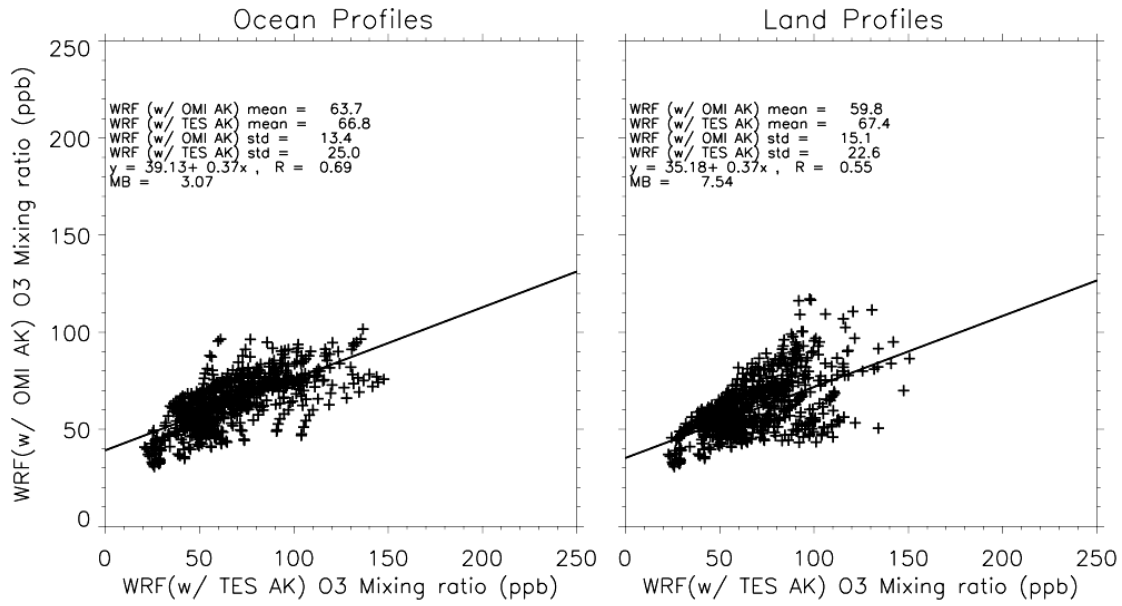

Figure 4.17 Differences between WRF/Chem (E_lightNO) smoothed with OMI averaging kernel and TES averaging kernel for Aura retrievals on July 7, 9, and 11, 2007 separated into ocean retrievals and land retrievals. The best-fit line is also shown.

The lower correlations over land may be due to different vertical distributions over land and water. Generally more surface ozone is found over land than over water. Mean differences between TES and OMI (from Eq 4.) are 3.1 ppbv over ocean and 7.5 ppbv over land. In Figure 4.12j -Figure 4.12i differences between model smoothed with TES and model smoothed with OMI averaging kernels is generally lower off the U.S. east coast and higher over northern New England States and southern Canada. The high bias of TES with respect to OMI is largest on July 7 over Southern Canada and on July 11 over northern New England.

Table 4.5 shows statistical analysis of model to satellite measurement comparison, before and after application of the TES and OMI averaging kernels. Mean bias, correlation coefficient (r) and reduced chi-squared (χ^2) were calculated for 1) TES(OMI) and raw WRF profiles and 2) TES(OMI) and WRF profiles convolved

with the TES(OMI) averaging kernel within three levels P> 700 hPa, 500-700 hPa and P>175 hPa. Reduced chi-squared (χ^2) analysis is given by:

$$\chi^2 = \frac{1}{N}\sum_{i=1}^{N}\left(\frac{Obs_i - Model_i}{\sigma_i}\right)^2, \quad (5)$$

where σ is observational uncertainty, contained within TES and OMI data sets. In general, a reduced chi-squared value of one indicates the model profile is within uncertainty of observations.

Overall, application of the averaging kernel improved model to satellite observation comparison. Application of the TES averaging kernel lowered model mean bias for the tropospheric column (P > 175 hPa) and lower troposphere (P>700 hPa) to -2.88 ppbv and -7.68 ppbv, yet slightly increased negative bias within the 500-700 hPa layer. Correlation coefficient decreased and reduced chi-squared increased following application of the averaging kernel. Model columns can decrease or increase after convolution with the averaging kernel, depending on the initial shape of model vertical profile. WRF/Chem peak TCO values were displaced to the west of TES retrieved TCO over the western North Atlantic, so low correlation values and high reduced chi-squared values are expected. Application of the OMI averaging kernel improved model to OMI comparison. Mean bias for the tropospheric column and lower troposphere was lowered, correlation coefficient was increased and reduced chi-squared value is pushed closer to unity (MB= -5.88 ppbv, r = 0.8, χ^2= 1.59). Between 500 hPa and 700 hPa, low model mean bias slightly increased. Statistical comparison shows that application of OMI/TES averaging kernels generally improves the OMI/TES and model comparison.

		TES		OMI	
		WRF Raw	WRF (TES AK)	WRF Raw	WRF (OMI AK)
P > 175 hPa	MB (ppbv)	-19.3	-2.88	7.12	-5.88
	r	0.46	0.19	0.52	0.80
	χ2	79.2	133.2	2.58	1.59
500-700 hPa	MB (ppbv)	-1.91	-2.74	-6.94	-7.27
	r	0.19	0.03	0.3	0.45
	χ2	11.1	27.2	5.02	2.61
P > 700 hPa	MB (ppbv)	-13.1	-7.68	-4.19	-5.67
	r	0.10	-0.09	0.34	0.42
	χ2	49.9	59.2	1.96	1.16

Table 4.5 Comparison of mean bias, correlation coefficient (r), and chi-squared of TES (OMI) and raw WRF and TES (OMI) and WRF convolved with TES (OMI) averaging kernel for three levels: P > 175 hPa, 500-700 hPa, and P > 700 hPa.

I initialized HYSPLIT [*Draxler and Rolph*, 2003] back trajectories from July 7 TES land retrievals with highest biases with respect to OMI. Back trajectories confirmed northwest to southeast flow through dense smoke west of the Hudson Bay at about 800 hPa on July 6 0-12 UTC.

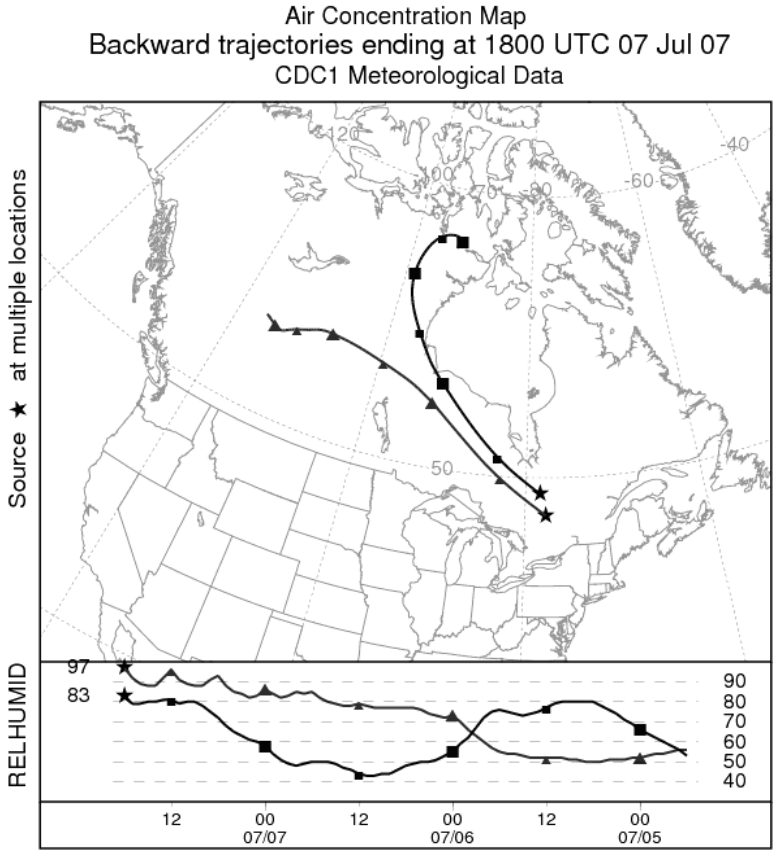

Figure 4.18 NOAA HYSPLIT back trajectories starting at 4km from TES observations on July 7, 2007 18 UTC where TES-OMI bias exceeded 30 ppbv.

The National Geophysical Data Center (NGDC) at National Oceanic and Atmospheric Administration (NOAA) satellite fire detections analyses indicated forest fires and smoke layer in this region of northern Manitoba, Canada during July 5-7, 2007 (Figure 4.19).

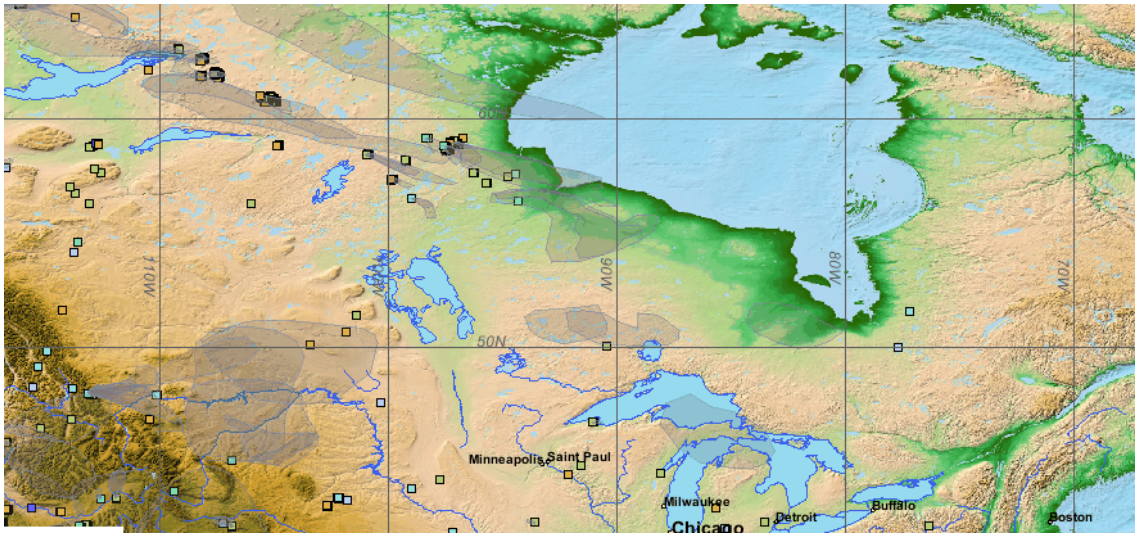

Figure 4.19 Fire locations identified by MODIS, AVHRR, and GOES during July 5-7, 2007. Analyzes smoke is shaded. Plot generated by National Geophysical Data Center (NGDC) at National Oceanic and Atmospheric Administration (NOAA): http://map.ngdc.noaa.gov/website/firedetects/viewer.htm.

TES is an infrared spectrometer and has greater sensitivity to boundary layer O_3 than the ultraviolet OMI spectrometer. Boundary layer smoke plumes from the Canadian forest fires are sampled better by the TES instrument. Therefore at least a portion of the 30 ppbv TES - OMI bias on July 7 is likely due to O_3 with a forest fire source. On July 11, both TES and OMI measure O_3 tropospheric column increase ahead of the approaching warm front, but some of the maxima are not co-located. Even after adjusting TES O_3 amounts for their assumed 3-7 ppbv high bias, TES VMR in the continental pollutant outflow region remain above 70 ppbv.

4.5.3 Source of high TES and OMI ozone distribution

The NOAA HYSPLIT model [*Draxler and Rolph*, 2003] was run with NCAR/NCEP 2.5° x 2.5° global reanalysis meteorological data to analyze the source of high ozone air (observed by TES and OMI) off the coast of Delaware, Maryland, Virginia, North Carolina, and South Carolina. TES profile locations during the July 9, 2007 Step and Stare overpass were used to initialize 72-hour back trajectories. Back trajectories were run starting at 2 km, 4 km, and 7 km. TES measurements in the continental outflow region are influenced by two regimes of back trajectories: 1) northwesterly wind that passes over the Great Lakes into the Mid-Atlantic region and 2) westerly wind from Louisiana and Florida. Both regimes are influenced by a combination of boundary layer pollution and lightning.

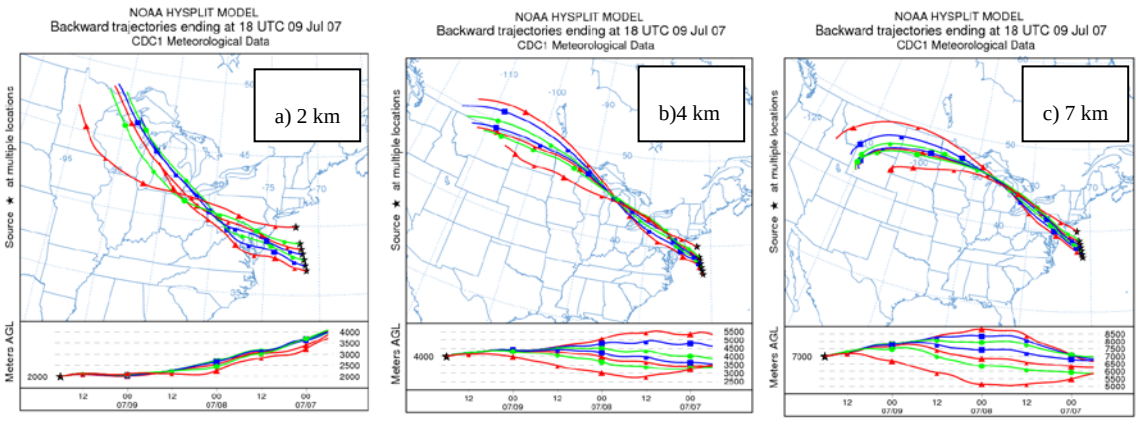

Figure 4.20 NOAA HYSPLIT back trajectories starting at 2 km, 4km, and 7 km from TES observations on July 9, 2007 18 UTC for Regime 1.

Figure 4.20 shows the results for three levels in the lower and middle troposphere for regime 1. TES tropospheric column ozone in this area peaked at 64 DU. The air mass has slowly passed over the Delaware, Maryland, and Virginia region within the previous 24 hours at a fairly constant altitude of 2 km. The

boundary layer in the model extends up to 2500 m in the late afternoon on July 8, 2007 at the time of the calculated back trajectories in the region. The air mass picked up the boundary layer pollution along its path. During the preceding 48 hours the air mass moved quickly over Lake Michigan and Lake Superior. For all altitudes the air mass passed over the same region: the Great Lakes, the Ohio River Valley into the Mid-Atlantic region. Analysis of NLDN lightning maps showed that regime 1 back trajectories were also affected by lightning-induced nitrogen oxides. Regime 1 back trajectories started at 4 km and 7 km passed through a storm over Lake Michigan (discussed in section 4.5.1.3) at an altitude of 3.5 – 8.5 km at about 12 UTC on July 8, 2007.

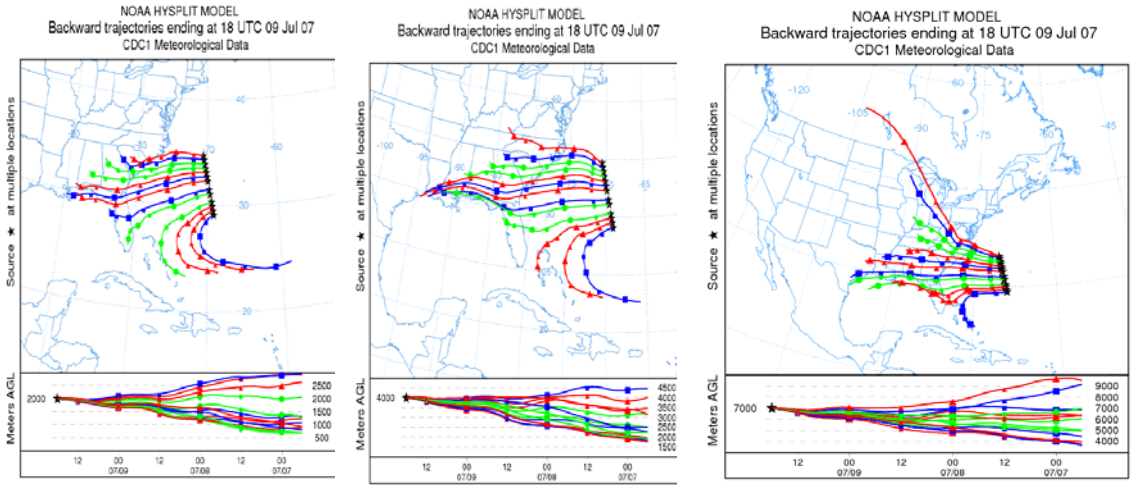

Figure 4.21 NOAA HYSPLIT back trajectories starting at 2 km, 4km, and 7 km from TES observations on July 9, 2007 18 UTC for Regime 2.

TES tropospheric column ozone for regime 2 reached a maximum of 61 DU. According to back trajectories starting at 2 km for this regime (Figure 4.21), the slow moving air mass passed over coastal North Carolina, South Carolina, and Georgia on

July 7, 2007, picking up surface pollution as reported by AQS ground stations. NLDN lightning maps showed that regime 2 back trajectories were also influenced by LNO_x (discussed in section 4.5.1.3). Regime 2 back trajectories started at 4 km and 7 km passed through a storm over Georgia and parts of South Carolina at an altitude of 5 – 6.5 km at about 18-23 UTC on July 8, 2007. Cloud-to-ground flash rates of 10-50 flashes/hr were observed during this 4-6 hr long storm.

Following convection, a large percentage of lightning-induced NO_x remains in the middle and upper troposphere [*Ott et al.*, 2010], where the lifetime of NO_x is longer and photochemical production of ozone is more efficient [*Wu et al.*, 2007] than in the boundary layer. GEOS-Chem simulated sensitivity of tropospheric O_3 columns to lightning NO_x emissions were on the order of 8-10 DU over the pollutant outflow region off the coast of Georgia and South Carolina [*Martin et al.*, 2007]. The LNO_x contribution to regimes 1 and 2 was only about 1-2 DU, due to the long travel time and mixing of the lightning affected air masses. A combination of lightning-induced nitrogen oxides and boundary layer pollution contributed to the TES reported TCO in regimes 1 and 2 over the western North Atlantic Ocean.

4.5.4 O_3-CO over the outflow region

O_3-CO correlations can give insight into the source of an increase in O_3 and CO pollutants in the plume sampled by the TES instrument. Figure 4.22 shows TES O_3-CO scatter plot for three Step and Stare overpasses within the pollutant outflow region (30°N – 40°N) during July 7-11, 2007. Only observations from surface to 600hPa are used to exclude the influence of stratospheric intrusions at the tropopause interface. A linear regression line is calculated using the reduced major axis (RMA)

method [*Hirsch and Gilroy*, 1984], where the slope ($\Delta O_3/\Delta CO$) represents the O_3-CO enhancement ratio. For the analyzed overpasses, TES O_3 and CO show a positive enhancement ratio of 0.51 mol/mol and a weak correlation coefficient R=0.3. Enhancement ratio and correlation coefficient calculated for P > 800 hPa and 600 < P < 800 hPa separately are $\Delta O_3/\Delta CO$ =0.57, R=0.54 and $\Delta O_3/\Delta CO$ =0.53, R=0.22, respectively.

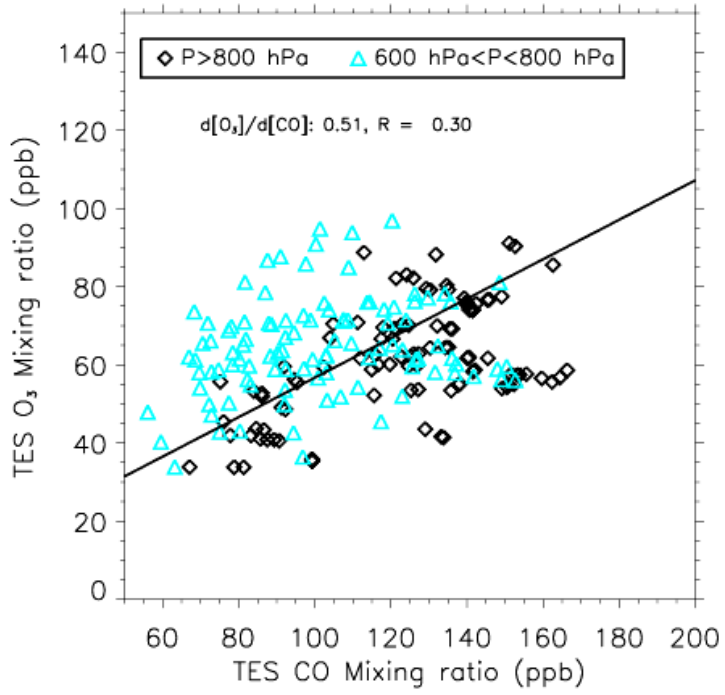

Figure 4.22 TES CO-O_3 relationship at P > 800 hPa (black diamonds) and 600-800 hPa (blue triangles) during July 7, 9, and 11, 2007 Step and Stare observations over the western Atlantic ocean (20°N – 40°N). RMA regression line is shown for all data points.

Higher enhancement ratio and correlation are expected in the surface to 800 hPa layer where fresh CO and O_3 pollution are found. The slope is within the range of previous works analyzing summertime *in situ* and satellite observations over the Eastern U.S. Slopes derived from July-August 2004 International Consortium on Atmospheric Transport and Transformation (ICARTT) campaigns are 0.31-0.44 mol/mol with

R=0.5-0.67 [*Fehsenfeld et al.,* 2006*; Singh et al.,* 2006]. *Zhang et al.* [2006] reported enhancement ratios of 0.72 mol/mol and R=0.34 for ICARTT observations in a smaller domain (30°N-40°N, 70°W-80°W, 600-650 hPa) after excluding fresh pollution plumes and stratospheric influence. With the same approach, *Zhang et al.* [2006] derived a TES $\Delta O_3/\Delta CO$ ratio of 0.81 mol/mol and R = 0.53. Without filtering out fresh plumes and stratospheric component, the ratio decreased to 0.55 mol/mol. *Hegarty et al.* [2009] computed a ratio of 0.15-0.23 mol/mol for TES summertime 2004-2006 measurements over the western North Atlantic.

A higher $\Delta O_3/\Delta CO$ enhancement ratio is expected due to ozone production in the free troposphere from exported NO_y species [*Honrath et al.,* 2004] As was shown in section 4.5.2.2, TES captured some of the CO variability over the pollutant outflow region, where enhanced O_3 was observed. Also in section 4.5.3 I showed the contribution of lightning-induced O_3 to the TES TCO columns sampled on July 9. The high ratio and low correlation are also indicative of a mixture of natural and anthropogenic sources in the sampled plume.

Lightning-induced O_3 contributes to a higher enhancement ratio and a low correlation coefficient. However, due to differences in instrument vertical sensitivities care must be taken in comparing satellite derived enhancement ratios with *in situ* ratios in previous studies. A limitation of this comparison is that only three Aura Step and Stare overpasses are available during the course of the July 7-11, 2007 Mid-Atlantic smog event. Analysis of a larger number of profiles could yield better statistical comparison.

4.6 *Conclusions*

I used a regional model to simulate continental pollution outflow during a severe July 2007 smog event in the eastern U.S. TES, OMI, and OMI/MLS satellite instruments and WRF/Chem (constrained with lightning emissions) detect the greatest TCO values over the western North Atlantic Ocean. The model representation of NO_2 and O_3 tropospheric columns improved with the addition of lightning-NO_x. In the LNO_x sensitivity run, tropospheric NO_2 column increased by 4-10 x 10^{15} molecules/cm^2, tropospheric column ozone was enhanced 6-10 DU and surface O_3 was enhanced 4-8 ppbv in areas downwind of convective events within pollutant outflow region. Comparison with standard OMI tropospheric NO_2 column product confirmed the WRF/Chem NO_2 enhancements in the vicinity of convective storms.

Upper level winds and convection ahead of a passing cold-front at the end of the smog event exported a large amount of anthropogenic and natural O_3 and NO_x from the continent over the western North Atlantic. O_3 enhancements in profiles over ocean are not seen in the *a priori*, suggesting that satellites are detecting ozone with possible sources from surface pollution and lightning NO_x. HYSPLIT back trajectories associated with high TES and OMI TCO over western North Atlantic Ocean were influenced by a combination of boundary layer pollution and lightning-induced O_3. In one regime, back trajectories from TES retrievals passed over the Baltimore-Washington metropolitan area and the Great Lakes region within the preceding 72 hours. Another regime was influenced by transport of polluted air mass off the coast of Georgia, North Carolina and South Carolina. Both regimes

encountered lightning activity. Calculated TES O_3-CO correlations over the western Northern Atlantic region yielded a high $\Delta O_3/\Delta CO$ enhancement ratio of 0.51 mol/mol and a weak correlation coefficient R=0.3. Contribution of lightning-induced O_3 to high TES TCO explain low correlation with surface CO and high enhancement ratio.

Finally, I used WRF/Chem to investigate the signature of pollution in the lower troposphere and link the satellite retrieved increased tropospheric column ozone with the smog event. I applied the TES and OMI averaging kernels to WRF/Chem for better analysis of the two satellite instruments with different vertical sensitivity. Mean difference between the TES and OMI instruments is 3.07 ppbv over ocean and 7.54 ppbv over land. In general, TES has a higher bias than OMI with respect to *in situ* measurements. Here higher average TES land retrievals than OMI are also explained by sampling an aged air mass from boreal forest fires in Manitoba on July 7 and differences in sampling outflow ahead of approaching warm front in a mid-latitude cyclone on July 11.

I used OMI and TES retrievals to map outflow of eastern U.S. pollution during a severe smog event and showed that natural and anthropogenic sources contribute to high TCO in retrieved pollutant outflow plumes. The OMI/MLS TCO product did not capture the high distribution of O_3 in this event; but the OMI product, TES and the model show a large maximum off the U.S. East Coast. In view of the proposed satellite geostationary missions to monitor air quality, better temporal and spatial data availability will contribute to better statistical analysis of pollutant plumes on a regional scale.

Chapter 5 Open convection cells and their role in the redistribution of tropospheric ozone: WMONEX O_3 observations

5.1 *Introduction*

Winter Monsoon Experiment (WMONEX) 1978/1979 was an international atmospheric–oceanic experiment over the Western Pacific Ocean focusing on the global and regional aspects of the winter monsoon circulation over East Asia and Australia [*Greenfield and Krishnamurti*, 1979]. This campaign included research aircraft, ships, soundings, radar, and surface stations – all deployed to study the circulation features of the winter monsoon. Some of the major scientific findings during this campaign were characterization of the structure and dynamics of cold surges over the South China Sea and interaction with planetary-scale circulations. A regular diurnal convection cycle was described off the coast of Borneo with convection developing over land in the late afternoon and new convection forming offshore at midnight. *Houze et al* [1981] characterized the development of this off shore convection into a mature mesoscale system in the early morning hours. This mesoscale system dissipated typically at midday. Here, I present the WMONEX O_3 measurements taken aboard the NCAR Electra as it flew over the Western Pacific through the remnant of one of these dissipated storms. The WMONEX ozone data have not been published prior to this study.

Convective cloud observations from first satellites revealed cellular cloud patterns not discernable from Earth's surface. The so-called mesoscale cellular convection (MCC) pattern is an organized array of three-dimensional polygonal open or closed

cells over vast regions of oceans [*Hubert*, 1966]. Open cell circulation (Figure 5.1 and Figure 5.2a) has downward motion and clear sky in the center, and is surrounded by cloud associated with upward motion [*Atkinson and Zhang*, 1996].

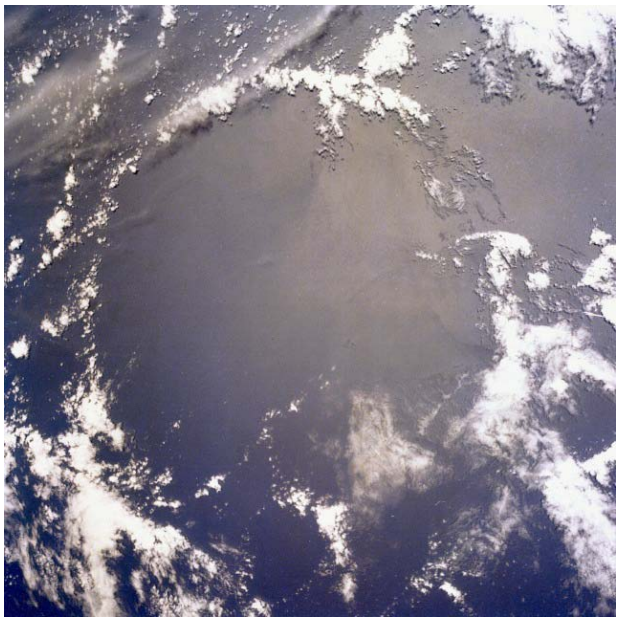

Figure 5.1 Convective cloud ring over the Southern Pacific Ocean. Image STS 032-097-006 courtesy of Earth Sciences & Image Analysis Laboratory, NASA Johnson Space Center (http://eol.jsc.nasa.gov)

Closed cells have the opposite circulation (Figure 5.2b). Warm air is rising in the center, and sinking around the edges, so clouds appear in cell centers, but evaporate around cell edge.

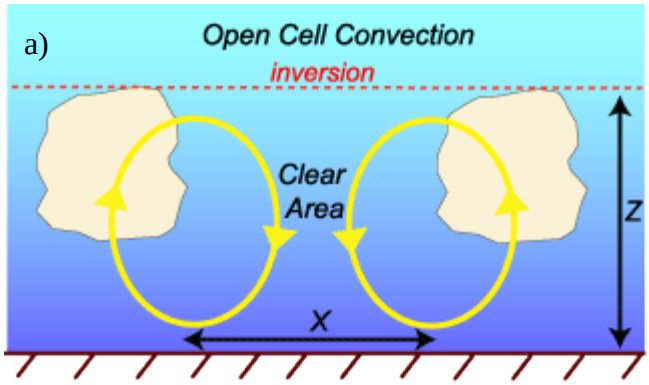

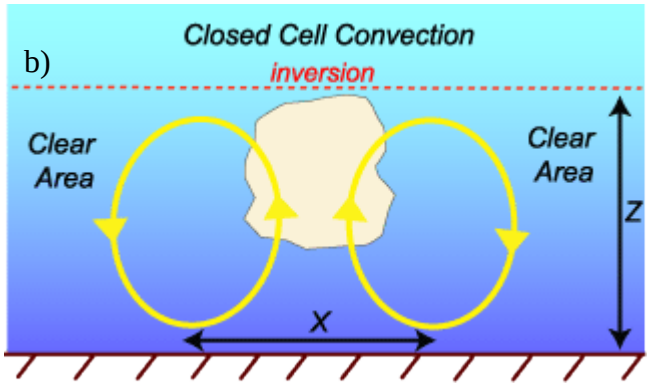

Figure 5.2 a) Open and b) closed cell mesoscale cellular convection. Figure adapted from http://apollo.lsc.vsc.edu/classes/met455/notes/section9/1.html.

In highly convective regions, open cells occur over areas with significant air-sea temperature difference, while closed cells form over regions with weak air-sea temperature gradient. Open cells frequently occur within cold-air outbreaks (CAO), when cold, dry air from continents is advected over a warmer ocean surface [*Atkinson and Zhang*, 1996]. For open cell and closed cell convection aspect ratios of horizontal scale, *x*, to vertical scale, *z*, are:

Open Cell: $\frac{x}{z} = \frac{15}{1}$ and Closed Cell: $\frac{x}{z} = \frac{30}{1}$

While there is little in reviewed literature on the dynamics of concentric cloud formation, such cloud rings are an example of open convection where a broad downwelling region is surrounded by thin regions of ascent [e.g., *Helfand and Kalnay*, 1983]. Evidence from previous studies suggests that cloud rings are the remains of collapsed thunderstorms: forming and decaying convective clouds [*Loranger*, 1974]. All cloud ring events were noted in tropical, marine environments (Figure 5.3).

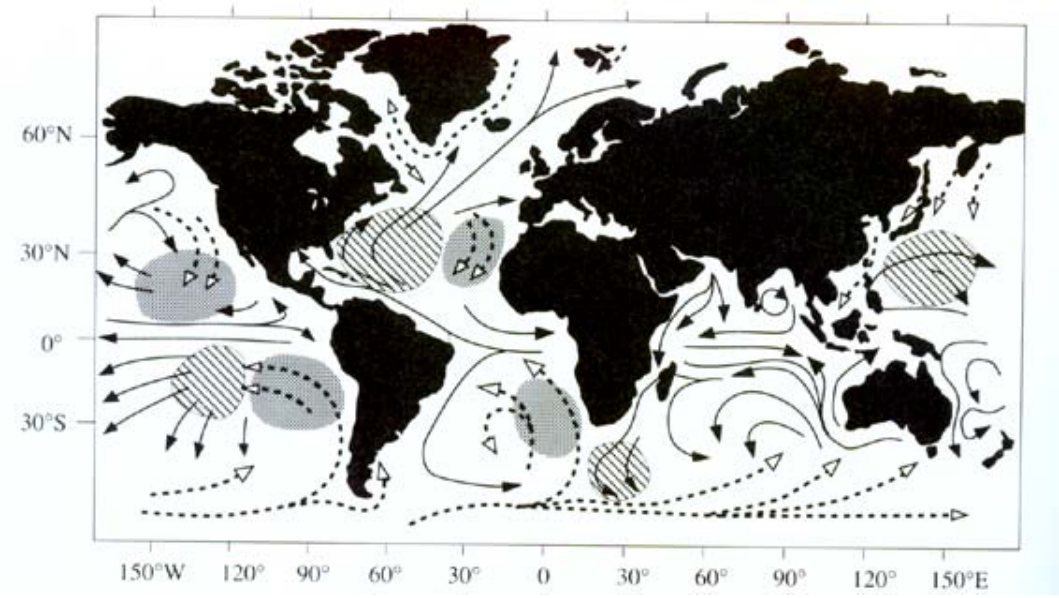

Figure 5.3 Global climatology of cellular convective clouds over oceans. Hatched areas are regions where open convection cells predominate. Shaded areas are regions where closed cells are more common. Dashed streamlines show cold currents; solid streamlines show warm currents. Adapted from [*Agee et al.*, 1973].

The abundance of warm, moist, and unstable air parcels in marine environments facilitates thunderstorm formation. As the convective cloud reaches its mature stage, strong updrafts develop. Radiative and evaporative cooling in the cloud top can cause precipitation and downdrafts. If there is weak vertical wind shear, the thunderstorm is upright and the rainy downdraft undercuts the updrafts. Falling precipitation suppresses rising air drafts by frictional drag, and the storm begins to dissipate or collapse. The subsiding air may combine with ascending surface air and form convective clouds around the collapsing thunderstorm. The formed cloud ring is characterized by ascending air in the convective walls and subsiding air in the central clear region. *Ruprecht et al.* [1973] found that the equivalent potential temperature, a measure of internal energy and moisture content of an air parcel, decreased within the cloud ring and increased within the cloud walls. The reduced equivalent potential

temperature inside the ring can be explained by the subsidence of dry air from aloft. Likewise, an increase in potential temperature inside cloud walls is due to upward convection of moist, marine air. In this chapter, I examine these properties using the first *in situ* ozone measurements within the cloud ring.

5.2 *Background*

Convection associated with thunderstorms is an important mechanism of tropospheric air transport. Rapid convective updrafts redistribute trace gases within the troposphere [*Chatfield and Crutzen*, 1984; *Dickerson et al*., 1987]. Likewise, synoptic-scale frontal systems transport air downwards from the upper troposphere [*Luke et al*., 1992]. In the marine boundary layer ozone photochemical lifetime is less than a week, increasing with height to 1 month at 6 km and 1 year at 10 km [e.g., *Kley et al.*, 1996]. Consequentially, lifetime of lower tropospheric ozone is enhanced by the upward convective transport. On the other hand, lifetime of upper tropospheric ozone decreases as it is transported to the lower troposphere where it is more efficiently destroyed [*Lelieveld and Crutzen*, 1994]. *Lawrence et al*. [2004] used a global model to show that convection shortens the lifetime of ozone in marine environments but lengthens it over continents for a net impact of increasing the lifetime and burden of tropospheric ozone. In this chapter I provide observations of these model predictions.

Tropospheric ozone is destroyed by photochemical reactions in unpolluted air. The photochemistry of O_3 in the troposphere is initiated by photolysis of O_3 at wavelengths less than 340 nm [*Levy*, 1971]:

(R1) $O_3 + h\nu \rightarrow O(^1D) + O_2 \quad (\lambda < 340 \text{ nm})$

The highly reactive excited atomic oxygen, $O(^1D)$, reacts with the gas phase H_2O to generate tropospheric OH radicals:

(R2) $O(^1D) + H_2O \rightarrow 2OH$

Reactions R1 and R2 are a primary source of tropospheric OH radicals and removal of O_3. The OH species can undergo further reactions, contributing to ozone destruction:

(R3) $OH + O_3 \rightarrow HO_2 + O_2$

(R4) $HO_2 + O_3 \rightarrow 2O_2 + OH$

(R5) $HO_2 + HO_2 \rightarrow H_2O_2 + O_2$

In addition, halogens, particularly bromine in sea salt, can destroy tropospheric ozone catalytically [e.g., *Vogt et al*., 1996; *Dickerson et al*., 1999]:

(R6) $Br + O_3 \rightarrow BrO + O_2$

(R7) $BrO + HO_2 \rightarrow HOBr + O_2$

(R8) $HOBr + h\nu \rightarrow OH + Br$

The marine boundary layer is characterized by a local maximum in H_2O and sea-salt Br, and undergoes rapid photochemical destruction of ozone by reactions R1-R8. In polluted environments oxides of nitrogen lead to ozone production:

(R9) $HO_2 + NO \rightarrow NO_2 + OH$

(R10) $NO_2 + h\nu \rightarrow O + NO$

(R11) $O + O_2 + M \rightarrow O_3 + M$

Emissions from East Asia have been detected thousands of kilometers downwind both on the west and the east coast of North America [e.g. *Jaffe et al*., 2003]. Asian pollution plumes enhance high pollution episodes and increase

"background" concentrations making it more difficult to comply with National Ambient Air Quality Standards (NAAQS). Surface ozone in the western U.S. in April-May is on average enhanced by 3-6 ppbv as a result of Asian anthropogenic emissions [*Yienger et al.*, 2000]. Similarly, *Fiore et al.* [2002] showed that anthropogenic emissions in Asia and Europe contribute to an increase in summer time afternoon ozone concentrations in surface air over the conterminous United States by about 4-7 ppbv. As East Asia continues to grow economically and its emissions continue to increase, there is a need to better understand mechanisms for export of Asian pollution to the global atmosphere. Because ozone is central to the chemistry of the atmosphere and is itself a greenhouse gas, evidence of long-term trends in tropospheric ozone would be useful for quantifying climate change. The data from the 1978-1979 WMONEX, a sample of which is presented here, could offer a useful benchmark for comparison with future observations.

5.3 *Observations*

This study uses NCAR Electra aircraft data from Winter Monsoon Experiment (WMONEX) based in Malaysia between November 17, 1978 and January 9, 1979. This campaign included flights over the Pacific Ocean and South China Sea (Figure 5.4).

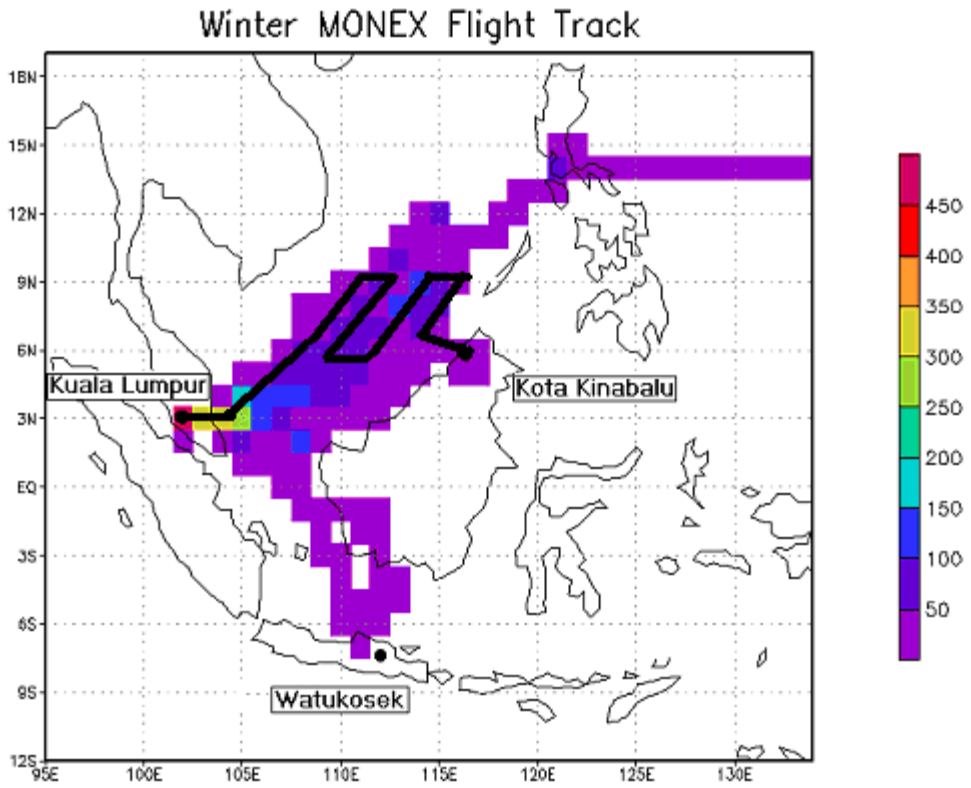

Figure 5.4 Collection of available measurements for all WMONEX flights. Scale (minutes within 1° x 1° grid) at lower right. The bold black line depicts the December 29, 1978 flight track when several cloud rings were penetrated.

A number of variables were measured from the NCAR Electra as it flew over the Western Pacific. After successfully converting the archived data from an archaic GENPRO-I data format into a readable one the ozone data are analyzed and published for the first time here. Figure 5.5 is a plot of average ozone mixing ratios over the South China during WMONEX. The tropical, marine lower troposphere is characterized by low ozone concentrations; here averaged 40.2 ppbv.

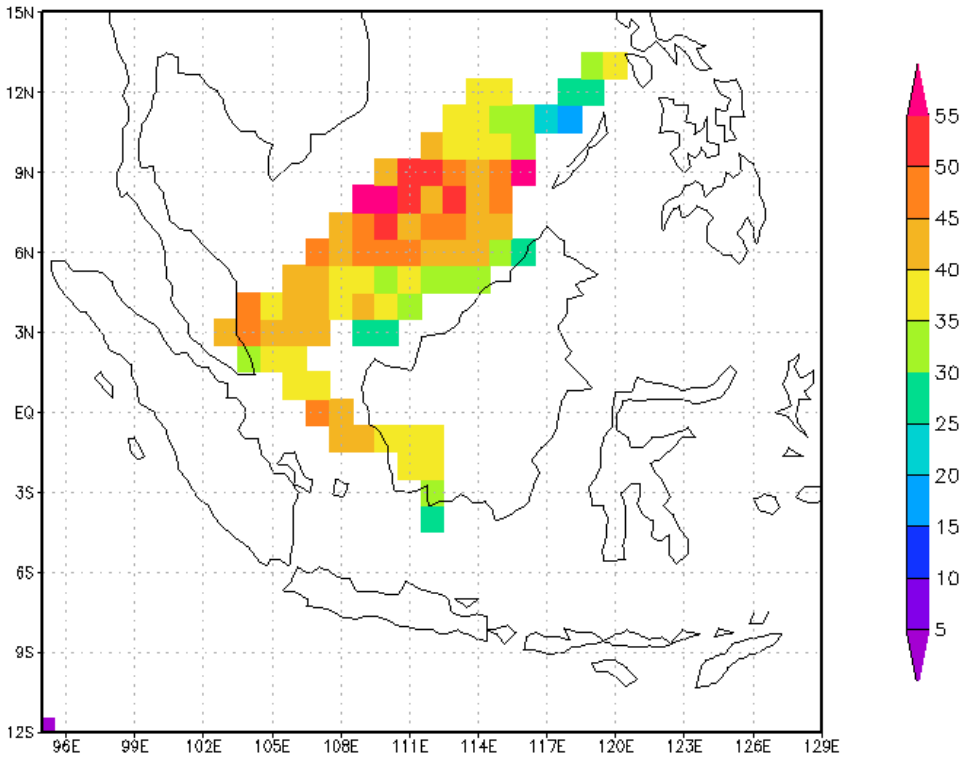

Figure 5.5. Average ozone mixing ratios (ppbv) over the South China Sea measured at cruise altitude 5.5 km – 6.5 km.

The ozone mixing ratio measurements taken during the WMONEX 1978 mission provide a benchmark to test for trends in the composition of the atmosphere, and thus climate forcing, over the western Pacific – an area surrounded by countries that have been developing rapidly in the intervening decades. Direct comparison of these observations to more recent data for the same Southern Oxidation Index (SOI) is impossible, since no field campaigns have examined the chemical composition of air over the South China Sea in December since WMONEX,

I concentrated on the flight with several documented occurrences and penetrations of ring clouds. Cloud rings were visually identified during the December 29, 1978 flight by observers on the aircraft and later from time-lapse 16 mm films. During this flight, the aircraft flew at a cruising altitude of 6 km from

Kuala Lumpur (3°N, 101°E) to Kota Kinabalu (5°N, 116°E) in East Malaysia, crossing the South China Sea. The tropopause height was about 19 km during WMONEX flights.

5.4 *Ozone Loss during Measurement*

During WMONEX flights, ozone was sampled directly from the ventilation system of the Electra aircraft, supplied by the engine compressors; passage through the compressors resulted in a loss of ozone. Comparisons of ozone measured directly in ambient air to air that has passed through engine compression systems [e.g. *Prados et al*., 1999] typically show that about 5 % of the ozone is destroyed by surface deposition.

Average Ambient O_3 (ppbv)	Average Cabin O_3 (ppbv)
40.4	26.0
41.4	29.2
36.2	25.9
35.2	24.8
33.2	22.2
29.1	19.7
27.3	20.8
33.0	17.5
31.5	21.3
26.7	17.2
20.2	16.9

Table 5.1 Average ambient O_3 and average cabin O_3 measured aboard NOAA's P3 on August 29, 2008.

The loss of ozone within air compressors inside of NOAA's P3 (same as NCAR Electra) aircraft was tested during a hurricane Gustav research flight from

Florida to Cuba on August 29, 2008. The TECO ozone analyzer was set up to manually switch between sampling ambient air and cabin air every 5-10 seconds. Cabin and ambient measurements were averaged to represent the same altitude (Table 5.1). Figure 5.6 shows the ratio between average inside and outside O_3 as sampled by TECO; R^2 is 0.75. The average ratio of cabin sampled ozone to ambient sampled ozone is 0.57±0.24 with a confidence interval of 95%. The confidence interval is computed using $= t(\alpha, df) \times S_b$, where *t* is the critical value of the *t* statistic and S_b is the standard error in the slope. All WMONEX O_3 plots are adjusted for the 0.57 ratio.

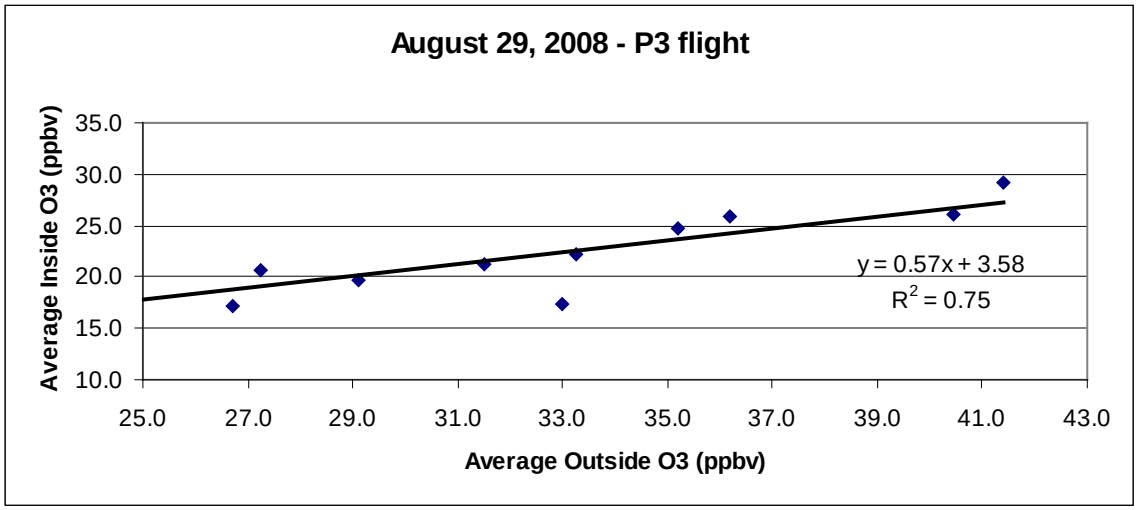

Figure 5.6 Loss of O_3 within air compressors inside of P3 aircraft.

Since WMONEX O_3 measurements are the average cabin O_3 mixing ratios, relationship shown in Figure 5.6 can be used to adjust 1978/1979 measurements for comparisons with future field campaigns over Indonesia or modeling studies. These O_3 observations are useful for characterizing lower tropospheric chemical and mesoscale processes during the winter monsoon, as discussed in the next section.

5.5 *Results*

A Dasibi ultraviolet absorption sensor monitored ozone mixing ratios during the flight (Figure 5.7). Although the average background ozone for this flight was around 30 ppbv, significant signal increases were noted throughout the flight. While the 12:00 LST peak has been identified as a cyclone [*Bolhofer et al*., 1981] from the mainland of Asia which brought with it both polluted continental outflow and dry, descending stratospheric air, all other signal peaks are postulated to correspond to cloud rings.

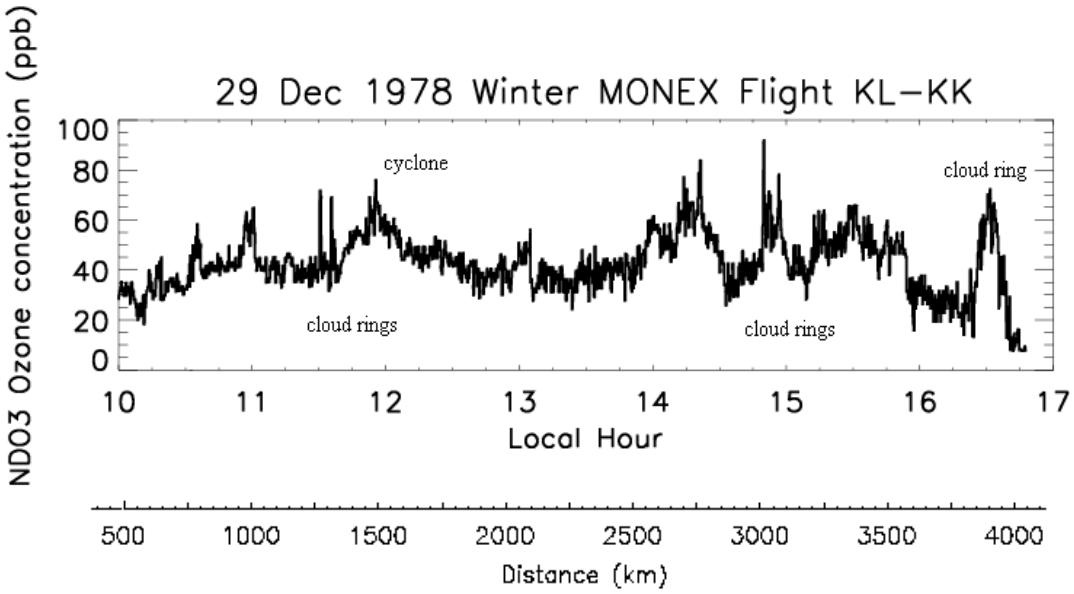

Figure 5.7 Ozone mixing ratio series with respect to distance and local time for part of the December 29, 1978 flight. Distance is measured as traversed flight path from Kuala Lumpur. Flight start time 00:41 UTC (8:41 LST) and end time 8:48 UTC (16:48 LST). Flight altitude was nearly constant at ~6 km until descent for landing, starting at 16:20 LST, 3810 km from Kuala Lumpur. Largest cloud ring is about 50-100 km in diameter, smallest are about 10 km.

At 11:40 LST there are two signal peaks, each of about 72 ppbv, measuring about 10 km and 20 km in covered distance. Similar spikes were recorded at 14:50 LST, 78 ppbv mixing ratio was measured within a 10 km stretch and 96 ppbv within 20 km. Ozone mixing ratios of 70-80 ppbv were also recorded at 11:00 LST and 14:20 LST.

The longest in duration ozone local maximum was at 16:30 LST with mixing ratio of 75 ppbv within a 50-100 km width. All of these ozone mixing ratio spikes are postulated to correspond to clear regions within cloud rings with subsiding ozone-rich upper tropospheric air, transporting ozone downward. The validity of this conclusion depends on the characteristics of ozone mixing ratio in a pristine, marine environment.

The vertical ozone distribution in the clean, tropical troposphere is typified by the electrochemical concentration cell (ECC) ozonesonde observations made at American Samoa, South Pacific (14°S, 170°W) from April 1986 – May 1990. Average seasonal vertical ozone distribution for December, January, February months was assessed using 26 profiles. For the 500 hPa to 300 hPa pressure levels, corresponding to the WMONEX cruising altitude, the mean ozone mixing ratio was 33 ppbv and 32 ppbv respectively [*Komhyr*, 1992]. Similarly, average ratios of 34 ppbv were observed for December – March 1998-2002 period at Watukosek, Java (7.5°S, 112.7°E), one of the sites of Southern Hemisphere Additional Ozonesondes project [*Thompson et al*., 2003]. Average WMONEX ozone mixing ratio at an altitude of 6 km over the South China Sea was 40.2 ppbv (after applying correction for loss of ozone in air compressors). In general, over equatorial oceans, ozone destruction by reactions R1 and R2 is enhanced by high levels of ultraviolet radiation and high humidity. Ozone mixing ratios of 70-80 ppbv are rarely observed in the tropical, marine boundary layer.

The last peak in ozone time series (see Figure 5.8a) was analyzed using shortwave irradiance data, measured during the flight (Figure 5.8b).

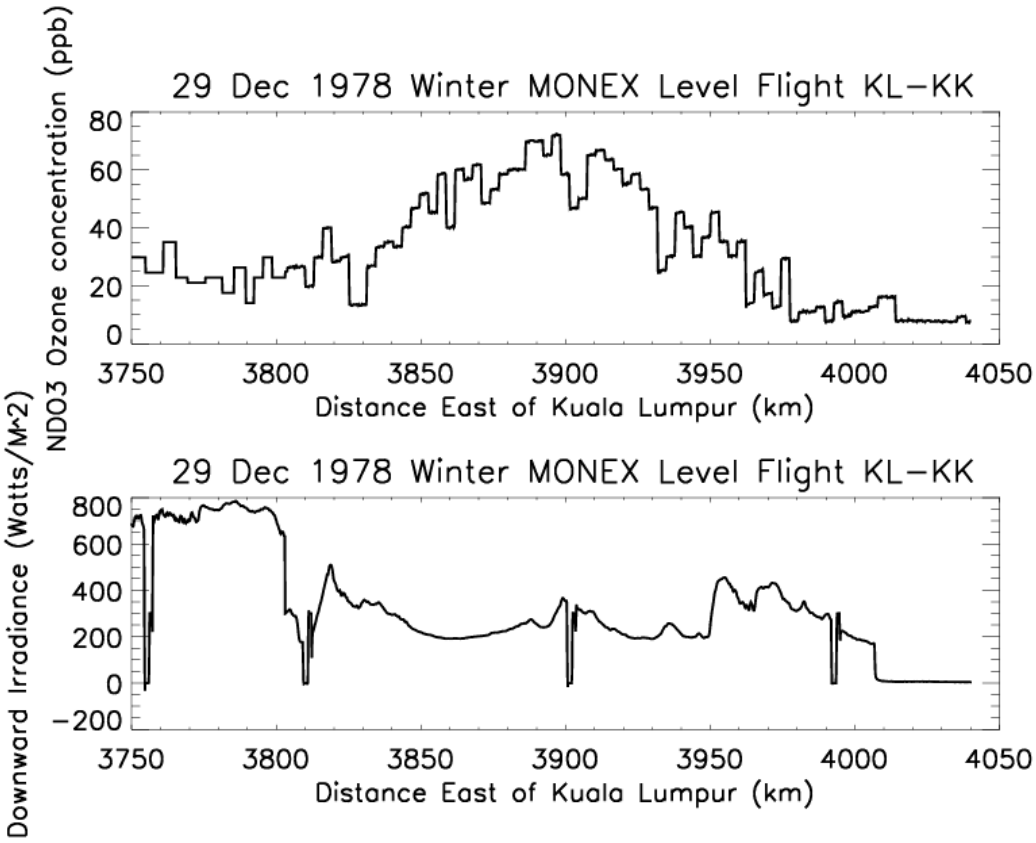

Figure 5.8 (a) Blow up of ozone mixing ratios observed on December 29, 1978 in a cloud ring penetrated as the aircraft descended into Kota Kinabalu. X-axis is the distance from Kuala Lumpur; approximate altitude shown below distance. (b) Same as (a) but for downward shortwave radiation; the instrument automatically zeros every 600 seconds. Irradiance reaches a local maximum around 3900 km from Kuala Lumpur in the center of the cloud ring.

Reductions in downward shortwave irradiance indicate clouds above the aircraft. Irradiance is higher in clear regions, where incoming solar radiation is maximized, and lower in cloudy regions, where clouds block incoming solar radiation. The last ozone local maximum of the flight corresponds to a local maximum in the solar irradiance plot at about 3900 km from Kuala Lumpur. The irradiance local maximum is surrounded by two well-formed local minima, adjacent to the ozone peak. Simultaneous ozone and irradiance peaks can be interpreted as a clear sky region with subsiding upper-tropospheric air. The irradiance minima and

ozone mixing ratio minima on both sides of this clear region correspond to convective clouds, transporting low-ozone marine air upward. These data were collected near the end of the flight, while the aircraft was descending prior to landing. The resulting plots confirm the occurrence of cloud rings, noted visually by observers on the aircraft.

5.6 *Discussion*

The Asian winter monsoon is distinguished by cold-surges, low-level winds over the South China Sea. As the cold air moves off the China coast, there is an enhancement of moisture transport equatorward, which increases deep convective activity over the South China Sea [*Johnson and Zimmerman*, 1986]. On December 28 and 29, 1978 a rapid-moving cold surge moved off the coast of south China and spread southward. Cold surges over the warm ocean should be conducive to open convection [*Helfand and Kalnay,* 1983]. Convective activity increased in the central part of the South China Sea and cyclonic circulation intensified in the region of the December 29 flight [*Bolhofer et al*., 1981]. *Houze et al.* [1981] discovered that convection in this region underwent an extremely regular diurnal cycle. The cycle of convection began at midnight when an off shore low-level wind began (Figure 5.9). Convergence of this wind and monsoonal northeasterly flow just off the east coast of Borneo resulted in formation of convective cells. The system dissipated at midday, when the offshore wind became onshore wind and convergence concentrated over land.

Throughout the flight, winds were on the order of 2 -10 m/s with a vertical shear less than 8 m/s between the surface and 6 km altitude. According to the

collapsed thunderstorm hypothesis, convection and minimal vertical wind shear are conductive to cloud ring formation [*Loranger*, 1994]. The cloud rings witnessed during the December 29 flight could have indeed been formed by collapsing thunderstorms.

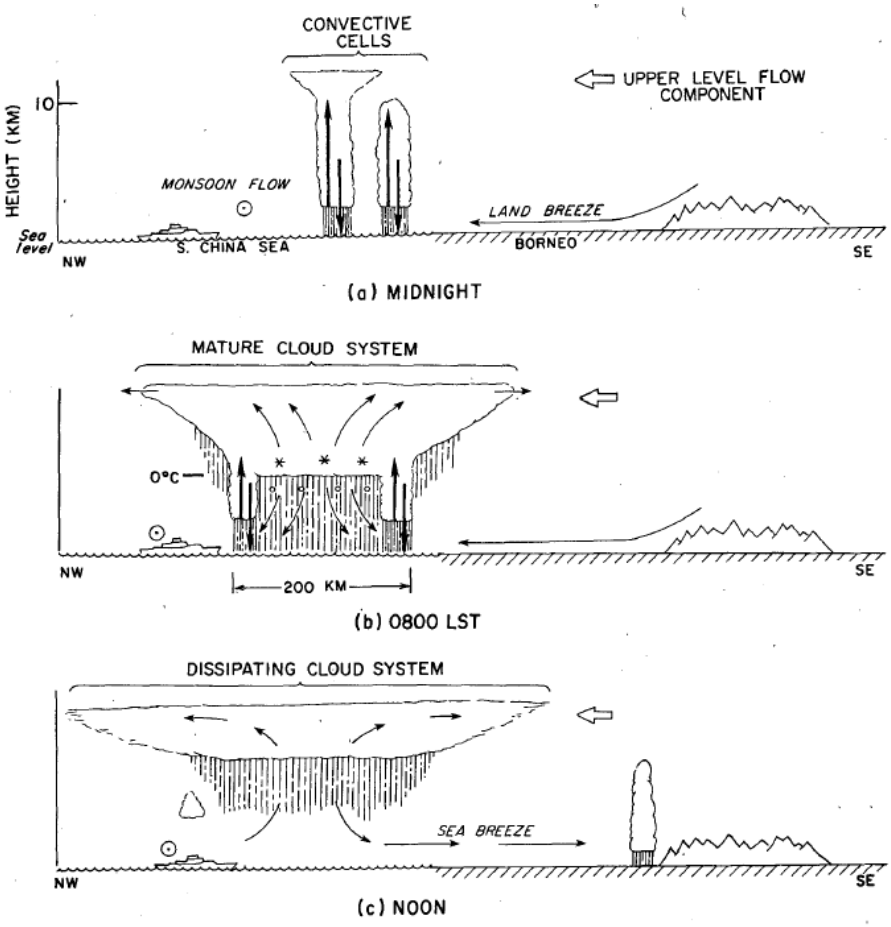

Figure 5.9 Schematic of the development of diurnal mesoscale precipitation system off the coast of Borneo. Adapted from [*Houze et al*, 1981].

The origin of ozone enhanced air within the cloud rings must be examined. According to the collapsed thunderstorm hypothesis, the developed thunderstorm at its mature stage entrains air parcels with higher ozone concentration from the upper troposphere. As the thunderstorm decays, the ozone rich air descends within the cloud ring, exiting at the cloud base. Observed air parcels with mixing ratios on the

order of 80-90 ppbv are probably of upper tropospheric origin. Yet, the equivalent potential temperature in the upper troposphere would have been too great in magnitude to allow air parcels to descend to the observed altitude of 6 km.

Alternatively, the high ozone mixing ratios measured in the cloud rings over the South China Sea are more likely explained by active convection over Indonesia several days before the WMONEX observations. The NCEP Reanalysis (available from http://www.cdc.noaa.gov/cdc/reanalysis/) 200 hPa wind field maps confirmed the east-west wind flow pattern over Indonesia and the South China Sea during the week prior to December 29 measurements. Upward transport and mixing of urban polluted air with upper tropospheric air, NO production by lightning, followed by photochemical ozone production during westward transport, could have provided sufficiently large ozone mixing ratios to the 10-12 km altitude region over the South China Sea. The collapsed thunderstorm could have then entrained this enhanced ozone and brought it down to 6 km. According to the World Fire Atlas provided by European Space Agency (available at http://shark1.esrin.esa.it/ionia/FIRE) December is not a biomass-burning month in Indonesia. Therefore, biomass-burning pollution is not a likely contributor. Observations from the BIBLE-A experiment showed that during transport from the tropical Pacific Ocean to Western Indonesia, which takes about 2.6 days in the upper troposphere, the ozone mixing ratio of an air mass increased. With median NO of about 100 pptv, *Kita et al*. [2003] estimated median O_3 production of 2.1 ppbv/day in the transported air mass. Moreover, during BIBLE-A experiment most air masses encountered cumulus clouds within 24-48 hours prior to observation [*Kita et al*., 2003]. The ozone mixing ratio increase in BIBLE-A is

due to the mixing of upper tropospheric air with convectively lifted polluted, urban air and NO production by lightning. The same transport and mixing mechanism would have influenced the air masses observed during WMONEX. I investigated the increase in ozone mixing ratio due to lightning produced NO to explain the WMONEX observations.

I used a three-dimensional cloud-scale chemical transport model (CSCTM) developed by the University of Maryland Atmospheric Chemistry Group to approximate the net ozone production due to lightning NO in a convective cloud [*DeCaria*, 2000]. The model was initialized by profiles of O_3, NO, NO_2, CO, and 4 species of hydrocarbons including isoprene. These profiles were chosen to represent relatively clean tropical conditions with a lightning NO_x signal of 500 pptv superimposed in the upper troposphere. According to the NASA's Lightning Imaging Sensor (LIS) data (available at http://thunder.nsstc.nasa.gov) there is higher lightning frequency over Indonesian islands in December, the beginning of the local wet season, than in September. So the NO mixing ratios used in the model were higher than those observed during the Bible-A study in the months of September and October. Daily ozone profiles for 8 days after the modeled lightning episode are illustrated in Figure 5.10.

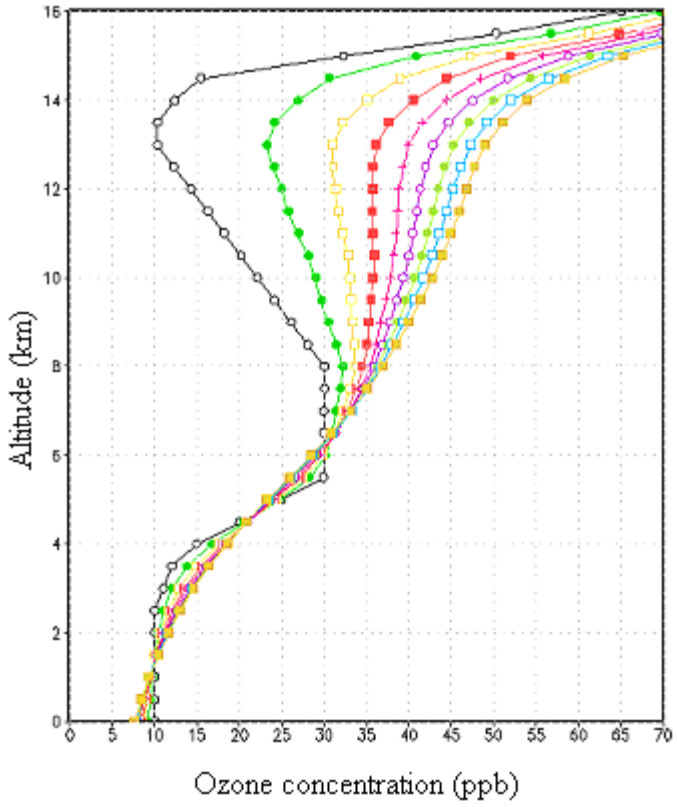

Figure 5.10 Daily ozone production for 8 days following the modeled lightning episode. The left-most profile is the initialization profile.

Most ozone production takes place in the upper-tropospheric layers, where NO was produced by lightning. Above 10 km, 7-14 ppbv O_3 were produced within first day after lightning, 4-8 ppbv O_3 within second day, and 3-5 ppbv O_3 within third day. Ozone production aloft continued at smaller rates after the fifth day, averaging 1-2 ppbv/day. Thus ozone production within the first 48 hours after lightning is on the order of 11 – 22 ppbv. Not only is the produced ozone not destroyed in the subsequent days, it is augmented at a small but steady rate. Therefore, with upstream lightning there could have been sufficient ozone at 8-14 km to be entrained and cause the observed ozone enhancements at 6 km in the areas of subsiding air. Thus the

upstream lightning scenario can be applied to explain the ozone peaks observed during WMONEX flights.

The proximity of the Intertropical Convergence Zone accounts for frequent lightning activity over Indonesia. The WMONEX flights took place during the wet season, time of enhanced convection in the tropics. During this season lightning occurrence at peak time of 15 LST over Indonesian islands is three times the rate of occurrence over ocean [*Hidayat and Ishii*, 1999]. Indeed, according to LIS data, there is substantial lightning activity over Indonesia in Decembers with equivalent ENSO index as in 1978. Since the easterlies carry the upper tropospheric air from the Pacific Ocean, I conjecture that the NO enhancement of air by lightning occurred over Eastern Indonesia. Within 24 – 48 hours after the lightning activity, net ozone production in the affected air mass is on the order of 11 – 22 ppbv. The easterlies carry this air mass from Eastern Indonesia to the South China Sea, with transport time of 24 – 48 hours during which the air probably subsided by 1-2 km. In the South China Sea the ozone enhanced air is entrained by developing convective clouds. Under the conditions of low vertical sheer, a convective cloud collapses, bringing air from 8 – 10 km downward. The descending air within the cloud exits the cloud base on its sides and combines with ascending lower tropospheric air, which forms the cloud ring. Ozone trends within such clouds support the postulated transport mechanisms of collapsed thunderstorms. Changes in ozone concentration during penetration of a cloud ring correspond to subsiding upper tropospheric air currents within the center of the cloud ring and upward moving lower tropospheric air within the convective cloud walls. The WMONEX ozone mixing ratios of 70-80 ppbv in the

cloud ring center could have been produced in outflow from a thunderstorm over Eastern Indonesia 2 – 3 days prior to observations. The hypothesis of cloud rings formed by collapsed thunderstorms is supported by WMONEX observations.

5.7 *Conclusions*

The ozone mixing ratio measurements taken during the Winter MONEX 1978 mission provide a benchmark to test for trends in the composition of the atmosphere, and thus climate forcing, over the western Pacific – an area surrounded by countries that have been developing rapidly in the intervening decades. The observations in cloud rings support the hypothesis that convective cloud rings result from collapsed thunderstorms. The measurements further demonstrate how convective mixing, as predicted by numerical models, can lead to vertical transport and destruction of ozone over remote, tropical, marine environments. The subsiding air channel within the cloud ring's clear region transports upper tropospheric air into the lower levels where ozone's lifetime is shorter. Though this rare cloud phenomenon only occurs in tropical, marine environments, it may offer a useful test bed where atmospheric scientists can investigate the impact of convective clouds on the composition of the atmosphere. The natural formation of convective cloud rings in tropical regions presents a beautiful display in the sky for visual enjoyment and provides novel insight into the interaction of cumulus convection and tropospheric chemistry.

Chapter 6 Conclusions

6.1 *Summary*

Summertime smog episodes are frequent in the Mid-Atlantic region. In this work, I analyzed the July 7-11, 2007 air pollution event during which 8 hour maximum ozone mixing ratios in northeastern Maryland reached 125 ppbv. This is the worst smog event in Maryland to date since the implementation of SIP Call power plant NO_x emission reduction in 22 eastern states in 2003. The meteorological setup for this smog event included a Bermuda High pressure system off the U.S. east coast, formation of midlatitude cyclone over southern Canada, clear skies, hot temperatures (~37°C), low southwesterly winds and plenty of vehicle NO_x and VOC emissions. Development of the Low Level Jet and Appalachian Leeside Trough on July 10 set up large-scale southwest flow along the eastern sea-board, transporting pollutants from the southeast U.S. to New England. Several large thunderstorm systems occurred over the eastern U.S. over the course of the smog episode, creating the potential of this regional pollution event to be exported from North America and contribute to hemispheric pollution. The smog event ended as the cold front associated with the midlatitude cyclone near James Bay pushed through the region on July 12, sweeping pollution out over the western North Atlantic Ocean.

I used a regional chemical transport model (WRF/Chem V3.1.1) with RADM2 chemical mechanism to simulate the July 7-11, 2007 smog event. In Chapter 3, I evaluated model performance against surface and ozonesonde measurements across the eastern U.S. WRF/Chem-calculated trace gases (O_3, NO_x, CO) and

meteorological parameters (T) were compared to ground observations and ozonesonde profiles. Mean bias, root mean square error and correlation coefficient (r) from WRF/Chem 8-hr O_3 maximum and AQS observations during July 6-11, 2007 were 0.59 ± 11.0 ppbv, 11.0 ppbv, and 0.7, respectively. However the low mean biases are a result of underpredicted O_3 in the northeast and overpredicted O_3 in the southeast. WRF/Chem captures mean ozone mixing ratios, but shows less variability than is observed. The model underestimated the magnitude of the 8-hr maxima observed on July 9, 2007 in the densely populated northeast. WRF/Chem has difficulty correctly representing O_3 mixing ratios in the southeast, showing a high bias of 8-11 ppbv at the peak of the smog event. Using FDDA analysis nudging increased surface ozone biases to 17.2-24.3 ppbv in the southeast U.S, highlighting the sensitivity of photochemical O_3 production to model generated meteorological fields.

Comparison at individual sites showed that the model captures the diurnal temporal and spatial variations in O_3 and passage time of the cold front. Over the course of the smog episode WRF/Chem underpredicts daytime O_3 at rural Pinnacles, NY and Great Smokies, TN sites and suburban Aldino, MD AQS site. In JST and YRK, GA sites daytime and nighttime O_3 is overpredicted. Ozone overprediction in the southeast U.S. is attributed to overpredicted temperature (>1.5°C) in the model. In a separate run, 3-D analysis nudging increased surface ozone biases by 12 ppbv in the southeast U.S. This is attributed to increased insolation and temperature in the FDDA run.

The RADM2 chemical mechanism used in this simulation does not account for NO_x lifetime-extending reservoir species: organo-nitrates and nitryl chloride. In sensitivity simulation where heterogeneous production of HNO_3 was eliminated to simulate the maximum effect of recycling of NO_x through $ClNO_2$ chemistry, daytime O_3 mean biases at Aldino, Pinnacles and Great Smokies sites were reduced by 3-5 ppbv. Another sensitivity simulation showed that low biases in O_3 dry deposition velocities contribute to insufficient nighttime depletion of O_3 at SEARCH sites and Aldino, MD.

Analysis of Beltsville ozonesondes showed that the model captures the vertical distribution of ozone up to 600 hPa. The model-simulated ozone plume extends into the 815 hPa and 730 hPa pressure layers, a portion of the troposphere where ozone information can be retrieved from satellite measurements. In Chapter 4, the model representation of NO_2 and O_3 tropospheric columns improved with the addition of lightning-NO_x emissions at the location of NLDN flash rates. Upper level winds and convection ahead of a passing cold-front at the end of the smog event exported a large amount of anthropogenic and natural O_3 and NO_x from the continent over the western North Atlantic. The OMI/MLS TCO product did not capture the high distribution of O_3 in this event; but the OMI product, TES and the model show a large maximum off the U.S. East Coast. In the LNO_x sensitivity run, tropospheric NO_2 column increased by 4-10 x 10^{15} molecules/cm^2, tropospheric column ozone was enhanced 6-10 DU and surface O_3 was enhanced 4-8 ppbv in areas downwind of convective events within pollutant outflow region.

O_3 enhancements in profiles over ocean are not seen in the CO and O_3 *a priori*, suggesting that satellites are detecting ozone with possible sources from surface pollution and lightning NO_x. HYSPLIT back trajectories associated with high TES and OMI TCO over western North Atlantic Ocean were influenced by a combination of boundary layer pollution and lightning-induced O_3. In one regime, back trajectories from TES retrievals passed over the Baltimore-Washington metropolitan area and the Great Lakes region within the preceding 72 hours. Another regime was influenced by transport of polluted air mass off the coast of Georgia, North Carolina and South Carolina. Both regimes encountered lightning activity. Calculated TES O_3-CO correlations over the western Northern Atlantic region yielded a high $\Delta O_3/\Delta CO$ enhancement ratio of 0.51 mol/mol and a weak correlation coefficient R=0.3. The contribution of lightning-induced O_3 to high TES TCO explain low correlation with surface CO and high enhancement ratio. OMI and TES retrievals were used to map outflow of eastern U.S. pollution during a severe smog event. I showed that natural and anthropogenic sources contribute to high TCO in retrieved pollutant outflow plumes.

In Chapter 5, a historical O_3 data set from the 1978-1979 Winter Monsoon Experiment (WMONEX) over the Western Pacific was used to investigate open convection cells. These tropical cloud rings are characterized by circular structure with cumulus ring walls and a clear area in the center, presenting an interesting mesoscale dynamics problem and probable net sink for tropospheric O_3. I examined *in situ* O_3 measurements within convective ring clouds. Presented here for the first time, WMONEX ozone observations were used to demonstrate how convection leads

to the redistribution and destruction of ozone in the tropical marine environment. O_3 was observed to increase in the clear center of the cloud ring and decrease in the convective cloud walls, consistent with subsidence of ozone-rich air from the upper troposphere and lifting of ozone-depleted air from below. The 70-80 ppb O_3 mixing-ratios within the rings were too high to descend directly from aloft. I showed that the O_3 within the cloud rings over the South China Sea possibly originated in upwind convective clouds, undergoing lightning NO production, over Indonesia. From a chemical transport model, ozone production due to lightning NO in a convective cloud was on the order of 11-22 ppb within 48 hours of the lightning occurrence. These tropical ozone data from the late 1970's may also serve as a benchmark for assessing changes in atmospheric composition resulting from emission changes in rapidly developing East Asia.

6.2 *Recommendations for Future Work*

Many of the limitations of the current study can be used as a starting point for future work. Deficiencies in the RADM2 chemical mechanism used in this dissertation can be addressed by adjusting reaction rates of NO_x species within known uncertainties. More importantly, development of a chemical mechanism that takes into account organo-nitrates (including isoprene nitrates) and nitryl chloride chemistry is needed to improve regional air quality modeling efforts. More ground and in-situ observations of alkyl nitrates and NO_y species would help develop a more accurate and explicit chemical mechanism.

The use of Four-Dimensional Data Assimilation in regional WRF/Chem studies needs to be studied closer, especially for the Southeast U.S. region, where

high temperature biases result in overprediction of O_3 production. Meteorology fields nudged with analysis and observational data improve WRF meteorology only runs [*Zhang et al*., 2009]. Ambient temperature and planetary boundary layer heights are possibly driving some of the high model biases in the Southeast U.S. More observations of PBL heights are needed to confirm model performance. A network of wind profilers and Light Detection and Ranging (LIDAR) instruments is needed over contiguous U.S. for improvement of modeling studies.

For WRF/Chem studies in the mid-to-upper troposphere, more rigorous algorithm is needed to distribute lightning NO emissions within the modeling domain. Ideally, lightning emissions should be prescribed to grid boxes, where convection with lightning is occurring. More accurate lightning NO emissions in the model will improve the accuracy of predicted NO and O_3 profiles and surface fields.

Winter MONEX observations over the Western Pacific can be used in atmospheric composition studies in conjunction with future campaigns. East Asian countries are undergoing fast economic growth and rapid urbanization at the expense of the environment. Fossil fuel and biomass burning emissions are rapidly increasing in this region. Southeast Asia Composition, Cloud, Climate Coupling Regional Study (SEAC4RS) is currently planned for 2012 in the tropical Southeast Asia. This airborne campaign will investigate atmospheric processes related to deep convection, atmospheric chemistry, aerosols and clouds in the marine, tropical environment. WMONEX measurements can be used to investigate changes in atmospheric composition in a quickly developing, overpopulated region with growing environmental problems.

Appendix A: Evaluation of convection in MM5/CMAQ

The timing and location of convection can determine when and where maximum pollutant concentrations are observed. How realistically a regional-scale or a multi-scale chemical transport model depicts an air pollution event or its transport depends on meteorological fields used in the model.

Before the emergence of WRF/Chem as a leading regional chemical model, Community Multiscale Air Quality modeling system (CMAQ) was the main model used for regional air quality modeling. Prior to availability of WRF meteorological fields, CMAQ incorporated meteorological output fields from the fifth-generation Pennsylvania State University–National Center for Atmospheric Research Mesoscale Model (MM5) modeling system. Thus how well CMAQ simulates vertical uplift of pollution during convective events depends on how well MM5 captures convective events in comparison with observations.

A verification of short-range numerical model forecasts of warm season convection was conducted over two U.S. regions: Northeast and Midwest. All available days from the summer 2002 were evaluated using accumulated precipitation products from the NCEP hourly, multi-sensor National Precipitation Analysis (NCEP NPA) and MM5 model with Modified Blackadar PBL scheme and Kain–Fritsch convective parameterization.

Area averages over two 500 km^2 regions show good agreement between model forecast and observations with an average R^2 value of 0.76. The square of the correlation coefficient decreases to 0.42 as the area of comparison is gradually decreased to a 16 km^2 region. Analysis of the diurnal cycle of model and observed

accumulated precipitation showed that MM5 peak precipitation is on average 2-3 hours earlier and 25% - 42% greater in magnitude than NCEP NPA (Figure A.). Overall MM5 correctly forecasts large-scale convective events, but time lag in the peak precipitation might be problematic for air quality modeling.

Verification of convective occurrence was based on contingency table (Table A.1) in which each element of the table equals the number of occurrences in which CMAQ and NCEP did or did not report precipitation over a 24 hour period [*Wilks*, 1995]. The canonical threat score is a measure of the fractional overlap between the observed and model areas meeting or exceeding a specified precipitation threshold (here 1.25 mm):

		Observed	
		Yes	No
Forecast	Yes	A	b
	No	C	d

Table A.1 A 2x2 contingency table. Shaded boxes are correct forecasts.

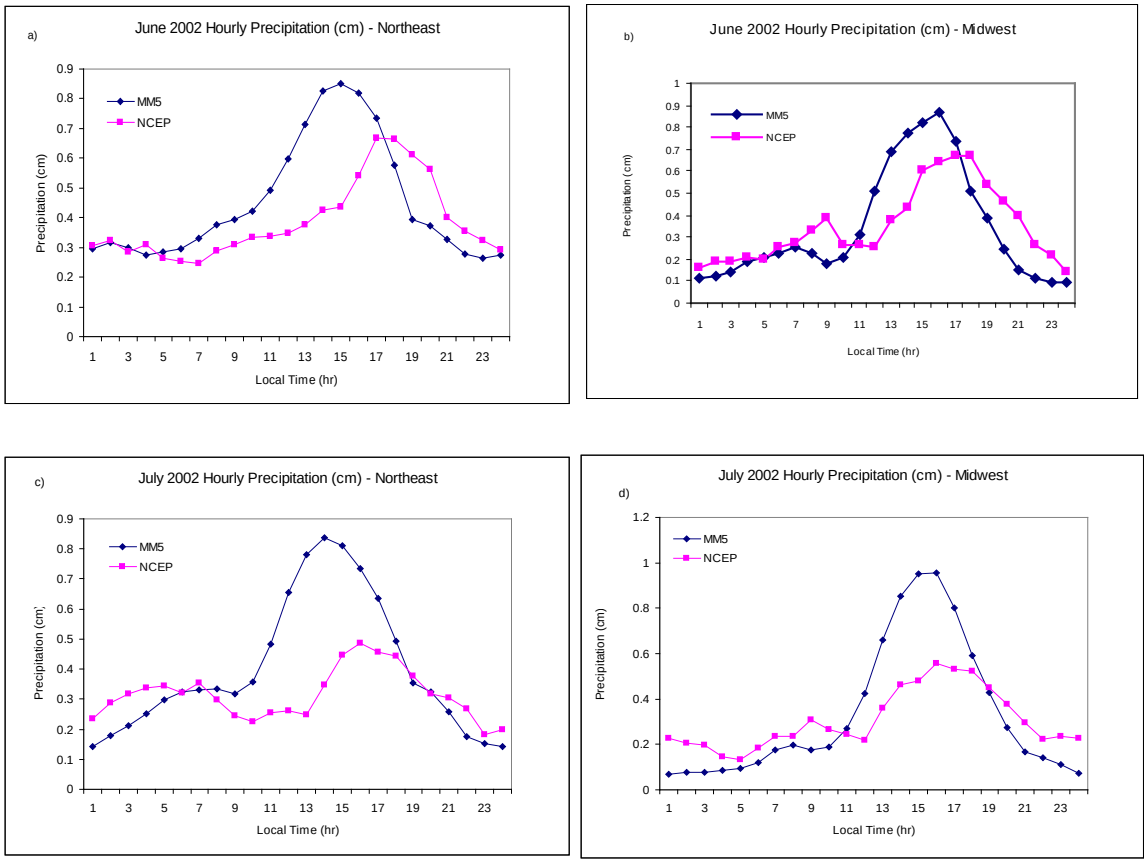

Figure A.1 Total hourly precipitation for June and July 2002 in the two 500 km^2 regions: Northeast and Midwest.

Contingency forecasts of the area coverage of the 24-h accumulated precipitation in convective events show skill comparable to the lower-resolution, operational models (Table A.2), with median threat scores of 0.358 and 0.326 for all modes of convection (defined as linear, multicellular, or isolated) for Northeast and Midwest respectively. The definitions for the convection modes are as follows: *linear convection* - length to width ratio of at least 3:1, persists for at least 3 hours, and has an areal coverage of at least 500 km^2; *multicellular convection* - length:width ratio less than 3:1, persists for at least 3 hours and has an areal coverage of at least 500 km^2, *isolated convection* - spatial coverage of less than 500 km^2. Analysis was performed only for days when convection occurred. When calculated by convective

mode, threat scores are highest for most organized modes with largest spatial scale – linear (0.721, 0.533) and multicellular (0.55, 0.344), and the lowest for small scale isolated events (0.171, 0.134). Threat scores are comparable with published results for operational models.

Percentile	**Threat Score (Threshold = 1.25 mm)**	
All Convection	**Northeast (43 days)**	**Midwest (43 days)**
25th	0.171	0.180
50th	0.358	0.326
75th	0.636	0.466
Linear	**Northeast (5 days)**	**Midwest (7 days)**
25th	0.638	0.438
50th	0.721	0.533
75th	0.818	0.674
Multicellular	**Northeast (20 days)**	**Midwest (25 days)**
25th	0.333	0.250
50th	0.550	0.344
75th	0.678	0.434
Isolated	**Northeast (18 days)**	**Midwest (11 days)**
25th	0.124	0.109
50th	0.171	0.134
75th	0.288	0.200

Table A.2. Threat scores calculated by type of convection (all, linear, multicellular, isolated) and by region (Northeast, Midwest).

Overall MM5 and NCEP Stage II observations show good agreement. The limiting resolution for agreement is variable from 5°x5° to 1°x1°. MM5 shows

stronger peak precipitation a few hours before actually observed in NCEP NPA. This time lag in diurnal cycle should be considered when analyzing CMAQ simulations.

Bibliography

Agee, E.M., et al. (1979), A review of mesoscale cellular convection, *Bull. of Amer. Met. Soc.*, 54, 10, 1004-1012.

Alexander, B., et al. (2009), Quantifying atmospheric nitrate formation pathways based on a global model of the oxygen isotopic composition ($\Delta^{17}O$) of atmospheric nitrate, *Atmos. Chem. Phys*., 9, 5043-5056.

Allen, D., K. Pickering, B. Duncan, and M. Damon (2010), Impact of lightning NO emissions on North American photochemistry as determined using the Global Modeling Initiative (GMI) model, *J. Geophys. Res.*, 115, D22301, doi:10.1029/2010JD014062.

Al-Saadi, J., et al. (2005), Improving National Air Quality Forecasts with Satellite Aerosol Observations, *Bull. Amer. Meteor. Soc.*, 86, 1249–1261.

Atkinson B.W. and J.W. Zhang (1996), Mesoscale shallow convection in the atmosphere, *Reviews of Geophysics*, 34, 403–431.

Beer, R., et al. (2001), Tropospheric emission spectrometer for the Earth Observing System's Aura Satellite, *Applied Optics, 40*(15), 2356-2367, doi:10.1364/AO.40.002356.

Bell, M. L., A. McDermott, S. L. Zeger, J. M. Samet, and F. Dominici (2004): Ozone and short-term mortality in 95 U.S. urban communities. *J. Amer. Med. Assoc*., 292, 2372−2378.

Bethan, S., et al. (1998), Chemical air mass differences near fronts, *J. Geophys. Res.*, *103*, 13,413– 413,434.

Blanchard, C., and S. Tanenbaum (2006), Weekday/Weekend Differences in Ambient Air Pollutant Concentrations in Atlanta and the Southeastern United States, *J. Air & Waste Manage. Assoc.*, 56, 271–284.

Boccippio, D., K. Driscoll, W. Koshak, R. Blakeslee, W. Boeck, D. Mach, D. Buechler, H. J. Christian, and S. J. Goodman (2000), The Optical Transient Detector (OTD): Instrument Characteristics and Cross-Sensor Validation, *J. Atmos. Oceanic Tech.*, *17*, 441-458.

Boccippio, D. J., K. L. Cummins, H. J. Christian, and S. J. Goodman (2001), Combined satellite- and surface-based estimation of the intracloud-cloud-to-ground lightning ratio over the continental United States, *Mon. Weather Rev.*, 129, 108–122.

Boccippio, D. J., W. J. Koshak, and R. J. Blakeslee (2002), Performance assessment of the Optical Transient Detector and Lightning Imaging Sensor, I: Predicted diurnal variability, *J. Atmos. Oceanic Technol., 19*, 1318–1332.

Boersma, K.F., et al., (2007), Near-real time retrieval of tropospheric NO_2 from OMI. *Atmos. Chem. and Phys*. 7, 2103–2118.

Bolhofer, W., M. Chambers, D. Frey, J. Kuettner, and S. Unninayar (1981),Winter MONEX U.S. Research Flight Missions, December 1978. NCAR Technical Note #NCAR/TN-167+STR.

Browning, K. A. (1990), Organization of clouds and precipitation in extratropical cyclones, Extratropical cyclones: The Erik H. Palmen Memorial Volume, *Amer. Meteor. Soc.*, 129-153.

Bucsela, E. J., et al. (2008), Comparison of tropospheric NO_2 from in situ aircraft measurements with near-real-time and standard product data from OMI, *J. Geophys. Res., 113*, D16S31, doi:10.1029/2007JD008838.

Cai., C., et al. (2008), Performance evaluation of an air quality forecast modeling system for a summer and winter season – Photochemical oxidants and their precursors, *Atmos. Environ.*, 42, 8585-8599.

Carter, W.P.L., (1996). Condensed atmospheric photooxidation mechanisms for isoprene. *Atmos. Environ*. 30, 4275–4290.

Castellanos, P., et al. (2010), Ozone, nitrogen oxides, and carbon monoxide during pollution events over the eastern US: An evaluation of emissions and vertical mixing, *J. Geophys. Res*, submitted.

Celarier, E. A., et al. (2008), Validation of Ozone Monitoring Instrument nitrogen dioxide columns, *J. Geophys. Res., 113*, D15S15, doi:10.1029/2007JD008908.

Chance, K., (2002), OMI Algorithm Theoretical Basis Document, in OMI Trace Gas Algorithms, ATBD-OMI-04. NASA Distrib. Active Archive Centre, Greenbelt, MD, 1336 pp.

Chance, K., (2006), Spectroscopic measurements of tropospheric composition from satellite measurements in the ultraviolet and visible: steps toward continuous pollution monitoring from space. In: Perrin, A., Ben Sari-Zizi, N., Demaison, J. (Eds.), Remote Sensing of the Atmosphere for Environmental Security. Springer, ISBN 1-4020-5089-5, pp. 1–25.

Chatfield, R. B. and P.J. Crutzen (1984), Sulfur dioxide in remote oceanic air: Cloud transport of reactive precursors, *J. Geophys. Res*., 89, 7111-7132.

Christian, H. J., et al. (2003), Global frequency and distribution of lightning as observed from space by the Optical Transient Detector, *J. Geophys. Res.*, *108* (D1), 4005, doi:10.1029/2002JD002347.

Chu, D. A., Y. J. Kaufman, C. Ichoku, L. A. Remer, D. Tanre, and B. N. Holben (2002), Validation of MODIS aerosol optical depth retrieval over land, *Geophys. Res. Lett.*, 29(12), 8007, doi:10.1029/2001GL013205.

Clerbaux, C., D. P. Edwards, M. Deeter, L. Emmons, J.-F. Lamarque, X. X. Tie, S. T. Massie, and J. Gille (2008), Carbon monoxide pollution from cities and urban areas observed by the Terra/MOPITT mission, *Geophys. Res. Lett.*, 35, L03817, doi:10.1029/2007GL032300.

Cooper, O. R., et al. (2004), A case study of transpacific warm conveyor belt transport: Influence of merging airstreams on trace gas import to North America, *J. Geophys. Res*, *109*.

Cooper, O. R., et al. (2006), Large upper tropospheric ozone enhancements above midlatitude North America during summer: In situ evidence from the IONS and MOZAIC ozone measurement network, *J. Geophys. Res.*, 111, D24S05, doi:10.1029/2006JD007306.

Crutzen, P.J., (1979): The role of NO and NO_2 in the chemistry of the troposphere and stratosphere. *Ann. Rev. Earth Planet. Sci.*, 7, 443-472.

DeCaria, A. J. (2000), Effects of convection and lightning on tropospheric chemistry studied with cloud, transport, and chemistry models, PhD dissertation, University of Maryland, College Park, 169 pp.

DeCaria A. J., K. E. Pickering, G. L. Stenchikov, and L. E. Ott (2005): Lightning-generated NO_x and its impact on tropospheric ozone production: A three-dimensional modeling study of a Stratosphere-Troposphere Experiment: Radiation, Aerosols and Ozone (STERAO-A) thunderstorm, *J. Geophys. Res*., 110, D14303, doi:10.1029/2004JD005556.

Deeter, M., et al. (2002), Validation of MOPITT Radiances, IGARSS 2002, Canada, June 24-28, 2002.

Dickerson, et al., (1987), Thunderstorms: An Important Mechanism in the Transport of Air Pollutants, *Science*, 235 (4787), 460.

Dickerson, R. R., et al. (1999), Ozone in the remote marine boundary layer: A possible role for halogens, *J. Geophys Res*., 104, 21385-21395.

Diem, J.E. (2009), Atmospheric characteristics conducive to high-ozone days in the Atlanta metropolitan area, *Atmos. Envir.* 43 (25), 3902-3909, doi: 10.1016/j.atmosenv.2009.04.050.

Draxler, R.R. and G.D. Rolph (2003). HYSPLIT (HYbrid Single-Particle Lagrangian Integrated Trajectory) Model access via NOAA ARL READY Website (http://www.arl.noaa.gov/ready/hysplit4.html). NOAA Air Resources Laboratory, Silver Spring, MD.

Earth Sciences and Image Analysis, NASA-Johnson Space Center. 9 Feb. 2004. "The Gateway to Astronaut Photography of Earth." http://eol.jsc.nasa.gov/Info/use.htm

Eder, B., et al. (2009), A performance evaluation of the National Air Quality Forecast Capability for the summer of 2007, *Atmos. Environ*., 43, 2312-2320.

Emmons, L.K., et al., (2010), Description and evaluation of the Model for Ozone and Related chemical Tracers, version 4 (MOZART-4), *Geosci. Model Dev*., 3, 43-67.

EPA, 2005 National Emission Inventory, http://www.epa.gov/ttn/chief/eiinformation.html, accessed on December 23, 2010.

Eremenko, M., et al. (2008), Tropospheric ozone distributions over Europe during the heat wave in July 2007 observed from infrared nadir spectra recorded by IASI, *Geophys. Res. Lett*., 35, L18805, doi:10.1029/2008GL034803.

Fehsenfeld, F. C., et al. (2006), International Consortium for Atmospheric Research on Transport and Transformation (ICARTT): North America to Europe—Overview of the 2004 summer field study, *J. Geophys. Res.*, 111, D23S01, doi:10.1029/2006JD007829.

Finlayson-Pitts B.J. and N. Pitts, (1993), VOCs, NOx and ozone production. *J. Air Waste Mgmt. Assoc*., 43,1093-1101.

Fiore, A. M., et al. (2002), Background ozone over the United States in summer, origin, trend, and contribution to pollution episodes, *J. Geophys Res*., 107 (D15), 4275.

Fishman, J., and J. C. Larsen (1987), Distribution of total ozone and stratospheric ozone in the tropics: Implications for the distribution of tropospheric ozone, *J. Geophys. Res.*, *92*(D6), 6627 - 6634.

Fishman, J., et al. (2008), Remote sensing of tropospheric pollution from space, *B. Am. Meteor. Soc.,* 89, 805–821.

Frost, G. J., et al. (2006), Effects of changing power plant NOx emissions on ozone in the eastern United States: Proof of concept, *J. Geophys. Res*., 111, D12.

Gaza, Robert S., (1998), Mesoscale Meteorology and High Ozone in the Northeast United States. *J. Appl. Meteor*., 37, 961–977.

Gilliland, A. B., et al. (2008), Dynamic evaluation of regional air quality models: Assessing changes in O_3 stemming from changes in emissions and meteorology, *Atmos. Environ*, *42*(20), 5110-5123.

Godowitch, J. M., A. B. Gilliland, R. R. Draxler, and S. T. Rao (2008), Modeling Assessment of point source NO_x Emission Reductions on Ozone Air Quality in the Eastern United States, *Atmos. Environ.*, *42*(1), 87-100.

Greenfield, R.S., and T.N. Krishnamurti (1979), The Winter Monsoon Experiment – Report of December 1978 Phase, *Bull. Amer. Meteor. Soc*., 60, 439-444.

Grell, G. A., et al. (2005), Fully coupled "online" chemistry within the WRF model, *Atmos. Environ.*, *39*(37), 6957-6975, doi:10.1016/j.atmosenv.2005.04.027

Grogan, M. J. (2004): Report on the 2002–2003 U.S. NLDN system-wide upgrade, Vaisala Thunderstorm, Tucson, Ariz, USA.

Guenther, A.B., Zimmerman, P.R., Harley, P.C., Monson, R.K., Fall, R., (1993). Isoprene and monoterpene emission rate variability: model evaluations and sensitivity analyses, *J. Geophys. Res*., 98D, 12609–12617.

Guenther, A., et al. (2006), Estimates of global terrestrial isoprene emissions using MEGAN (Model of Emissions of Gases and Aerosols from Nature), *Atmos. Chem. Phys*., 6(11), 3181– 4055.

Harrold, T. W. (1973), Mechanisms influencing the distribution of precipitation within baroclinic disturbances, *Q. J. R. Meteorol. Soc.*, *99*, 232-251.

Hegarty, J., H. Mao, and R. Talbot (2010): Winter- and summertime continental influences on tropospheric O_3 and CO observed by TES over the western North Atlantic Ocean, *Atmos. Chem. Phys*., 10, 3723-3741, doi:10.5194/acp-10-3723-2010.

Helfand, M. and E. Kalnay (1983), A Mechanism for open or closed cellular convection, *J. Atmos. Sci*., 40, 631-650.

Hidayat, S. and M. Ishii (1999),Diurnal variation of lightning characteristics around Java Island, *J. Geophys Res*., 104, 24449-24454.

Hirsch, R.M., and E.J Gilroy (1984), Methods of fitting a straight line to data: Examples in water resources: *Water Resources Bulletin*, v.20, no. 5, p. 705-712.

Holton, J. R.: 1967, The diurnal boundary layer wind oscillation above sloping terrain. *Tellus*, 19, 199-205.

Honrath, R. E., R. C. Owen, M. Val Martín, J. S. Reid, K. Lapina, P. Fialho, M. P. Dziobak, J. Kleissl, and D. L. Westphal (2004), Regional and hemispheric impacts of anthropogenic and biomass burning emissions on summertime CO and O_3 in the North Atlantic lower free troposphere, *J. Geophys. Res.*, 109, D24310, doi:10.1029/2004JD005147.

Hopkins, A., et al. (2010), WRF-Chem lightning NO_x parameterization at Florida State University: $FSULNO_x$, paper presented at 90th Annual American Meteorological Society Meeting, Atlanta, GA.

Houze, R. A., S. G. Goetis, F. D. Marks, and A. K. West (1981), Winter monsoon convection in the vicinity of north Borneo. Part I: Structure and time variation of clouds and precipitation. *Mon. Wea. Rev*., 109, 1595−1614.

Hubert, L.F. (1966), Mesoscale cellular convection, Meteorological Satellite Laboratory report, no. 37., U.S. Department of Commerce., 68 pp.

Hudman, R. C., et al. (2007), Surface and lightning sources of nitrogen oxides over the United States: Magnitudes, chemical evolution, and outflow, *J. Geophys. Res*., 112, D12S05, doi:10.1029/2006JD007912.

Hudson, R. D. and A. M. Thompson (1998), Tropical tropospheric ozone from total ozone mapping spectrometer by a modified residual method, *J. Geophys. Res*., 103, 22,129- 122,145.

IPCC (2007), Climate Change 2007: The Physical Science Basis. Contribution of Working Group I to the Fourth Assessment Report of the Intergovernmental Panel on Climate Change [S. Solomon, D. Qin, M. Manning, Z. Chen, M. Marquis, K. B. Averyt, M. Tignor and H. L. Miller (eds)]. Cambridge, United Kingdom and New York, NY, USA, pp. 996.

Jaffe, D.A. et al. (2003), Six new episodes of trans-Pacific transport of air pollutants, *Atmos. Environ.,* 37, 391-404.

Johnson, R. H. and Zimmerman, J. R. (1986), Modification of the boundary layer over the South China Sea during a Winter MONEX cold surge event, *Mon. Wea. Rev*., 114, 2004-2015.

Jourdain, L., S. S. Kulawik, H. M. Worden, K. E. Pickering, J. Worden, and A. M. Thompson (2009), Lightning NOx emissions over the USA investigated using TES, NLDN, LRLDN, IONS data and the GEOS-Chem model, *Atmos. Chem. Phys. Discuss*., 9, 1123–1155.

Kang D. and B. Elder (2005), The New England air quality forecasting pilot program: development of an evaluation protocol and performance benchmark, *J. Air and Waste Manage. Assoc.*, 55, 1782-1796.

Kar, J., J. Fishman, J. K. Creilson, A. Richter, J. Ziemke, and S. Chandra (2010), Are there urban signatures in the tropospheric ozone column products derived from satellite measurements? *Atmos. Chem. Phys.*, 10, 5213–5222.

Kaufman, Y. J., D. Tanre´, L. A. Remer, E. F. Vermote, A. Chu, and B. N. Holben (1997), Operational remote sensing of tropospheric aerosol over the land from EOS-MODIS, *J. Geophys. Res*., 102, 17,051– 17,067.

Kelly, T. J., et al. (1980), Measurements of oxides of nitrogen and nitric acid in clean air, *J. Geophys. Res*., 85, 7417-7425.

Kim, S.W., et al. (2009), NO_2 columns in the western United States observed from space and simulated by a regional chemistry model and their implications for NO_x emissions, *J. Geophys. Res.*, 114, D11301, doi:10.1029/2008JD011343.

Kita, K., et al. (2003), Photochemical production of ozone in the upper troposphere in association with cumulus convection over Indonesia, *J. Geophys Res*., 108 (D3), 8400.

Kley, D., et al. (1996), Observations of near-zero ozone concentrations over the convective Pacific: Effects on air chemistry. *Science*, 274, 230-233.

Koelemeijer, R.B.A., de Haan, J.F., Stammes, P. (2003), A database of spectral surface reflectivity of the Earth in the range 335–772 nm derived from 5.5 years of GOME observations. *Jour of Geophys Res.*, 108, 4070, doi:10.1029/2002JD002429.

Kondragunta, S. (1997): The impact of aerosols on urban photochemical ozone production. Ph.D. dissertation, University of Maryland, College Park, MD.

Koshak, W.J., et al., (2004), North Alabama Lightning Mapping Array (LMA): VHF Source Retrieval Algorithm and Error Analyses. *J. Atmos. Oceanic Technol.*, **21**, 543–558.

Koshak, W. J., H. S. Peterson, E. W. McCaul, and A. Biazar (2010), Estimates of the lightning-NO_x profile in the vicinity of the North Alabama Lightning Mapping Array, 21st International Lightning Detection Conference (ILDC)/Vaisala, 18-22 Apr. 2010, Orlando, FL, United States, NASA Technical Report Document 20100021055.

Kuhns, H. D., et al. (2004), Remote sensing of PM, NO, CO and HC emission factors for on-road gasoline and diesel engine vehicles in Las Vegas, NV, *Science of the Total Environment*, 322, 123-137, doi:10.1016/j.scitotenv.2003.09.013.

Kulawik, S. S., et al. (2006), Implementation of cloud retrievals for Tropospheric Emission Spectrometer (TES) atmospheric retrievals: part 1. Description and characterization of errors on trace gas retrievals, *J. Geophys. Res.*,, *111*(D24204), doi:10.1029/2005jd006733.

Lamsal, L. N., R. V. Martin, A. van Donkelaar, E. A. Celarier, E. J. Bucsela, K. F. Boersma, R. Dirksen, C. Luo, and Y. Wang (2010), Indirect validation of tropospheric nitrogen dioxide retrieved from the OMI satellite instrument: Insight into the seasonal variation of nitrogen oxides at northern midlatitudes, *J. Geophys. Res.*, 115, D05302, doi:10.1029/2009JD013351.

Lawrence, M.G., et al. (2003), The balance of effects of deep convective mixing on tropospheric ozone. *Geophys. Res. Lett*., 94 (D4), 5029-5041.

Lelieveld, J. and Crutzen, P. J. (1994), Role of deep cloud convection in the ozone budget of the troposphere. *Science*, 264, 1759-1761.

Levelt, P. F., et al. (2006), Science Objectives of the Ozone Monitoring Instrument, *IEEE Trans. Geosci. Remote Sens.*, *44*, 1199-1208, doi: 0.1109/TGRS.2006.872336.

Levy, H. II (1971), Normal atmosphere: Large radical and formaldehyde concentrations predicted. *Science*, 173, 141-143.

Li, Q., D. J. Jacob, R. Park, Y. Wang, C. L. Heald, R. Hudman, R. M. Yantosca, R. V. Martin, and M. Evans (2005), North American pollution outflow and the trapping of convectively lifted pollution by upper-level anticyclone, *J. Geophys. Res*., 110, D10301, doi:10.1029/2004JD005039.

Liu, H., et al. (2003), Transport pathways for Asian pollution outflow over the Pacific: Interannual and seasonal variations, *J. Geophys. Res*, *108*, 8786.

Liu, X., et al. (2005), Ozone profile and tropospheric ozone retrievals from Global Ozone Monitoring Experiment: Algorithm description and validation, *J. Geophys. Res.*, *110* (D20307), doi:10.1029/2005JD006240.

Liu, X., et al. (2009), Ozone profile retrievals from the Ozone Monitoring Instrument, *Atmos. Chem. Phys. Discuss.*, 9, 22693–22738.

Loranger, D. C.: Mesoscale convective cloud rings in the tropics. M.S. thesis, Dept. of Atmospheric Science, Colorado State University. Fort Collins, CO, 1974.

Loughner, C.P., D.J. Allen, K.E. Pickering, R.R. Dickerson, D.-L. Zhang, and Y.-X. Shou (2010), Impact of the Chesapeake Bay breeze and fair-weather cumulus clouds on pollutant transport and transformation, submitted to *Atmos. Environ.*

Luke, W. T., et al. (1989), Direct Measurements of the Photolysis Rate Coefficients and Henry's Law Constants of Several Alkyl Nitrates, *J. Geophys. Res.*, *94*(D12), 14905-14921.

Luke, W. T., et al. (1992), Tropospheric chemistry over the lower Great Plains of the United States 2: Trace gas profiles and distributions, *J. Geophys. Res*., 97 (18), 20647-20670.

Mao, H., et al. (2010), A comprehensive evaluation of seasonal simulations of ozone in the northeastern U.S. during summers of 2001-2005, *Atmos. Chem. Phys*., 10, 9-27.

Mari, C., et al. (2004), Export of Asian pollution during two cold front episodes of the TRACE-P experiment, *J. Geophys. Res*, 109.

Martin, R.V., et al. (2002), An improved retrieval of tropospheric nitrogen dioxide from GOME. *J. of Geophys. Res*., 107, 4437. doi:10.1029/2001JD001027.

Martin, R. V., B. Sauvage, I. Folkins, C. E. Sioris, C. Boone, P. Bernath, and J. Ziemke (2007), Space-based constraints on the production of nitric oxide by lightning, *J. Geophys. Res*., 112, D09309, doi:10.1029/2006JD007831.

Martin, R. V. (2008), Satellite remote sensing of surface air quality, *Atmos. Envir.*, 42, 34, 7823-7843, doi:10.1016/j.atmosenv.2008.07.018.

Martini, M., et al. (2010), The impact of North American anthropogenic emissions and lightning on long range transport of trace gases and their export from the continent during summers 2002 and 2004, *J. Geophys. Res.*, accepted.

McPeters, R. D., et al. (2007), Ozone climatological profiles for satellite retrieval algorithms, *J. Geophys. Res.*, *112*(D05308), 05310.01029/02005JD006823.

Maryland Department of Environment (MDE), (2010), Protocol for WRF meteorological modeling in support of regional SIP air quality modeling in the OTR, Baker, D. (ed). Baltimore, MD, pp. 74.

Mena-Carrasco, M., et al.(2007), Improving regional ozone modeling through systematic evaluation of errors using the aircraft observations during the International Consortium for Atmospheric Research on Transport and Transformation, *J. Geophys. Res*., 112, D12S19, doi:10.1029/2006JD007762.

Middleton, P., et al. (1990) Aggregation and analysis of volatile organic compound emissions for regional modeling. *Atmos. Environ*., 24A, 1107−1133.

Molina, L. T., et al. (2007), Air quality in North America's most populous city – overview of the MCMA-2003 campaign, *Atmos. Chem. Phys*., 7, 2447-2473, doi:10.5194/acp-7-2447-2007.

Millet, D. B., et al. (2006), Formaldehyde distribution over North America: Implications for satellite retrievals of formaldehyde columns and isoprene emission, *J. Geophys. Res.*, *111*, D24S02, doi: 10.1029/2005JD006853.

Nassar, R., et al. (2008), Validation of Tropospheric Emission Spectrometer (TES) nadir ozone profiles using ozonesonde measurements, *J. Geophys. Res.*, *113*(D15S17), doi:10.1029/2007JD008819.

Osterman, G. (2009), Tropospheric Emission Spectrometer TES L2 data user's guide, version 4.0, edited, Pasadena.

Ott, L. E., K. E. Pickering, G. L. Stenchikov, D. J. Allen, A. J. DeCaria, B. Ridley, R.F. Lin, S. Lang, and W.K. Tao (2010), Production of lightning NO_x and its vertical distribution calculated from three dimensional cloud scale chemical transport model simulations, *J. Geophys. Res.*, 115, D04301, doi:10.1029/2009JD011880.

Parrish, D. D. (2006), Critical evaluation of US on-road vehicle emissions inventory, *Atmos. Environ*., 40, 2288-2300, doi:10.1016/j.atmosenv.2005.11.033.

Perring, A, E., et al. (2009), Airborne observations of total $RONO_2$: new constraints on the yield and lifetime of isoprene nitrates, *Atmos. Chem. Phys*, 9, 1451-1463.

Pickering, K. E., A. M. Thompson, J. R. Scala, W.-K. Tao, R. R. Dickerson, and J. Simpson (1992), Free Tropospheric Ozone Production Following Entrainment of Urban Plumes Into Deep Convection, *J. Geophys. Res.*, 97(D16), 17,985–18,000.

Pickering, K. E., Y. S. Wang, and W. K. Tao (1998), Vertical distributions of lightning NO_x for use in regional and global chemical transport models, *J. Geophys. Res*., 103, 23, 31203-31216.

Pierce, T., Geron, C., Bender, L., Dennis, R., Tonneson, G., Guenther, A., (1998). Influence of increased isoprene emissions on regional ozone modelling. *J. Geophys. Res.*, 103, 25611–25629.

Pope, C. A (2000), Epidemiology of fine particulate air pollution and human health: Biologic mechanisms and who's at risk? *Environ. Health Perspect*., 108, 713−723.

Poulida, O., K. L. Civerolo, and R. R. Dickerson (1994), Observations and tropospheric photochemistry in central North Carolina, *J. of Geophys. Res.*, 99(D5), 553-563, doi:10.1029/94JD00404.

Prados, A. I., Dickerson, R. R. , Doddridge, B. G. , Milne, P. A., Moody, J. L., and Merrill, J. T. (1999) Transport of ozone and pollutants from North America to the North Atlantic Ocean during the 1996 Atmospheric/Ocean Chemistry Experiment (AEROCE) intensive, *J. Geophys. Res*., 104, 26, 219-26, 233.

Price, C., J. Penner, and M. Prather (1997), NOx from lightning: 1. Global distribution based on lightning physics, *J. Geophys. Res*., 102(D5), 5929– 5942.

Rao, S.T, et al. (2003), Summertime Characteristics of the Atmospheric Boundary Layer and Relationships to Ozone Levels over the Eastern United States, *Pure Appl. Geophys.* 160, 21−55.

Remer, L. A., et al. (2002), Validation of MODIS aerosol retrieval over ocean, *Geophys. Res. Lett.*, 29(12), 8008, doi:10.1029/2001GL013204.

Ruprecht, E., et al. (1973), Radarbeobachtungen der Konvektionsgebiete im Bereich der Innertropischen Konvergenzone uber dem aquatorialen Atlantischen Ozean. Meteor Forschungsergebnisse Reihe B..

Ryan, W.F., et al. (1998), Pollutant transport during a regional O_3 episode in the Mid-Atlantic States, *J. Air & Waste Manag. Assoc*., 48, 174-185.

Ryan, W. F., et al. (2000), Air quality forecasts in the mid-Atlantic region: Current practice and benchmark skill, *Weather and Forecasting*, *15*(1), 46-60.

Schoeberl, M. R., et al. (2007), A trajectory-based estimate of the tropospheric ozone column using the residual method, *J. Geophys. Res.*, *112*(D24S49).

Schumann, U and H. Huntrieser, (2007), The global lightning-induced nitrogen oxides source, *Atmos. Chem. Phys*., 7, 3823-3907.

Schwab, J. J., et al. (2009), Ozone, trace gas, and particulate matter measurements at a rural site in Southwestern New York State: 1995-2005, *Journal of the Air and Waste Management Association*, *59*, 293-309.

Seinfeld, J.H., and S.N. Pandis (1998), Atmospheric Chemistry and Physics, 1326 pp., Wiley-Interscience.

Singh, H. B., W. H. Brune, J. H. Crawford, D. J. Jacob, and P. B. Russell (2006), Overview of the summer 2004 Intercontinental Chemical Transport Experiment–North America (INTEX-A), *J. Geophys. Res.*, 111, D24S01, doi:10.1029/2006JD007905.

Singh, H. B., et al. (2007), Reactive nitrogen distribution and partitioning in the North American troposphere and lowermost stratosphere, *J. Geophys. Res*., 112, D12.

Stauffer, D., N. Seaman, and F. Binkowski, (1991). Use of four-dimensional data assimilation in a limited-area mesoscale model. Part II: Effects of data assimilation within the planetary boundary layer. *Mon. Wea. Rev.*, 119, 734–754

Stehr, J.W. (2005), A Guide to Mid-Atlantic Regional Air Quality, MARAMA, Mid-Atlantic Regional Air Management Association, Baltimore, Maryland.

Stockwell, W. R., et al. (1990), The Second Generation Regional Acid Deposition Model Chemical Mechanism for Regional Air Quality Modeling, *J. Geophys. Res.*, *95*(D10), 16343-16367.

Stohl, A. (2001), A 1-year Lagrangian ‘‘climatology’’ of airstreams in the Northern Hemisphere troposphere and lowermost stratosphere, *J. Geophys. Res.*, *106*, 7263-7279.

Talbot, R., et al. (2005), Diurnal characteristics of surface-level O_3 and other important trace gases in New England, *J. Geophys. Res*., 110, D09307.

Tanre´, D., Y. J. Kaufman, M. Herman, and S. Mattoo (1997), Remote sensing of aerosol properties over oceans using the MODIS/EOS spectral radiances, *J. Geophys. Res*., 102, 16,971– 16,988.

Tanrikulu, S., D.R. Stauffer, N.L. Seaman, and A.J. Ranzieri (2000), A field-coherence technique for meteorological field-program design for air quality studies. Part II: Evaluation in the San Joaquin Valley. *J. Appl. Meteor*., 39, 317-334.

Taubman, B. F., J. C. Hains, A. M. Thompson, L. T. Marufu, B. G. Doddridge, J. W. Stehr, C. A. Piety, and R. R. Dickerson (2006), Aircraft vertical profiles of trace gas and aerosol pollution over the mid-Atlantic United States: Statistics and meteorological cluster analysis, *J. Geophys. Res.*, 111, D10S07, doi:10.1029/2005JD006196.

Thompson, A. M., (2003), Southern Hemisphere Additional Ozonesondes (SHADOZ) 1998-2000 tropical ozone climatology, 1, Comparison with Total Ozone Mapping Spectrometer (TOMS) and ground-based measurements, *J. Geophys. Res*., 108 (D2), 8238.

Thompson, A.M., Witte, J.C., Smit, H.G.J., Oltmans, S.J., Johnson, B.J., Kirchhoff, V.W.J.H., Schmidlin, F.J. (2007a), Southern Hemisphere Additional Ozonesondes (SHADOZ) 1998–2004 tropical ozone climatology. 3. Instrumentation, station variability, evaluation with simulated flight profiles. *J. Geophys. Res.* 112, D03304.

Thompson, A.M., et al. (2007b), Intercontinental Transport Experiment Ozonesonde Network Study (IONS 2004): 1 Summertime upper tropospheric/lower stratosphere

ozone over northeastern North America. *J. Geophys. Res.* 112, D12S12.

Thompson, A.M., et al. (2007c), Intercontinental Transport Experiment Ozonesonde Network Study (IONS, 2004): 2. Tropospheric ozone budgets and variability over northeastern North America. *J. Geophys. Res.* 112, D12S13.

Thompson, A.M., et al. (2008), Tropospheric ozone sources and wave activity over Mexico City and Houston during MILAGRO/Intercontinental Transport Experiment (INTEX-B) Ozone Network Study, 2006 (IONS-06). *Atmos. Chem. Phys.* 8, 5113–5126.

Thornton, J., et al. (2010), A large atomic chlorine source inferred from mid-continental reactive nitrogen chemistry, *Nature*, 464, 271- 274.

Umeda, T. and P.T. Martien (2002), Evaluation of a data assimilation technique for a mesoscale meteorological model used for air quality modeling. *J. Appl. Meteor*., 41, 12-29.

Vogt, R., P. J. Crutzen and R. Sander (1996), A mechanism for halogen release from sea salt aerosol in the remote marine boundary layer, *Nature*, 383, 327-330.

Vonder Haar, T.H., et al. (1968), Phonomenology of Convective Ring Clouds in the Tropics Derived from Geosynchrous Satellite Observations. Preprint from Proceedings of the International Conference of Cloud Physics, Toronto, Canada.

Wang, et al., (2009), Weather Research and Forecasting ARW Users Manual (NCAR) 310 pp.

Wilks, D. S. (1995), Statistical Methods in Atmospheric Sciences: An Introduction, 500 pp., Academic Press.

Worden, J., et al. (2004), Predicted errors of tropospheric emission spectrometer nadir retrievals from spectral window selection, *J. Geophys. Res.*, *109*(D09308).

Worden, J. et al. (2007), Improved tropospheric ozone profile retrievals using OMI and TES radiances, *Geophys. Res. Lett.*, 34, L01809.

Wu, S., L. J. Mickley, D. J. Jacob, J. A. Logan, R. M. Yantosca, and D. Rind (2007), Why are there large differences between models in global budgets of tropospheric ozone?, *J. Geophys. Res.*, 112, D05302, doi:10.1029/2006JD007801.

Yarwood, G., et al. (2005), Updates to the Carbon Bond chemical mechanism: CB05. Final Report to the US EPA, RT-0400675, December 8, 2005 /http://www.camx.com/publ/pdfs/CB05_Final_Report_120805.pdf.

Yienger, J. J., et al. (2000), The episodic nature of air pollution transport from Asia to North America, *J. Geophys. Res*, 105, 26,931-926,945.

Yorks, J. E., et al. (2009), The variability of free tropospheric ozone over Beltsville, Maryland (39N, 77W) in the summers 2004–2007, *Atmos. Environ.*, *43*, 1827-1838.

Yu, S., et al. (2007), A detailed evaluation of the Eta-CMAQ forecast model performance for O_3, its related precursors, and meteorological parameters during the 2004 ICARTT study, *J. Geophys. Res.*, 112, D12S14.

Zhang, D.-L., Y.-X. Shou, and R. R. Dickerson (2009), Upstream urbanization exacerbates urban heat island effects, *Geophys. Res. Lett*., 36, L24401, doi:10.1029/2009GL041082.

Zhang, L., Jacob, D. J., Liu, X., Logan, J. A., Chance, K., Eldering, A., and Bojkov, B. R. (2010): Intercomparison methods for satellite measurements of atmospheric composition: application to tropospheric ozone from TES and OMI, *Atmos. Chem. Phys. Discuss.*, 10, 1417-1456, doi:10.5194/acpd-10-1417-2010.

Zhang, Y., et al. (2006), A comprehensive performance evaluation of MM5-CMAQ for the summer 1999 Southern Oxidants Study episode – Part II: Gas and aerosol predictions, *Atmos. Environ*., 40, 4839-4855.

Ziemke, J. R., S. Chandra, B. N. Duncan, L. Froidevaux, P. K. Bhartia, P. F. Levelt, and J. W. Waters (2006), Tropospheric ozone determined from Aura OMI and MLS: Evaluation of measurements and comparison with the Global Modeling Initiative's Chemical Transport Model, *J. Geophys. Res.*, 111, D19303, doi:10.1029/2006JD007089.